Expanding the Optical Capabilities of Germanium in the Infrared Range Through Group IV and III-V-IV Alloy Systems

by

Patrick Michael Wallace

A Dissertation Presented in Partial Fulfillment
of the Requirements for the Degree
Doctor of Philosophy

Approved August 2018 by the
Graduate Supervisory Committee:

John Kouvetakis, Chair
José Menéndez
Ryan Trovitch

ARIZONA STATE UNIVERSITY

December 2018

ABSTRACT

The work described in this thesis explores the synthesis of new semiconductors in the Si-Ge-Sn system for application in Si-photonics. Direct gap $Ge_{1-y}Sn_y$ (y=0.12-0.16) alloys with enhanced light emission and absorption are pursued. Monocrystalline layers are grown on Si platforms via epitaxy-driven reactions between Sn- and Ge-hydrides using compositionally graded buffer layers that mitigate lattice mismatch between the epilayer and Si platforms. Prototype *p-i-n* structures are fabricated which exhibit direct gap electroluminescence and tunable absorption edges between 2200-2700 nm indicating applications in LEDs and detectors. Additionally, a low-pressure technique is described producing pseudomorphic $Ge_{1-y}Sn_y$ alloys in the compositional range y=0.06-0.17. Synthesis of these materials is achieved at ultra-low temperatures resulting in nearly defect-free films that far exceed the critical thicknesses predicted by thermodynamic considerations, and provide a chemically driven route toward materials with properties typically associated with molecular beam epitaxy.

Silicon incorporation into $Ge_{1-y}Sn_y$ yields a new class of $Ge_{1-x-y}Si_xSn_y$ (y>x) ternary alloys using reactions between Ge_3H_8, Si_4H_{10}, and SnD_4. These materials contain small amounts of Si (x=0.05-0.08) and Sn contents of y=0.1-0.15. Photoluminescence studies indicate an intensity enhancement relative to materials with lower Sn contents (y=0.05-0.09). These materials may serve as thermally robust alternatives to $Ge_{1-y}Sn_y$ for mid-infrared (IR) optoelectronic applications.

An extension of the above work is the discovery of a new class of Ge-like Group III-V-IV hybrids with compositions $Ga(As_{1-x}P_x)Ge_3$ (x=0.01-0.90) and $(GaP)_yGe_{5-2y}$

related to $Ge_{1-x-y}Si_xSn_y$ in structure and properties. These materials are prepared by chemical vapor deposition of reactive Ga-hydrides with $P(GeH_3)_3$ and $As(GeH_3)_3$ custom precursors as the sources of P, As, and Ge incorporating isolated GaAs and GaP donor-acceptor pairs into diamond-like Ge-based structures. Photoluminescence studies reveal bandgaps in the near-IR and large bowing of the optical behavior relative to linear interpolation of the III-V and Ge end members. Similar materials in the Al-B-P-Sb system are also prepared and characterized. The common theme of the above topics is the design and fabrication of new optoelectronic materials that can be fully compatible with Si-based technologies for expanding the optoelectronic capabilities of Ge into the mid-IR and beyond through compositional tuning of the diamond lattice.

For my friends, my family, and for Sarah. I would not have made it without you.

ACKNOWLEDGMENTS

First, I would like to thank Professors John Kouvetakis and José Menéndez. Without their support and expertise, none of the work described here would have been possible. I would also like to acknowledge my colleagues: Dr. James Gallagher, Dr. C. Lasitha Senaratne, Dr. Patrick E. Sims, and Dr. Chi Xu for providing training, guidance, and collaboration on many aspects of this research.

I would like to recognize the facilities provided by the Leroy Eyring Center for Solid State Sciences, the John M. Cowley Center for High Resolution Electron Microscopy, and the Ira A. Fulton Center for Solid State Electronics Research at Arizona State University, as well as assistance I have received from their knowledgeable staff.

This research was funded by Air Force Office of Scientific Research grants FA9550-12-1-0208, FA9550-13-1-0022, and FA9550-17-1-0314; as well as the National Science Foundation grant DMR-1309090. Without funding from these organizations, none of these research efforts could have taken place.

I would like to thank my Mom and Dad for always supporting me, and encouraging me to go far in life. I would like to thank the many friends I have made at Arizona State University who I have leaned on frequently over the years. Finally, I would like to thank Sarah Yandle who was always by my side, believing in me through difficult times.

TABLE OF CONTENTS

Page

LIST OF TABLES…….....ix

LIST OF FIGURES……...……..x

CHAPTER

1 BACKGROUND AND MOTIVATION FOR EXTENDING THE OPTICAL RANGE OF Ge-BASED MATERIALS..……..……1

1.1 Introduction…….…….……..1

1.2 Pursuit of Group IV-Based Optoelectronic Materials Through $Ge_{1-y}Sn_y$ Alloys……...……..…….....3

1.3 Group IV Ternary Compounds: $Ge_{1-x-y}Si_xSn_y$…….…….…….……6

1.4 Alternative p-type Doping Strategies in Ge……..……...…..…8

1.5 Integrating III-V Dimers within a Group IV Matrix: III-V-IV Hybrid Materials as a Route Toward Ge-based Photonics……..…..…10

1.6 Beyond Ge: Heavy III-V-IV and III-V Alloys Containing Sb……13

2 DIRECT GAP $Ge_{1-Y}Sn_Y$ ALLOYS: FABRICATION AND DESIGN OF MID-IR PHOTODIODES AND PHOTOLUMINESCENCE FROM HIGH Sn CONTENT $Ge_{1-X-Y}Si_XSn_Y$ MATERIALS……...…..…..15

2.1 Introduction……..…….16

2.2 Experimental……..……...……..…..19

2.3 Results and Discussion……..……..….24

CHAPTER Page

2.3.1 Structural Analysis……..……...24

2.3.2 Electronic Properties……..……..……..33

2.3.3 Band Gap Analysis…….…..…….36

2.4 High Sn Content $Ge_{1-x-y}Si_xSn_y$ Materials and Insights into Si-Sn Bandgap Bowing …….…..……...……..…..40

2.4.1 Synthetic Routes Toward High Sn Content $Ge_{1-x-y}Si_xSn_y$ Films……..40

2.4.2 Structural and Compositional Characterization of $Ge_{1-x-y}Si_xSn_y$ Materials……..…….……...……..41

2.4.3 Photoluminescence Studies of $Ge_{1-x-y}Si_xSn_y$ Films……...…44

2.4.4 Insights into Si-Sn Band Gap Bowing……...46

2.5 Summary…….…….…..50

3 MOLECULAR EPITAXY OF PSEUDOMORPHIC $Ge_{1-Y}Sn_Y$ (Y = 0.06 - 0.17) MATERIALS AND DEVICES ON Si/Ge AT ULTRA-LOW TEMPERATURES VIA REACTIONS OF Ge_4H_{10} AND SnD_4…….……...……..…...52

3.1 Introduction……..……..……..53

3.2 Experimental……..……..56

3.3 Results and Discussion……..……..59

3.3.1 Composition and Structural Analysis……...……..…...59

3.3.2 Doping and Device Fabrication…….64

3.3.3 Strain Relaxed $Ge_{1-y}Sn_y$ Films via Ge_4H_{10} and SnD_4……69

CHAPTER Page

3.4 Summary……..……75

4 FABRICATION OF Ge:Ga HYPER-DOPED MATERIALS AND DEVICES USING CMOS COMPATIBLE Ga AND Ge HYDRIDE CHEMISTRIES …...……...…....77

4.1 Introduction……...……..…….78

4.2 Experimental……...…….83

4.2.1 Depositions Methods……..……..……....84

4.3 Results and Discussion……..……..86

4.3.1 Doping and Activation Characterizations.…..……..……..…86

4.3.2 Structural and Morphological Properties……..……..…93

4.3.3 Photoluminescence Properties.……..……98

4.3.4 Diode Fabrication and Testing…….…101

4.4 Summary……104

5 SYNTHESIS AND STRUCTURAL AND OPTICAL PROPERTIES OF III-V-IV HYBRID ALLOYS: $Ga(As_{1-X}P_X)Ge_3$ AND $Al(P_{1-X}Sb_X)Si_3$ SEMICONDUCTORS……..……..…106

5.1 Introduction……....107

5.2 Experimental…….….111

5.3 Results and Discussion…….……117

5.3.1 $Ga(As_{1-x}P_x)Ge_3$ Composition and Structural Analysis ...…….119

5.3.2 $Al(P_{1-x}Sb_x)Si_3$ Composition and Structural Analysis…….…..125

5.3.3 Microstructure Analysis…….……..….128

CHAPTER Page

5.3.4 $Ga(As_{1-x}P_x)Ge_3$ Optical Properties……...……136

5.4 Summary…..……..141

6 BEYOND GERMANIUM: SYNTHESIS OF III-V MATERIALS VIA REACTIONS BETWEEN $Al(BH_4)_3$ AND PH_3 AND SbD_3 GROUP V HYDRIDES…..……...…..143

6.1 Introduction…….…….144

6.2 Low-Pressure CVD Methods to Produce BP and $Al_{1-x}B_xSb$ Materials..….146

6.3 Composition and Structural Analysis of BP and $Al_{1-x}B_xSb$ Materials……...……149

6.4 Summary……..……..……..157

REFERENCES……..……..158

APPENDIX

A PERMISSIONS FOR REPRINTED MATERIALS……174

LIST OF TABLES

Table Page

1 Sn-rich $Ge_{1-x-y}Si_xSn_y$ Films……..……..…...41

2 List of Pseudomorphic $Ge_{1-y}Sn_y$ Films……..……..…….……57

3 Representative Ga Doped Ge Samples……..…….……..…86

4 Comparison Between Various Ga Doping Methods…….…..…...92

5 Summary of $Ga(As_{1-x}P_x)Ge_3/Ge_{1-x}Si_x$ Samples……..…….112

6 List of Selected $Al(P_{1-x}Sb_x)Si_3$ Films……..……...…….116

LIST OF FIGURES

Figure Page

1 Band Diagrams for Ge and α-Sn……5

2 Diagram Showing Several Classes of Semiconductor Materials……..……..…10

3 Theoretical Band Gap Bowing of $(GaAs)_{1-2x}Ge_{2x}$……..……..…12

4 Comparison of E_0 and Δ_0 in $Ge_{1-y}Sn_y$ Alloys……..…..18

5 XSTEM Images of n-Ge/i-$Ge_{0.863}Sn_{0.137}$/p-$Ge_{0.92}Sn_{0.08}$…….…..……25

6 HR-XRD (224) RSM of n-Ge/i-$Ge_{0.863}Sn_{0.137}$/p-$Ge_{0.92}Sn_{0.08}$…….……..……27

7 EL Plot of a 12% Sn Device……...……..……28

8 HR-XRD RSM of a n-$Ge_{0.89}Sn_{0.11}$/i-$Ge_{0.85}Sn_{0.15}$/p-$Ge_{0.85}Sn_{0.15}$ Diode……..…..….30

9 XTEM Micrographs of a n-Ge/n-$Ge_{0.89}Sn_{0.11}$/i-$Ge_{0.85}Sn_{0.15}$/p-$Ge_{0.85}Sn_{0.15}$ Diode…...32

10 Schematic and I-V Curves for Diodes with y = 0.135-0.16 Active Layers……..…34

11 Comparison of Diode Currents at -1.0 V Bias Between Ge/GeSn/GeSn and GeSn/GeSn/GeSn……..……35

12 Calculated Band Lineup at Different GeSn/GeSiSn Heterostructures……..…...37

13 HR-XRD Spectra of n-$Ge_{0.77}Si_{0.08}Sn_{0.15}$……...……..…..42

14 RBS Spectra of a $Ge_{0.77}Si_{0.08}Sn_{0.15}$ Film……..……..……...43

15 Photoluminescence Spectra of $Ge_{1-x-y}Si_xSn_y$ Materials…….……...45

Figure Page

16 Three Phase Diagrams of Ge-Si-Sn with Various Si-Sn Bowing Parameters…..…....47

17 Experimental Band Gap Energies of $Ge_{1-x-y}Si_xSn_y$ Alloys……..….49

18 HR-XRD Spectra from $Ge_{1-y}Sn_y$ Alloy Films with y = 0.10-0.17……..…..60

19 RBS Spectra of a $Ge_{0.83}Sn_{0.17}$ Film……..…….……..…..61

20 XSTEM Images of $Ge_{0.83}Sn_{0.17}$ Alloy……..……..……...…63

21 SIMS Spectrum for a Sample with 11% Sn Content Doped by P……..…..64

22 (224) RSM and (004) θ/2θ Scan of n-type doped $Ge_{0.91}Sn_{0.09}$ and XTEM Image of an n-$Ge_{0.91}Sn_{0.09}$/p-$Ge_{0.94}Sn_{0.06}$ Diode…….……...……66

23 Differential Conductance vs. Voltage Obtained from n-$Ge_{0.91}Sn_{0.09}$/p-$Ge_{0.94}Sn_{0.06}$….68

24 Thickness vs. Composition for Fully Strained and Partially Relaxed $Ge_{1-y}Sn_y$……...71

25 PL Spectra Obtained from Relaxed $Ge_{0.922}Sn_{0.078}$ and $Ge_{0.933}Sn_{0.067}$ Films…….....74

26 Real and Imaginary Dielectric Functions ε_1 and ε_2 for Ga Doped Ge……..……88

27 SIMS Spectra of a Ga doped Ge Film……..……..……..89

28 Plots of Ga Dopant Activation Ratios in Ge…….……..…..90

29 Resistivity of Ge:Ga Samples……...……....91

30 XRD (004) and (224) Scans for a Ga Doped Ge Sample……..……..…….94

31 RBS Spectra for a Ga Doped Ge Sample……..…..…....95

Figure Page

32 RBS Spectra for a 1.3 μm Thick Ge:Ga Layer…….……....96

33 XTEM Image of a Ge:Ga Layer Grown Upon $Ge_{0.95}Si_{0.05}$ Buffered Si……...…...….97

34 PL Spectra and Peak Fitting for Ge:Ga Samples……..…….…...99

35 Schematic and I-V Plots of a Ge:Ga p-i-n Device……..……102

36 EL Spectra of a 300 μm Ge:Ga p-i-n Photodiode……...……..……..103

37 Structural Model of $Ga(As_{1-x}P_x)Ge_3$ on a $Ge_{1-x}Si_x$ Buffer Layer……..…….…110

38 RBS Spectrum of $GaAs_{0.15}P_{0.85}Ge_3/Ge_{0.70}Si_{0.30}$ Sample……...……..……118

39 HR-XRD on-axis Plots and (224) RSM of $GaAs_{0.8}P_{0.2}Ge_3$ Grown on $Ge_{0.83}Si_{0.17}$ and $Ge_{0.93}Si_{0.07}$ Buffer Layers……..…….…….…119

40 Relaxed Cubic Lattice Parameter a_0 for $Ga(As_{1-x}P_x)_yGe_{5-2y}$ Alloys……...122

41 Structural Models of $GaAsGe_3$ and $GaPGe_3$……...123

42 HR-XRD Plots of an $AlP_{0.89}Sb_{0.11}Si_3$ Film……..…….……..……126

43 RBS Spectra of an $AlP_{0.89}Sb_{0.11}Si_3$ and $AlSbSi_3$ Film……..……..127

44 STEM Images of $Ga(As_{0.80}P_{0.20})Ge_3$ Grown on a $Ge_{0.88}Si_{0.12}$ Buffer…….……..…..129

45 XTEM Data $Ga(As_{0.80}P_{0.20})Ge_3$ Grown Lattice Matched on a $Ge_{0.93}Si_{0.07}$ Buffer…130

46 XTEM Images of $GaPGe_{3.3}$ Grown on a $Ge_{0.70}Si_{0.30}$ Buffer ……..……..……..…132

47 XTEM Micrograph of an $AlP_{0.88}Sb_{0.12}Si_3$ Sample……..134

Figure Page

48 XTEM Micrograph of an $AlPSbSi_3$ Sample……...……135

49 Room Temperature Raman Spectra of $GaPGe_{3.3}$ and $GaAs_{0.8}P_{0.2}Ge_3$……136

50 PL Plots of $Ga(As_{0.8}P_{0.2})Ge_3$……...137

51 Plots of Absorption Coefficients from a $GaAs_{-0.7}P_{0.3}Ge_3$ Sample and Reference GaP, GaAs, and Ge End Members……...……...…140

52 SIMS and RBS spectra of a BP Film on Si(100)……150

53 EELS Maps of a BP Film……...151

54 XTEM Micrograph, Electron Diffraction and FT-IR Spectra of a BP Film……..153

55 SIMS and RBS spectra of an $Al_{0.95}B_{0.05}Sb$ Film on Si(100)……..154

56 XTEM Micrograph, Electron Diffraction and FT-IR Spectra of $Al_{0.95}B_{0.05}Sb$……..156

Chapter 1

BACKGROUND AND MOTIVATION FOR EXPANDING THE OPTICAL RANGE OF Ge-BASED MATERIALS

1.1 Introduction

Nearly all modern electronic devices function using digital logic circuits made possible through innovative semiconductor device design, and cutting edge solid-state materials. Initial interest in semiconductor materials came to prominence in the early half of the 20th century when Group IV elements such as silicon and germanium were described as "poorly conducting metals",[1] then in 1947 the first solid-state transistor was produced at Bell Labs utilizing a large sample of elemental germanium.[2] This kick started a revolution spanning the next several decades that would allow complex and clunky vacuum tube technologies to be replaced with smaller, simpler solid-state components. In 1958 the first integrated circuit (IC) was produced by Jack Kilby at Texas Instruments semiconductor lab,[3] the development of a single component capable of containing entire multi-device circuits allowed bulky single room computers to be reduced in size to the point where use in a home or business became practical. The rapid increase in productivity made possible through the assistance of computers lead to technological progress rivaled only by the industrial revolution of the 19th century, and thus the information age was born.

In addition to digital logic technologies made possible through the development of semiconductor materials, advances have been made to improve electronics that interact with light. These so-called optoelectronic materials are a broad class of electronic materials that absorb or emit light, including light emitting diodes (LEDs) and solid-state lasers, photovoltaics, photodetectors, and recently even photonic ICs. Early technologies made use of III-V compound semiconductor alloys comprising of two or more elements combined into a single material. The role of III-V materials in optoelectronics originated with electroluminescence reported from GaAs in 1955 by RCA,[4] and their efficiency and optical range continued to expand through the 1960s. Currently LEDs are capable of producing light across the entire visible range and "white light" LED bulbs are quickly becoming energy efficient alternatives to incandescent and fluorescent technologies in homes and businesses.

Typically, III-V materials are desired materials for light emitting devices due to their direct gap behavior, meaning there is an increased probability of electron energy transitions occurring through photon emission as opposed to phonon emission. In an indirect gap semiconductor, a change in crystal momentum must occur for an electron to transition between energy bands, these transitions occur through phonon emission, i.e. a quantized vibration through the crystal lattice. In a direct gap semiconductor there is no transfer of momentum, and thus transitions may occur entirely through photon emissions increasing efficiency in optoelectronic applications.

1.2 Pursuit of a Group IV-Based Optoelectronic Material Through $Ge_{1-y}Sn_y$ Alloys

Currently nearly all solid-state technologies use Si wafers as platforms due to their relatively low cost and ease of manufacture. High quality monocrystalline Si wafers with 24-inch diameters can be routinely produced on an industrial scale; the technology is well established and can be relied upon as a starting material for commercial scale production of consumer electronics. Currently III-V materials dominate the optoelectronics field since they possess direct gaps spanning the visible and infrared (IR) range, however III-V materials cannot be easily integrated with Si through traditional means, which is major impediment to the development of photonic ICs. Because the Si wafer is ubiquitous in the commercial semiconductor industry it would be advantageous to have a Group IV direct gap material that can be deposited directly onto a Si substrate. Unfortunately, none of the Group IV elements are intrinsically direct gap materials, and thus are ill suited for optoelectronic applications.

Elemental Ge is an indirect band gap material with an energy of 0.66 eV, however the direct gap transition of Ge at 0.8 eV is only slightly higher in energy than the indirect transition making it "nearly" a direct gap material. This property is visualized in the top panel of Figure 1 where the band diagram of Ge is shown. There are several strategies that can be used to push Ge into the direct gap regime. One commonly used technique is to dope Ge *n*-type with an ultra-high carrier concentration ($>1.0x10^{20}$ cm^{-3}), in this case the L-valley of the conduction band of Ge is filled with enough carriers that there are no more energy levels available, and any further transitions to the conduction band are

forced to occur at the Γ-point. While this approach produces a quasi-direct gap material, it is impracticable from a device fabrication perspective due to free carrier absorption. Another potential approach is through strain engineering of the Ge lattice, under high tensile strain the shape of the conduction band changes such that it transitions toward direct gap behavior. Although this strategy has been attempted, the ultra-high tensile strain required to reach direct gap behavior is impractical, and typically, the material falls apart under high strain before it becomes direct gap.

The most promising strategy used to induce direct gap behavior in Ge is by forming an alloy, in this case with Sn. Sn is also a Group IV material located just below Ge on the periodic table. Elemental Sn has two common allotropes; β-Sn (also known as "white tin") is a tetragonal structure material that is stable at temperatures above 13 °C, β-Sn is the well-known metallic form of Sn. However, a second less common form of Sn exists as α-Sn, or "grey tin". This brittle allotrope of Sn adopts the diamond cubic crystal structure similar to the other Group IV elements: C, Si, and Ge. It is typically only stable at temperature below 13 °C, however when alloyed with another Group IV material the diamond cubic structure is maintained at much higher temperatures. Most significantly, α-Sn has a bandgap of -0.4 eV as can be seen is the bottom panel of Figure 1. When alloys are formed between Ge and Sn the Γ-point transition energy decreases more rapidly than that of the L-point, causing a transition toward direct gap behavior. This transition is predicted to occur with Sn contents as low as 6.5% in unstrained films,[5] and has been observed experimentally at ~9% Sn.[6] Although the resulting material is no longer purely elemental Ge it is still an entirely Group IV material and can be easily

integrated directly onto Si or other Group IV substrates and is the most practical strategy for use as a direct gap material in functional devices.

However, the preparation of $Ge_{1-y}Sn_y$ is not without its challenges. From a thermodynamics standpoint, Sn has a solubility in Ge materials of less than 1%. This presents a problem for producing a direct gap material which requires ~9% Sn or more,

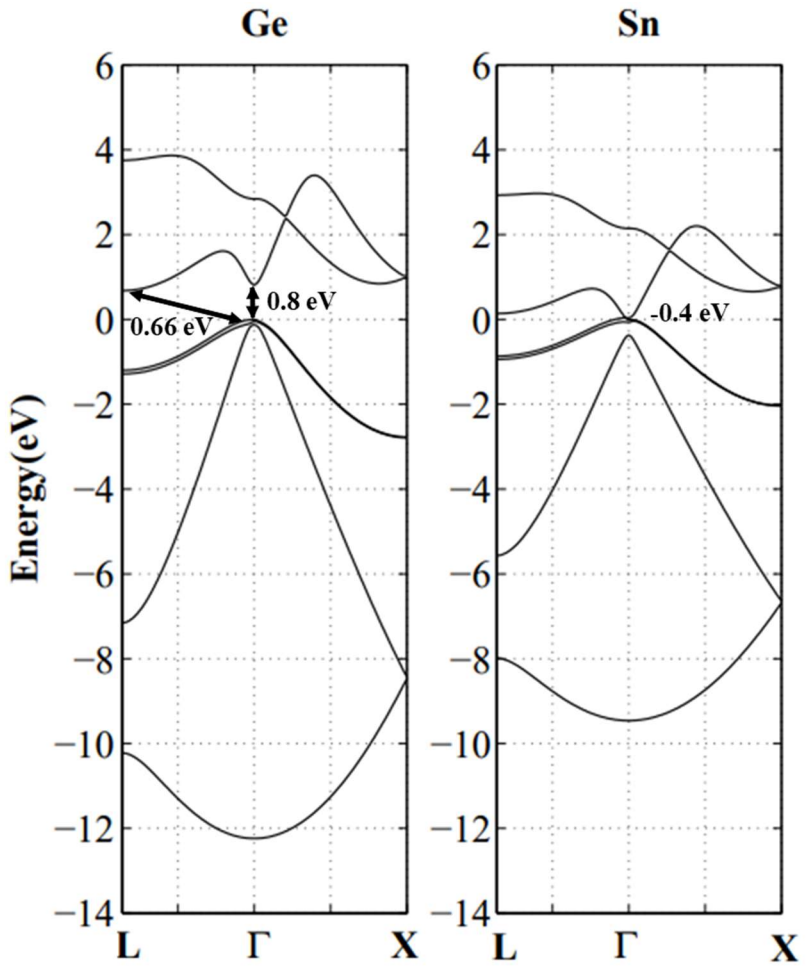

Figure 1: Left – the band diagram of Ge showing the lowest energy transition, 0.66 eV, occurring at the L-point. Note the transition to the Γ-point is only slightly higher in energy. Right – the band diagram of α-Sn showing the band overlap at the Γ-point. Alloys between these two elements are capable of forming a direct gap material. Figure modified from Moontragoon *et al.*[7]

thus kinetic strategies must be used in order to achieve alloys with the desired composition. $Ge_{1-y}Sn_y$ alloys were first produced using sputtering methods in the 1980s,[8] followed quickly by molecular beam epitaxy (MBE) which became a common technique throughout the 1990s with single-phase pseudomorphic films up to 200 nm thick being grown.[9] $Ge_{1-y}Sn_y$ materials were first made practical in 2002 with the introduction of Sn-hydrides by the Kouvetakis-Menendez group at Arizona State University.[10,11] This made chemical vapor deposition (CVD) routes toward $Ge_{1-y}Sn_y$ possible, and thus a potential material for commercial device manufacture. CVD methods with finely tuned deposition parameters have allowed materials with Sn contents far beyond the thermodynamic limit to be produced. Prototype electronic devices such as LED's, photodetectors, solar panels, and even optically pumped lasers have been fabricated from these materials,[12] and the future is bright for commercial Group IV optoelectronics becoming a reality.

1.3 Group IV Ternary Compounds: $Ge_{1-x-y}Si_xSn_y$

While recent efforts to produce Group IV photonic materials have focused primarily on $Ge_{1-y}Sn_y$ alloys between Ge and Sn, a ternary analogue incorporating Si has been pursued in parallel. This ternary system, with the formula $Ge_{1-x-y}Si_xSn_y$, presents several potential advantages over $Ge_{1-y}Sn_y$, which may make it a more attractive candidate for use as an optoelectronic material.

One significant advantage of $Ge_{1-x-y}Si_xSn_y$ is its relatively high thermal stability when compared with $Ge_{1-y}Sn_y$[13]. This results in a more robust material for electrically

activated devices which tend to operate at higher temperatures. Previous efforts have shown that the incorporation of even 1-2% Si has the added benefit of providing significantly more thermal stability to the resultant $Ge_{1-x-y}Si_xSn_y$ alloy than that of an equivalent $Ge_{1-y}Sn_y$ alloy.

In addition to the thermal stability of $Ge_{1-x-y}Si_xSn_y$, the ternary system also has the advantage of an additional compositional degree of freedom due to the presence of Si. Because of the large atomic size difference between Ge and Sn incorporating even a small amount of Si into $Ge_{1-y}Sn_y$ can significantly reduce the strain of the lattice. A major challenge currently facing high Sn content $Ge_{1-y}Sn_y$ materials is the lack of suitable substrates to be used for epitaxial growth. Typically, Ge is used as a virtual substrate to integrate $Ge_{1-y}Sn_y$ with Si wafers. However, this method becomes problematic at high Sn compositions, a $Ge_{1-y}Sn_y$ alloy with 12% Sn has a lattice constant of 5.757 Å which is more than 1.7% larger than the lattice constant of Ge (5.658 Å). This becomes a significant obstacle in attempts to grow relaxed materials in the mid-IR regime. In fact, some deposition strategies have resorted to the use of multiple $Ge_{1-y}Sn_y$ grading layers to achieve high Sn content films.[14] The $Ge_{1-x-y}Si_xSn_y$ system is more efficient at mitigating this mismatch strain because the Si content intrinsic to the film can be adjusted to decrease the size of the lattice parameter.

Additionally, recent insights have suggested a large bandgap bowing exists between Si and Sn, meaning the bandgap of $Ge_{1-x-y}Si_xSn_y$ alloys cannot be predicted by simple linear interpolation between the end members. In fact, the bowing parameter of Si-Sn may be large enough that the addition of Si into $Ge_{1-y}Sn_y$ may shift the band gap to

even lower energies at high Sn contents ($y > 0.15$). If this is the case, $Ge_{1-x-y}Si_xSn_y$ may be an even better candidate for mid-IR devices than the $Ge_{1-y}Sn_y$ binary because the addition of small amounts of Si would shift the band gap even further into the IR while simultaneously providing additional thermal stability and reducing strain.

1.4 Alternative *p*-type Doping Strategies in Ge

In order to produce functional electronic devices from $Ge_{1-y}Sn_y$ and $Ge_{1-x-y}Si_xSn_y$ alloys it is necessary to explore both *n*- and *p*-type dopant materials. *In situ n*-type doping sources for elemental Ge and Ge-based materials ($Ge_{1-y}Sn_y$ and $Ge_{1-x-y}Si_xSn_y$) have been studied extensively to the point where the use of Group V hydrides such as $P(GeH_3)_3$ or SbD_3 has become routine.[15,16] In the case of *p*-type doping however, a chemical source that can used to *in situ* dope Ge to high carrier concentration ($> 1x10^{20}$ cm^{-3}) is a more difficult problem to overcome. While this is a notable problem for the fabrication of high efficiency optoelectronics, it is especially salient for *p*-type metal-oxide-semiconductor logic (PMOS) design where the low resistivity afforded by high carrier concentrations is critical.

Traditionally, B_2H_6 has been used as a *p*-type doping source for Ge-based alloys. However, due the relatively low solubility of B in Ge films, carrier concentrations above $1x10^{20}$ cm^{-3} are difficult to achieve through conventional CVD methods making B an inferior choice in device design.[17,18] More so, at high carrier concentrations B can easily precipitate out of the Ge lattice.[19] Moving down Group III of the periodic table, Ga is

clearly the sensible choice for a *p*-type dopant as its atomic radius is nearly identical to Ge as indicated by its position directly to left of Ge. In fact, the solubility of Ga in Ge is higher than that of B meaning high carrier concentrations should be easily achievable.

Recently $[D_2GaN(CH_3)_2]_2$ has been used as a source of Ga atoms in III-V-IV thin film alloys with the formula $(GaP)_ySi_{5-2y}$.[20] Under CVD conditions this Ga hydride acts as a source of Ga through elimination of a stable $DN(CH_3)_2$ byproduct. With this in consideration $[D_2GaN(CH_3)_2]_2$ was used as a chemical source of Ga for use in *p*-type doping of Ge. This resulted in highly doped *p*-Ge films with high carrier activation, and prototype Ge photodiodes were fabricated to confirm the status of $[D_2GaN(CH_3)_2]_2$ as an *in situ p*-type doping source. The results of these studies are presented in Chapter 5 of this thesis. Thus far $[D_2GaN(CH_3)_2]_2$ has not been used as a dopant for other Ge-based materials such as $Ge_{1-y}Sn_y$ or $Ge_{1-x-y}Si_xSn_y$, but this work is ongoing and it is expected that $[D_2GaN(CH_3)_2]_2$ will act as a *p*-type doping source similar to what was observed in Ge.

1.5 Integrating III-V Dimers within a Group IV Matrix: III-V-IV Hybrid Materials as a Route Toward Ge-based Photonics

There are several alternate strategies to expand the optical possibilities of Ge beyond the alloys between Group IV elements discussed thus far. Figure 2 shows several classes of semiconductor materials available including II-VI and III-V compound semiconductors as well as the Group IV elemental semiconductors, there is no mixing shown between the material classes. Hybrid alloys between III-V compound

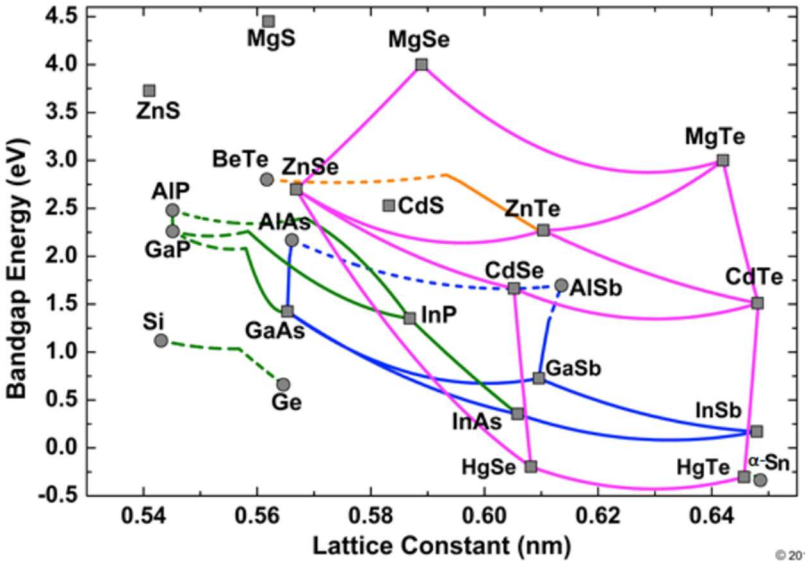

Figure 2: Diagram showing several classes of semiconductor materials with no intermixing between the classes. In this case, alloys are formed between the Group IV elements Si, and Ge shown as grey circles with green dashes between; as well as GaP and GaAs III-V materials shown as grey squares with green solid and dashed lines. Figure modified from Smith *et al*.[21]

semiconductors and Group IV materials are of some interest due to their potential for expanding the possible optical range while maintaining a similar lattice constant by mixing elements across periods versus down columns or the periodic table. Historically,

these hybrid materials have suffered from issues involving phase-segregation or compositional inhomogeneities.[22] However, the recent development of custom Group V hydrides with the general composition $M(SiH_3)_3$ and $M(GeH_3)_3$ where M = N, P, As, or Sb has enabled the incorporation of isolated III-V pairs through the formation of individual tetrahedral units centered on the Group V atom. Using this method compositional inhomogeneities are suppressed as these tetrahedral building blocks have the general composition (III-V)-IV_3 and are incorporated into the film as single units.

Extensive research has been performed using this technique with various III-V dimers having been incorporated into both Si and Ge matrices. However, in pursuit of an IR-active material, the incorporation of GaAs pairs into a Ge matrix is perhaps the most interesting. Theoretical predictions made for $(GaAs)_{1-2x}Ge_{2x}$ by Giorgi *et al.*[23] suggest that a material incorporating GaAs into Ge may have high band gap bowing resulting in a band gap that is far lower in energy than what might be expected through linear interpolation of the GaAs and Ge end members. A diagram of this theoretical bowing can be seen in Figure 3 below. In fact, the band gap bowing is predicted to be large enough that the material should become IR active in the composition range afforded by the tetrahedral unit growth method described above. Experimentally, the compositions produced were of the formula $(GaAs)_yGe_{5-2y}$ which is a slight departure from that used in theoretical models ($(GaAs)_{1-2x}Ge_{2x}$). The compositions used for the theoretical study were likely chosen due to their simplicity for producing a computational model, and the bowing effect was expected to be similar for the compositions pursued experimentally.

In the experiments described in this thesis, the incorporation of GaP units into Ge were pursued alongside GaAs, producing materials both at the end points, $(GaAs)_yGe_{5-2y}$ and $(GaP)_yGe_{5-2y}$, as well as a range of compositions in between. The expectation was that the incorporation of GaP pairs in addition to GaAs would allow an additional degree of freedom in composition and band gap tunability that may allow the optical range to be expanded over an even greater area. This was not found to be the case experimentally as small amounts of GaP effected no change in the PL spectra relative to pure $(GaAs)_yGe_{5-2y}$, and high amounts of GaP quenched the PL spectra entirely. The results of these experiments are described in detail in Chapter 6 of this thesis.

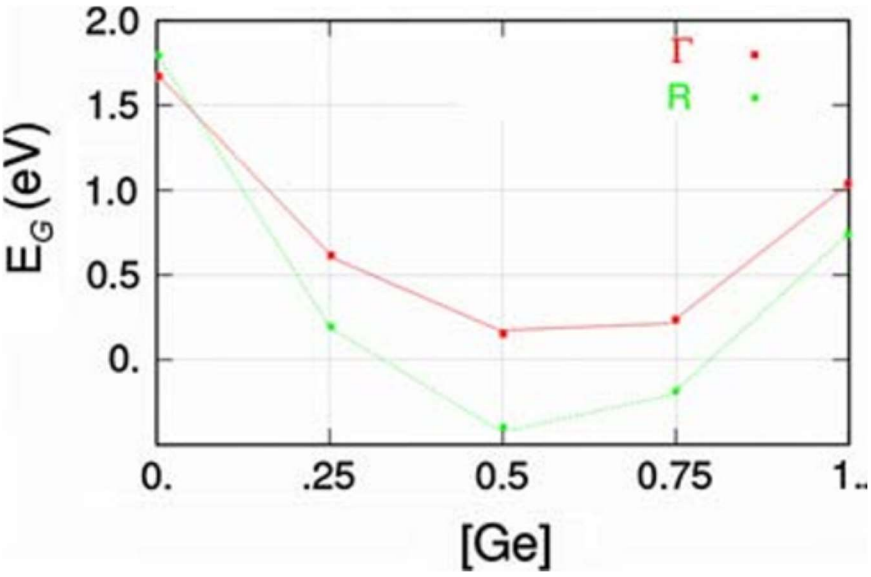

Figure 3: Theoretical band gap bowing of $(GaAs)_{1-2x}Ge_{2x}$ calculated using a quasipatricle *GW* approximation,[23] here the band gap at both the Γ-point and the R-point are plotted as a function of composition. Giorgi *et al.* found that high bowing resulted in a lower energy band gap than what would be expected resulting in an IR-active material.

1.6 Beyond Ge: Heavy III-V-IV and III-V Alloys Containing Sb

Extensive work has been done to incorporate isolated III-V pairs within Group IV materials using the tetrahedral building block method described in section 1.5 of this thesis. This class of hybrid alloys has opened up a wealth of possibilities for optoelectronic materials that can be integrated with Si. This work began with successful growth of $(AlP)_ySi_{5-2y}$ in 2011[24,25] and was subsequently expanded to include hybrid systems containing main group elements such as $Al(As_{1-x}N_x)_ySi_{5-2y}$, $(GaP)_ySi_{5-2y}$, and $(InP)_yGe_{5-2y}$,[26,20,27] of which the latter exhibited PL in the IR range. This work has recently been expanded upon to include AlSb pairs incorporated both alongside AlP as $Al(P_{1-x}Sb_x)Si_3$ alloys as well as alone as $(AlSb)_ySi_{5-2y}$. This alloy system is expected to exhibit unique optical properties that may be of interest. Additionally, these alloys have compositions that lattice match Ge and GaAs and could potentially be used as buffer layers between Group IV and III-V materials. Growth of these materials was achieved using both molecular $Al(BH_4)_3$ and an Al beam as sources of Al.

Further exploration of $Al(BH_4)_3$ as a Group III source was performed through the growth of compound III-V materials using $Al(BH_4)_3$ in combination with PH_3 and SbD_3 as precursors. $Al(BH_4)_3$ is known to act as a source of B atoms under CVD condititions,[28] and the initial goal of these experiments was to produce B-rich films with the composition $Al_{1-x}B_xP$ and $Al_{1-x}B_xSb$. BP and BSb are predicted to be highly refractory materials performing similarly to BAs[29] and are currently difficult or impossible to obtain through CVD methods. A CVD route toward these compounds would be useful as heat

dissipating materials that can be integrated directly with electronic devices. Interestingly this method was found to be capable of producing pure BP, however, thus far only Al-rich $Al_{1-x}B_xSb$ materials have been produced. This is likely due to the unfavorability of BSb bonding. Unfortunately, AlSb degrades quickly in the presence of oxygen,[30] and the same phenomena was observed in Al-rich $Al_{1-x}B_xSb$ films making structural analysis of the films difficult. A detailed examination of these films can be found in Chapter 6 of this thesis.

Chapter 2

DIRECT GAP $Ge_{1-Y}Sn_Y$ ALLOYS: FABRICATION AND DESIGN OF MID-IR PHOTODIODES AND PHOTOLUMINESCENCE FROM HIGH Sn CONTENT $Ge_{1-X-Y}Si_XSn_Y$ MATERIALS

Portions of this chapter were reprinted from Senaratne, C.L.; Wallace, P.M.; Gallagher, J.D.; Sims, P.E.; Kouvetakis, J.; Menéndez J. *J. Appl. Phys.* **2016***, 120*, 025701 with permission of AIP Publishing.

Synopsis

In this chapter, chemical vapor deposition methods for producing high Sn content $Ge_{1-y}Sn_y$ films are described. Ge and Sn hydrides are used to produce films with compositions in the y = 0.12 – 0.14 range directly onto Ge buffer Si substrates. Additionally, films with compositions y = 0.13 – 0.16 are produced using $Ge_{1-x}Sn_x$ grading layers where x < y in order to reduce lattice mismatch between the Ge buffer and the high Sn content active layers.

Prototype photodiodes with structures comprising of both *n*-Ge/*i*-$Ge_{1-y}Sn_y$/*p*-$Ge_{1-z}Sn_z$, as well as *n*-$Ge_{1-x}Sn_x$/*i*-$Ge_{1-y}Sn_y$/*p*-$Ge_{1-z}Sn_z$ were fabricated. The devices grown directly on Ge buffered Si showed rectifying diode behavior and clear electroluminescence, the device produced using $Ge_{1-x}Sn_x$ grading layers had an increase in reverse bias current. The latter observation is attributed to the enhancement of band-to-

band tunneling when all the diode layers consist of direct gap materials, and thus has implications for the design of light emitting diodes and lasers operating at desirable mid-IR wavelengths. The possibility of achieving Type-I structures using binary and ternary alloy combinations is discussed in detail, taking into account the latest experimental and theoretical work on band offsets involving such materials.

Ternary alloys were further explored and long-term PL and EL studies have provided insights into the Si-Sn bowing parameter. Fitting of a wide range of experimental data has yielded a Si-Sn bowing value of ~25 eV, which is in good agreement with determinations made in other studies using this material system.

2.1 Introduction

Substantial progress has been made in the development of $Ge_{1-y}Sn_y$ alloys since the introduction of a viable chemical vapor deposition (CVD) route in 2002.[31] This progress is remarkable if one considers that the room-temperature solid solubility of Sn in Ge is less than 1%.[32,33] In spite of this thermodynamic constraint, however, device-quality alloys with very high metastable Sn concentrations are now routinely synthesized.[34-36] These metastable alloys are not simple academic curiosities but have been incorporated into real device structures, including optically pumped lasers with compositions reaching 13% Sn,[12] and electroluminescent diodes with Sn concentrations above 10%.[37]

While the most recent generation of devices exceed the indirect-to-direct transition concentration y_c ~9% Sn,[6] fulfilling one of the basic goals of $Ge_{1-y}Sn_y$ research, there are fundamental and practical reasons for pursuing the development of $Ge_{1-y}Sn_y$ alloys with Sn concentrations well in excess of y_c. Near y_c, carriers pumped into the conduction band at room temperature reside mainly in the indirect *L* valleys—even in formally direct-gap materials—due to the very large density of states difference between the L minima and the direct valley at the Γ-point of the Brillouin zone (BZ). It is estimated that for 5×10^{17} cm^{-3} excited carriers in the conduction band, the population of the direct valley only reaches 50% of the pumped carriers, for a Sn concentration y = 21%. Another potentially important consideration is illustrated in Figure 4. Auger recombination has been identified by Sun and coworkers[38] as the main factor preventing $Ge_{1-y}Sn_y$ lasers from operating at room temperature. But as the Sn concentration is increased, the spin-orbit splitting Δ_0 increases and the direct gap E_0 decreases, which reduces and eventually eliminates (for $E_0 < \Delta_0$) Auger recombination involving hot holes, the dominant loss contribution in near-IR lasers.[39] From Figure 4, the required concentration to achieve this condition is y_A ~ 17%. At even higher Sn concentrations approaching the semiconductor-semimetal threshold, $Ge_{1-y}Sn_y$ alloys may represent a viable alternative to $Hg_{1-x}Cd_xTe$ alloys for far-IR applications integrated on Si platforms.

The far-infrared potential of $Ge_{1-y}Sn_y$ alloys requires an extension of the metastability window to much higher Sn concentrations than currently achieved. This chapter demonstrates that the CVD approach based on the Ge_3H_8/SnD_4 precursors can be extended to at least y = 16% by fabricating and testing a series of *p-i-n* diodes containing

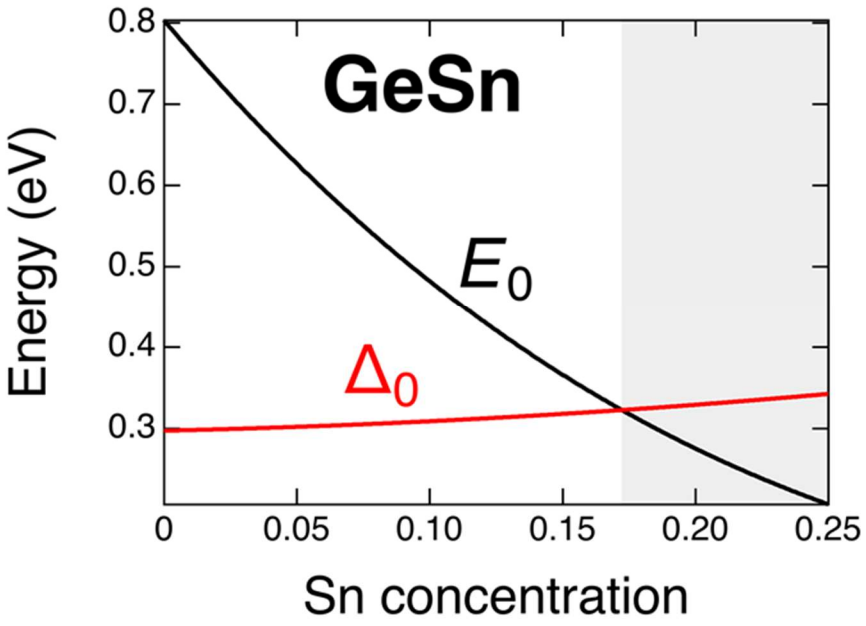

Figure 4: Comparison of the direct band gap E_0 and the spin-orbit splitting Δ_0 in $Ge_{1-y}Sn_y$ alloys. The shaded area corresponds to concentrations for which Auger recombination is suppressed.

such alloys. The use of real devices as a benchmark is important because, in addition to avoiding catastrophic segregation into distinct phases, the high-Sn material must remain free of crystalline defects that limit device performance. Some of these possible defects, such as the so-called β-Sn inclusion—in which a Sn atom fills a double vacancy in the Ge lattice—are predicted to become more abundant as the Sn concentration grows, and might preclude the use of high-Sn $Ge_{1-y}Sn_y$ in practical devices even if the material does not decompose.[40] Strain management at the interface between the high-Sn $Ge_{1-y}Sn_y$ film and the buffer layer remains the major consideration for achieving high-quality growth. No obvious synthetic barriers are identified in these experiments, suggesting that further increases the Sn concentration in practical device structures may be possible. The remainder of the chapter is organized as follows: in section 2.2, the possible synthetic

paths to high-Sn materials is discussed, and the choice of Ge_3H_8/SnD_4 is justified. In section 2.3, the results for devices grown on Ge-buffer layers, and Sn concentrations reaching 14% are presented. Additionally, even higher Sn concentration diodes can be achieved by inserting intermediate-composition $Ge_{1-x}Sn_x$ layers that mitigate the lattice mismatch between Ge and $Ge_{1-y}Sn_y$. Finally, in section 2.4 high Sn content $Ge_{1-x-y}Si_xSn_y$ films are explored as a potential cladding layer to produce Type-I heterojunctions for optoelectronic devices, and the Si-Sn bowing parameter is determined by collecting data from several PL and EL studies.

2.2 Experimental

Two distinct CVD approaches have emerged in the quest for high-Sn $Ge_{1-y}Sn_y$ alloys. The first method, introduced by the Kouvetakis research group, uses the inorganic Sn precursor deuterostannane (SnD_4) as the Sn source. An alternative route is based on $SnCl_4$,[41,42] which has the advantage of being favored in certain industrial tools. The SnD_4 precursor was initially demonstrated in combination with digermane (Ge_2H_6),[31] but subsequent work has shown that trigermane (Ge_3H_8) is ideally compatible with SnD_4,[43] leading to a nearly equal incorporation efficiency for Ge and Sn. This makes it very simple to control the film composition by varying the precursor gaseous mixture. While stannane, SnH_4, is unstable, deuteration increases stability to the point that epitaxy applications become feasible. Long-term storage of SnD_4 for commercial applications has

also been demonstrated.[44] The chemistry and applications of Group IV hydrocarbon analogues has been recently reviewed by Rivard.[45]

The alternative $SnCl_4$ precursor is used in combination with Ge_2H_6 as the Ge source.[41,42] In a typical growth experiment the gas ratio is held constant and the film compositions are varied by changing the growth temperature[46] while keeping a fixed excess of Ge_2H_6 relative to $SnCl_4$, which in the case of Ref. 46 was as high as $p_{Ge2H6}/p_{SnCl4} = 220$. This indicates that the reactivities of the two precursors are not compatible, leading to minimal conversion of the Ge_2H_6 starting material to solid product, which makes the process inefficient and costly. It is speculated that the large Ge_2H_6 excess used in this process enhances the reactivity of $SnCl_4$ at the low temperatures needed for the substitutional incorporation of Sn. From a reaction mechanism perspective, it is possible that an intermediate step during depositions produces transient SnH_mCl_{4-m} species (m=1-4), which are dramatically less stable than $SnCl_4$ and are therefore better Sn delivery sources.

It is known that $SnCl_4$ acts as a chlorinating agent of Ge_2H_6 when the two molecules are combined in a closed system,[47] readily producing Ge_2H_5Cl and $SnHCl_3$. The latter is highly unstable and eliminates HCl at room temperature, as demonstrated in control experiments conducted in the Kouvetakis labs. This indicates that a ligand exchange pathway is favored in direct reactions of Ge_2H_6 and $SnCl_4$ molecules under equilibrium conditions. While CVD is a non-equilibrium process due to the dynamic removal of the reaction components, the large $Ge_2H_6/SnCl_4$ ratio employed in the $SnCl_4$ process may generate a pseudo-equilibrium environment that favors the formation of the

unstable SnH_mCl_{4-m} intermediates. The rate of formation may be further increased under the 60 mbar reaction pressure employed in the CVD work of von den Driesch *et al.*, thereby explaining the ability of $SnCl_4$ to deposit Sn at low temperatures despite the relatively high strength of the Sn-Cl bond (0.33 eV).[36,46] A possible mechanism leading to Sn incorporation under these circumstances would involve the following reactions:

$$Ge_2H_6 + SnCl_4 \Rightarrow Ge_2H_5Cl + SnHCl_3 \quad (1)$$

$$Ge_2H_6 + SnHCl_3 \Rightarrow Ge_2H_5Cl + SnH_2Cl_2 \quad (2)$$

$$SnH_2Cl_2 \Rightarrow 2HCl + Sn\ (atoms) \quad (3)$$

By contrast, in the SnD_4/Ge_3H_8 approach, the requirement of excess Ge precursor is eliminated. This leads to a significant decrease in process cost and eliminates waste of expensive Ge, which is considered a rare element with limited global supply.[48] Furthermore, the decoupling of growth temperature and Sn concentration under this method implies that the growth temperature can be freely adjusted to maximize crystal quality, and is not constrained by stoichiometry requirements. The composition control obtained by tuning precursor ratios rather than temperature may also represent a more suitable method for fabricating devices with more complex layer structures that require precise tuning of band gap vs. composition. For these reasons, the SnD_4/Ge_3H_8 system is a more promising route to high-Sn $Ge_{1-y}Sn_y$ alloys, and the work presented here is based on this approach.

The initial appeal of the CVD approach to $Ge_{1-y}Sn_y$ films was the finding that the films grow directly on Si substrates with nearly complete strain relaxation. However, subsequent research showed that at the lower temperatures required to achieve Sn concentrations y > 5%, the films are prevented from fully relaxing the mismatch strain with the Si lattice. This, combined with the reduced growth rates, limits the overall thickness that can be achieved, ultimately diminishing the device potential of these materials on Si. A solution of this problem is the insertion of pure Ge buffer layers, which drastically reduce the starting lattice mismatch between the Si(100) substrate and the film.[49] This means that strain relaxation can be achieved with a much lower dislocation density, which facilitates the growth of thick films and reduces the non-radiative recombination velocities at the film-buffer interface. A number of groups have utilized this approach to fabricate *n*-Ge/*i*-$Ge_{1-y}Sn_y$/*p*-Ge heterostructure LEDs in which the GeSn active layers are ensconced by *p*- and *n*-type Ge electrodes.[33,35,50-54] A drawback of such designs; however, is the formation of two defected $Ge_{1-y}Sn_y$/Ge interfaces that act as carrier recombination sites, adversely affecting the emission efficiency of the devices. Previous work in this area was focused on the fabrication of enhanced performance LEDs by adopting improved *n*-Ge/*i*-$Ge_{1-y}Sn_y$/*p*-$Ge_{1-z}Sn_z$ designs containing a single defected interface. In this case, significantly stronger light emission was achieved from active $Ge_{1-y}Sn_y$ layers with compositions up to y = 0.11.[37] Here this approach is extended to demonstrate *n*-Ge/*i*-$Ge_{1-y}Sn_y$/*p*-$Ge_{1-z}Sn_z$ structures with y ~12-14 %.

The samples produced in this study were grown on Ge-buffered Si substrates. These buffers were deposited directly on 4” Si(100) wafers with a thickness of ~1 μm

using the Ge_4H_{10} precursor. They were doped *in situ* by adding 2% $P(GeH_3)_3$ in relation to the amount of Ge_4H_{10} in the reaction mixture, yielding active donor concentrations of 2×10^{19} cm^{-3}.[55] The intrinsic $Ge_{1-y}Sn_y$ layers were grown upon quadrants cleaved from the doped Ge-buffered Si(100) wafers. Prior to growth, the samples were cleaned by dipping in an aqueous HF bath and then loaded into the UHV-CVD reactor under a flow of H_2 at a background pressure of 200 mTorr. Immediately thereafter, a Ge seed layer was deposited on the wafer surface at 340 °C using Ge_3H_8/H_2 mixtures 1.5% by volume. This step produced a clean and uniform template devoid of structural flaws and lattice strains, allowing optimal epitaxy of subsequent intrinsic layers of $Ge_{1-y}Sn_y$ alloys. As indicated above, these were grown using gas mixtures containing appropriate concentrations of Ge_3H_8 and SnD_4. The compounds were combined in a 3.0 L ampule and diluted with research-grade H_2 to a final pressure of 760 Torr. In a typical run the Ge_3H_8 partial pressure in the mixture was kept constant at 9 Torr, while that of SnD_4 was varied from 2.9 - 3.5 Torr, yielding 0.107 - 0.126 Sn atoms relative to Ge atoms in the gas phase. These formulations produced alloys with Sn contents ranging from 12 - 13.7%, respectively, indicating that the Ge and Sn content in the films closely reflects the mole fraction of the gaseous mixtures. As such, it can be seen that the amount of Sn incorporated in the epilayer during growth is nearly stoichiometric. The composition control afforded in this case is facilitated by the similar reactivity of the co-reactants, yielding samples with well-defined and reproducible stoichiometries.

The fabrication of $Ge_{1-y}Sn_y$ layers with y = 0.12 - 0.137 was initiated at temperatures ranging from 280 – 270 °C, respectively. The growth was allowed to

proceed for a sufficient time to produce nucleation layers of the target material at low temperatures, in order to ensure substitutional incorporation of the entire Sn content. After this initial step, the temperature was raised slowly by 5 – 10 $^{\circ}$C and kept constant for the remainder of the experiment. The slight increase facilitated further strain relaxation in the growing layers, generating a more facile template upon which further growth can proceed at a faster rate. By following this procedure, it was possible to obtain uniform films in the target composition with thicknesses up to 430 nm. Due to the large final thickness, high degrees of strain relaxation were observed in all cases, a factor which promotes direct gap behavior. Finally, the device structures were completed by the growth of a top contact layer consisting of a $Ge_{1-z}Sn_z$ alloy that was doped *in situ* using B_2H_6. The $Ge_{1-z}Sn_z$ *p*-layers of the representative devices discussed here had lower Sn contents of 6, 10, and 8% than the corresponding 12, 12.8, 13.7% Sn of the active layers. This composition choice was made to increase carrier confinement in the active layer and to minimize reabsorption of the emitted light, while promoting pseudomorphic growth between the two materials in a given device.

2.3 Results and Discussion

2.3.1 Structural Analysis

The fabricated diodes bear many features in common with similar devices reported earlier spanning Sn compositions from y = 0.05 - 0.11.[37,56] The active $Ge_{1-y}Sn_y$

layer is mostly relaxed relative to the Ge buffer, and the strain misfit is accommodated by the formation of defects confined to the *n*-Ge/*i*-$Ge_{1-y}Sn_y$ interface. The top *i*-$Ge_{1-y}Sn_y$/*p*-$Ge_{1-z}Sn_z$ interface is fully strained and defect-free due to the absence of strain-induced defects, as evidenced by cross-sectional scanning transmission electron microscopy

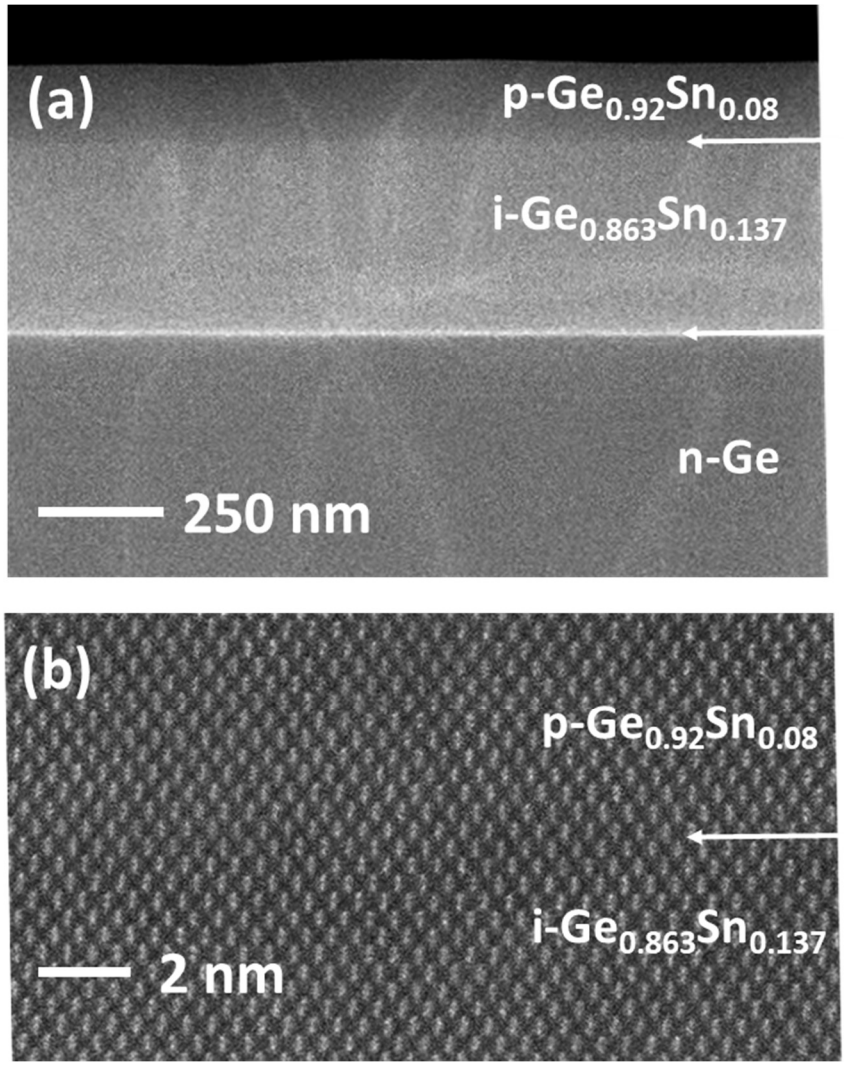

Figure 5: (a) XSTEM MAADF image of a *p*-*i*-*n* device comprising an *n*-Ge bottom contact, *i*-$Ge_{0.863}Sn_{0.137}$ active layer and *p*-$Ge_{0.92}Sn_{0.08}$ top electrode. The dark and light contrast in the image is consistent with different Sn contents in the layers. The uniform contrast within each layer indicates compositional homogeneity. (b) High-resolution image of the *p*-GeSn/*i*-GeSn interface showing no defects due to pseudomorphic growth.

(XSTEM) and XRD studies. Figure 5 shows representative XSTEM micrographs from a sample comprising a *n*-Ge/*i*-$Ge_{0.863}Sn_{0.137}$/*p*-$Ge_{0.92}Sn_{0.08}$ device stack. Panel 5(a) is a medium angle annular dark field (MAADF) image of the entire device. The intensity contrast in the image is sensitive to both atomic mass (Z-contrast) and strain, and therefore clearly delineates the active and passive layers due to their composition and strain differences. The layers are flat and exhibit thicknesses of ~340 and 140 nm, respectively. Furthermore, the uniform contrast within the layers indicates homogenous compositions throughout. This observation also provides further evidence that the slight temperature ramp employed during growth of the active layer did not lead to any compositional variations. Figure 5(b) is a high-resolution MAADF image of the top interface showing a defect-free microstructure due to the in-plane lattice matching of the *i-p* layers. The bottom *n-i* interface (not shown) contains 60° dislocations and short stacking faults penetrating down a short distance into the Ge buffer layer, as expected due to the relaxation of the *i*-layer. Figure 6 shows (224) reciprocal space maps of the same sample featuring the various peaks of the device layers and the buffer. The position of the *i*-layer peak is slightly below the relaxation line, indicating the presence of a residual compressive strain. The resultant in-plane and out-of-plane lattice parameters of the $Ge_{0.863}Sn_{0.137}$ alloy are measured to be a = 5.7304 Å and c = 5.7836 Å respectively. These are used to derive (via standard elasticity theory) a relaxed cubic cell constant a_0 = 5.761 Å, which implies that the strain relaxation reaches 70%. In contrast to the *n*/*i* interface, the XRD maps show that the top *p*-layer is fully strained to the *i*-layer, as evidenced by the vertical alignment of their (224) peaks. This is consistent with the dearth of interface

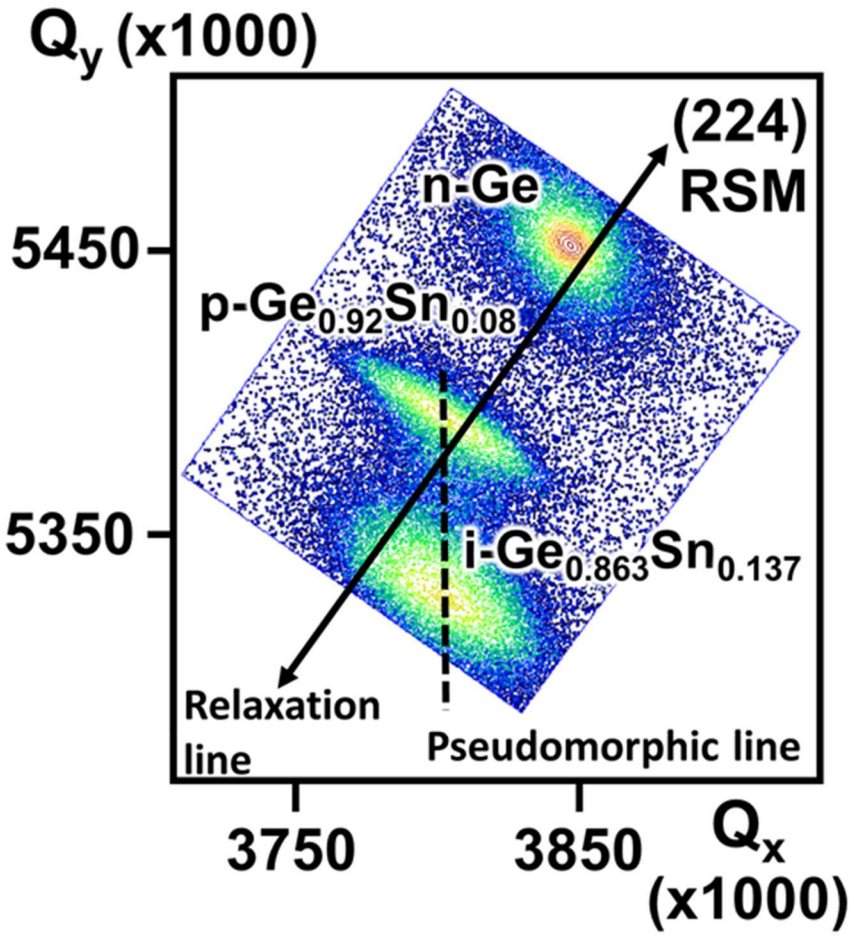

Figure 6: (224) reciprocal space maps of a *n*-Ge/*i*-$Ge_{0.863}Sn_{0.137}$/*p*-$Ge_{0.92}Sn_{0.08}$ diode. The *p*- and *i*-layers are nearly lattice matched in the plane of growth as evidenced by the vertical alignment of the peaks, indicated by the dashed pseudomorphic line in the figure.

defects in Figure 5(b). Fortuitously, the *p*-layer is nearly cubic with a = 5.728 Å and c = 5.717 Å as seen by the relaxation line passing near the center of the XRD peak. Note that the analogous devices *n*-Ge/*i*-$Ge_{0.88}Sn_{0.12}$/*p*-$Ge_{0.94}Sn_{0.06}$ and *n*-Ge/*i*-$Ge_{0.872}Sn_{0.128}$/*p*-$Ge_{0.90}Sn_{0.10}$ fabricated in this study also contain a single defected interface between the Ge buffer and the intrinsic $Ge_{0.88}Sn_{0.12}$ and $Ge_{0.872}Sn_{0.128}$ layers. The latter exhibit large thicknesses of 360 nm and 430 nm respectively, and are found to be ~ 70 % relaxed while the corresponding *p*-type counterparts $Ge_{0.94}Sn_{0.06}$ (270 nm) and $Ge_{0.90}Sn_{0.10}$ (150 nm) are

fully strained and lattice matched. This is likely a result of the ultra-low temperature of 275 - 290 °C employed in the deposition of the *p*-type materials in this case.

The optical properties of the resulting diodes were used to excite electroluminescence. A typical spectrum from the 12% Sn sample is plotted in Figure 7 and compared with that of a 10.5% Sn device from Ref. 37. The plots in both samples were recorded using a thermoelectrically cooled PbS detector, which is the reason for the relatively poor signal-to-noise ratio seen in the plots. By fitting the experimental data

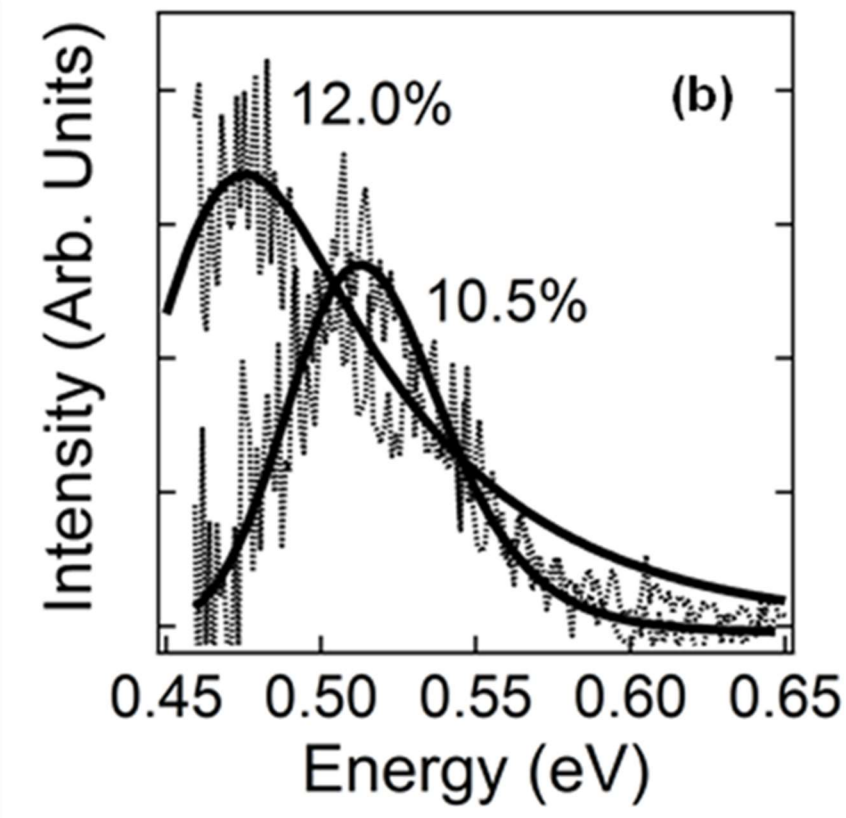

Figure 7: EL plot of the 12% device is compared with that of a 10.5% analogue described in prior work. The noise in the spectra is due to the thermoelectrically cooled PbS detector used in the experiment. The solid lines represent EMG fits to the data.

with exponentially modified Gaussian (EMG) functions as described in Ref. 57, the peak position for the 12% Sn device was determined to be at 0.47 eV (2640 nm), in good agreement with band gap-composition relationships derived for $Ge_{1-y}Sn_y$ alloys in previous studies.[6] Furthermore, the higher intensity observed for the 12% Sn spectrum is consistent with the expectation that the alloy becomes more direct with increasing Sn content. Note that the emission wavelength of the 12.8% and 13.7% Sn samples is beyond the 2700 nm cutoff of the detector and thus could not be measured in this study. Nevertheless, the relatively low dark currents of the samples, compared to the 12% analogue suggest that the optical quality should be comparable. In this connection it is noted that the onset of the EL peak for the 12.8% sample was detected indicating that the device should perform as expected.

A possible limit to the strategy of using pure Ge buffer layers was encountered when attempting to grow alloys with Sn concentrations $y > 0.14$, for which the mismatch strain reaches 1.9%. This produced highly defected materials, making it difficult to fabricate devices with a performance comparable to the $y < 0.14$ counterparts. This issue was addressed by introducing an *n*-doped $Ge_{1-x}Sn_x$ intermediate layer between the active material and the Ge buffer to mitigate the starting lattice mismatch. The first example of this type of device was reported by Gallagher *et al*., who produced diodes in which the three layers were $Ge_{1-y}Sn_y$ alloys with $y \approx 0.07$. These homo-structures yielded superior electroluminescence relative to hetero-structure *n*-Ge/*i*-$Ge_{1-y}Sn_y$/*p*-$Ge_{1-z}Sn_z$ analogues due to the absence of interfacial defects.[56]

In this study *n*-$Ge_{1-x}Sn_x$/*i*-$Ge_{1-y}Sn_y$/*p*-$Ge_{1-y}Sn_y$ devices with y = 0.15 - 0.16 active layers were produced on Ge buffered Si. The samples utilized *n*-type $Ge_{1-x}Sn_x$ intermediate layers with Sn contents x = 0.11-0.12 which are lower than those of the active layer. Furthermore, the Sn content *x* was selected to be close enough to *y* to guarantee no strain relaxation at the *n*-*i* interface and at the same time limit the compressive strain in the active layers. Growth of the $Ge_{1-x}Sn_x$ layer was achieved using

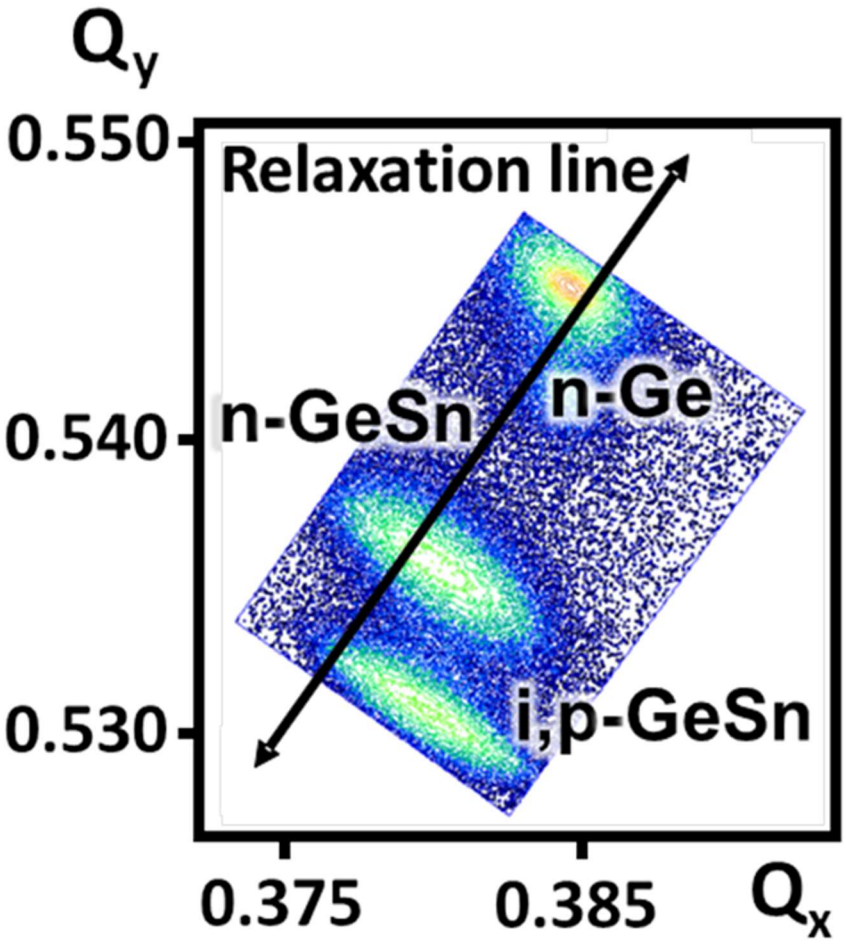

Figure 8: HR-XRD reciprocal space maps of a *n*-$Ge_{0.89}Sn_{0.11}$/*i*-$Ge_{0.85}Sn_{0.15}$/*p*-$Ge_{0.85}Sn_{0.15}$ diode. The combined peaks of the *i*- and *p*- layers are vertically aligned with that of the *n*-layer indicating pseudomorphic growth. The *n*-layer is 80 % relaxed as indicated by the position of the (224) peak below the relaxation line.

the SnD_4/Ge_3H_8 method described above for the 12 % device. The $P(SiH_3)_3$ single source precursor was used to dope the material *n*-type with 9×10^{18} cm^{-3} active carriers. The surface of the films was subjected to chemical cleaning using HF/H_2O solutions and the samples were reinserted into the UHV-CVD chamber for the deposition of the active layers. These were grown at 260-265 °C using a Ge_3H_8/SnD_4 mixture with a Sn/Ge element ratio of 0.16. The *p-i-n* stacks were completed by *in situ* doping the final 50-60 nm of the layer *p*-type using B_2H_6.

Figure 8 shows XRD reciprocal space maps of the (224) reflections for the *n*-$Ge/Ge_{0.89}Sn_{0.11}$/*i*-$Ge_{0.85}Sn_{0.15}$/*p*-$Ge_{0.85}Sn_{0.15}$ samples featuring an intrinsic $Ge_{0.85}Sn_{0.15}$ layer grown on a *n*-type $Ge_{0.89}Sn_{0.11}$ spacer and capped with a *p*-type $Ge_{0.85}Sn_{0.15}$ top electrode. The maps are well defined, narrow and symmetrical. Their vertical alignment indicates close lattice matching of the layers within the plane of growth, corroborating the notion that the relatively large lattice constant of $Ge_{0.89}Sn_{0.11}$ (a = 5.7285 Å) has allowed the active layer to grow pseudomorphically. An additional factor that may contribute to the pseudomorphic growth is the ultra-low temperatures of 260 °C utilized for the growth of these highly metastable alloy compositions. Furthermore, the XRD data suggest that the crystal quality of the $Ge_{0.85}Sn_{0.15}$ films is similar to that $Ge_{0.88}Sn_{0.12}$ analogues grown directly on virtual Ge substrates, as evidenced by comparable FWHM values of the (004) rocking curves of the two samples.

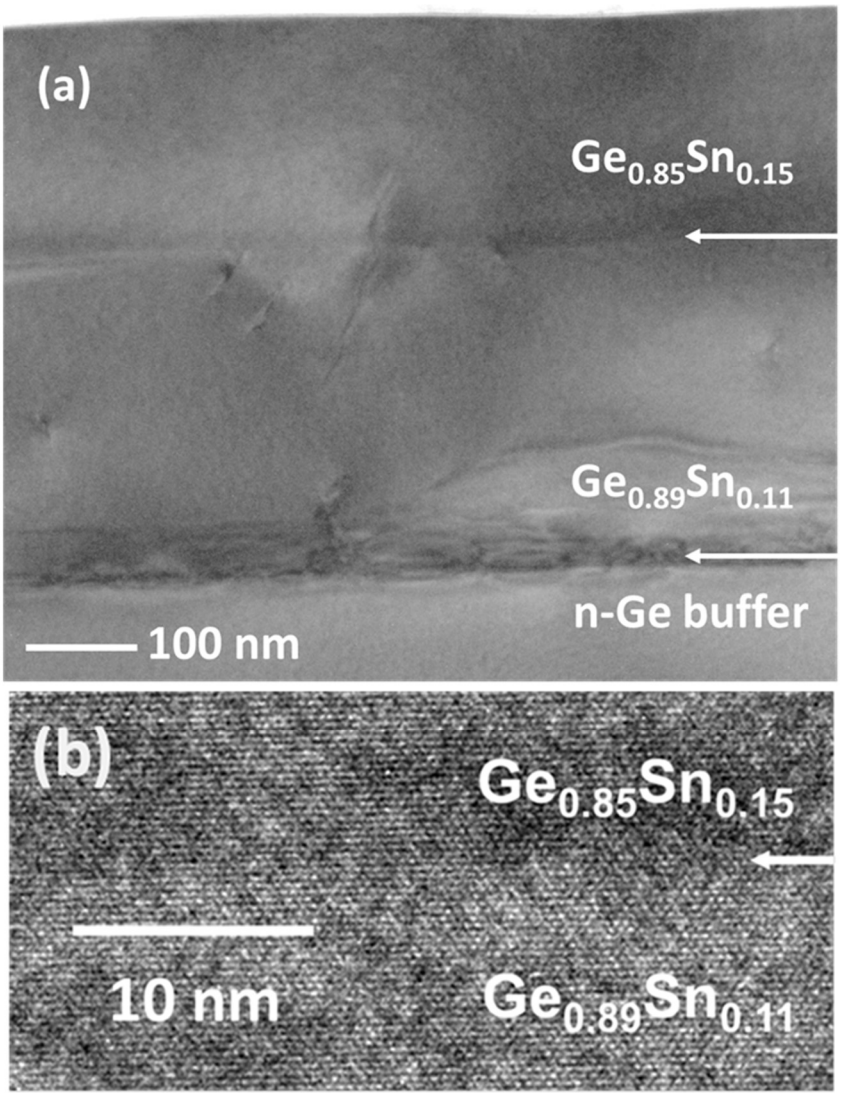

Figure 9: XTEM micrographs of the *n*-Ge/*n*-$Ge_{0.89}Sn_{0.11}$/*i*-$Ge_{0.85}Sn_{0.15}$/*p*-$Ge_{0.85}Sn_{0.15}$ diode. (a) Diffraction contrast view of the entire device showing the various device layers and corresponding interfaces marked by arrows. (b) High resolution image of the bottom *n*-$Ge_{0.89}Sn_{0.11}$/*i*-$Ge_{0.85}Sn_{0.15}$ interface showing defect free pseudomorphic growth.

Complementary characterizations of strain and structure of the above 15 % Sn devices were conducted by XTEM. A representative micrograph is shown in Figure 9(a) illustrating the entire device stack including the buffer layer, the *p*-*i*-*n* epilayers, and their respective interfaces. The data reveal that the bulk crystal is largely devoid of threading

dislocations in spite of the relatively high Sn contents of 15 %. The $Ge/Ge_{0.89}Sn_{0.11}$ bottom interface, marked by an arrow, is defective due to strain relaxation effects, while the upper *n*-$Ge_{0.89}Sn_{0.11}$/*i*-$Ge_{0.85}Sn_{0.15}$ analogue is defect free as evidenced by the uniform contrast in the vicinity of the top arrow. This is corroborated by high resolution images which show direct correspondence of the [111] lattice fringes between the two layers with no evidence of dislocations or other types of defects confined to the interface plane as illustrated in Figure 9(b). The top interface between the intrinsic and *p*-type $Ge_{0.85}Sn_{0.15}$ is not visible in the XTEM images because of the flawless integration and continuous transition afforded by the homo-epitaxial character of the constituent layers (each containing the same 15% Sn). Finally, note that XRD measurements of the *n*-Ge/*n*-$Ge_{0.88}Sn_{0.12}$/*i*-$Ge_{0.84}Sn_{0.16}$/*p*-$Ge_{0.84}Sn_{0.16}$ device revealed similar structural and strain properties as the 15% Sn analogue, also indicating pseudomorphic growth of highly crystalline active and passive layers. This further confirms that the insertion of an intermediate layer between the active components and the Ge platform makes it possible to integrate ultrahigh Sn content materials with large thickness and suitable crystal quality to produce working diodes.

2.3.2 Electronic Properties

The I-V characteristics of the fabricated diodes are shown in Figure 10. In both cases, the bottom contacts were made to the *n*-Ge layer, while the top contacts were deposited on the *p*-layer. Figure 10(b) shows I-V curves indicating that the dark currents

are significantly higher than what has been observed in lower Sn content diodes. This might indicate a significant degradation of the material's quality past the y ~ 14% limit, but the XTEM data in Figure 9 and a closer examination of the electrical results suggest otherwise. Figure 11 compares the reverse-bias currents of devices grown of pure Ge and $Ge_{1-x}Sn_x$ buffer layers depicted as $Ge/Ge_{1-y}Sn_y/Ge_{1-z}Sn_z$ and $Ge_{1-x}Sn_x/Ge_{1-y}Sn_y/Ge_{1-z}Sn_z$,

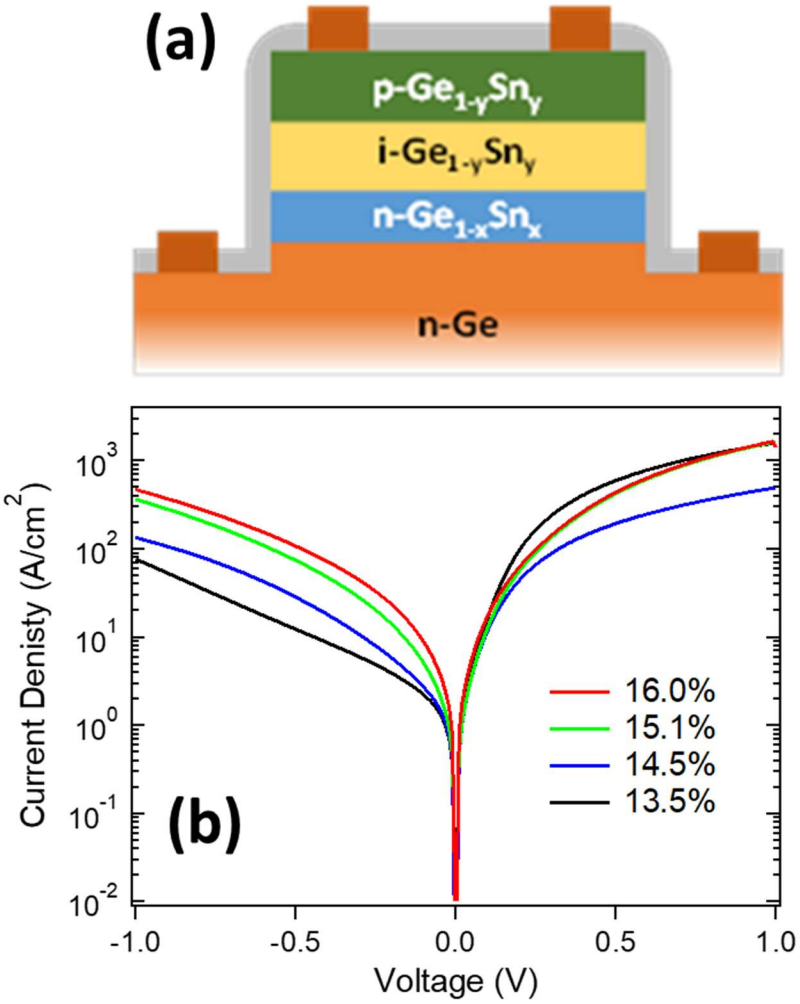

Figure 10: (a) Schematic representations of *n*-Ge/*n*-$Ge_{1-x}Sn_x$/*i*-$Ge_{1-y}Sn_y$/*p*-$Ge_{1-y}Sn_y$ diode structure in which the bottom contacts are made to the *n*-Ge layer. b) I-V curves obtained from devices with above diode design consisting of y = 0.135 - 0.16 active layers.

respectively. There is a drastic increase by almost two orders of magnitude in the samples grown on $Ge_{1-x}Sn_x$ buffers, even though in this case the interface with the intrinsic layer in most cases is pseudomorphic and defect free (see Figure 9), whereas in the pure Ge case it is relaxed and highly defected. While the higher reverse biased currents could be due to an increase in point defects, rather than the extended defects associated with strain relaxation, note that for the *same* intrinsic layer Sn concentrations *y*, the reverse bias currents are drastically higher when the *n*-type layer consists of a $Ge_{1-x}Sn_x$ alloy. This suggests that point defects in the intrinsic layer are not responsible for the higher reverse-bias current. Furthermore, for the higher values of *y* the corresponding value of *x* is about 11%, but when $Ge_{0.89}Sn_{0.11}$ is used as an intrinsic layer in devices grown on pure Ge, the reverse-bias currents are low. In other words, there is no device evidence for a higher

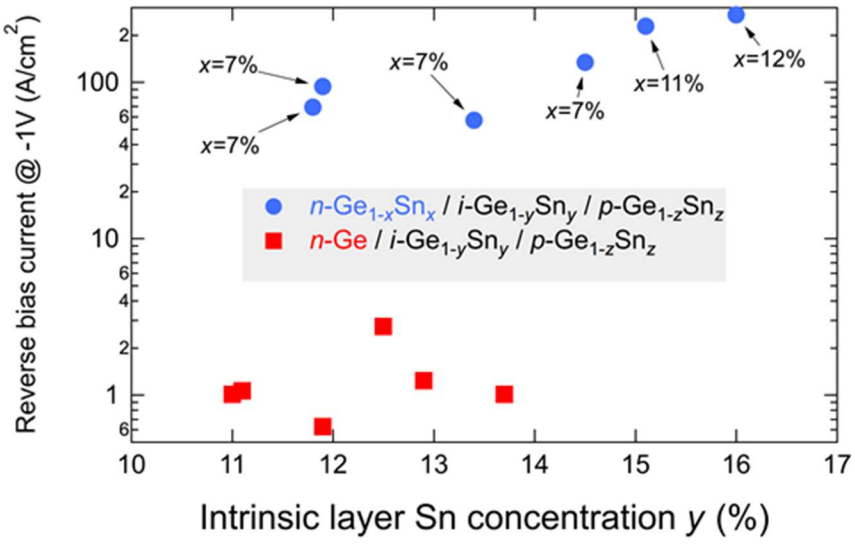

Figure 11: Comparison of diode currents at -1.0 V bias between Ge/GeSn/GeSn (red squares) and GeSn/GeSn/GeSn (blue circles) diodes. Note the dramatic increase in reverse bias currents as the *n*-layer approaches direct gap conditions, even though the *n-i* interface is less defected. The higher currents are assigned to band-to-band tunneling.

density of point defects associated with the Sn concentration in any of the device components. The explanation for the higher reverse bias currents is band-to-band-tunneling, which, as reported by Schulte-Braucks *et al.,*[58] is drastically enhanced when the *n*-type layer is a direct gap material. The key difference between the diodes in Figure 11 is in one case the *n*-type layer is pure Ge, which is indirect, but in the other case it is $Ge_{1-x}Sn_x$, which is a direct-gap alloy. This explains the dramatically increased tunneling current.

2.3.3 Band Gap Analysis

It has been demonstrated that the Ge_3H_8/SnD_4 route makes it possible to synthesize $Ge_{1-y}Sn_y$ alloys with Sn concentrations as high as y = 16% that can be incorporated into working devices. At high Sn-concentrations the main factor limiting the amount of Sn that can be incorporated—while maintaining the device integrity—is the same found at lower Sn-concentrations, namely the mismatch strain between the $Ge_{1-y}Sn_y$ layer and the underlying buffer layer. Provided that this mismatch strain is kept moderately low, good quality films can with Sn concentrations as high as 16% can be grown. This suggests that even higher Sn concentrations may be attainable by this method by growing successive layers of ever increasing Sn concentrations, following a process similar to the early efforts to grow Ge on Si by using intermediate $Ge_{1-x}Si_x$ layers of graded composition.[59] The ultimate limit of this approach may be given by the ever-decreasing growth temperature needed to incorporate an increasing amount of Sn.

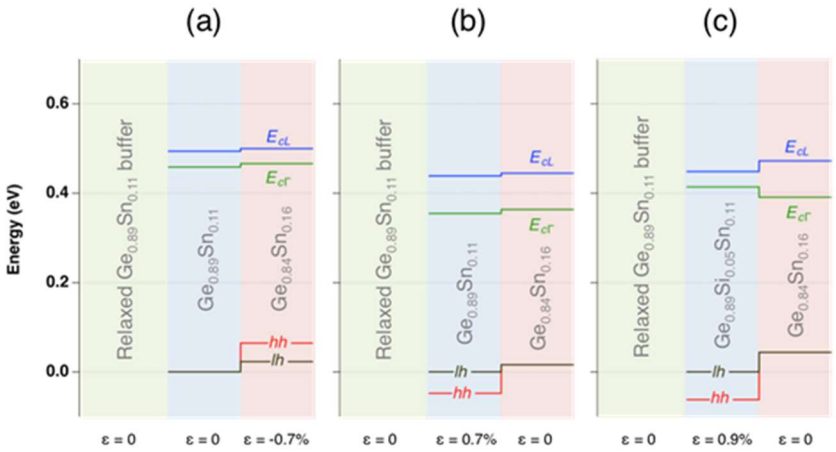

Figure 12: Calculated band lineup at different GeSn/GeSiSn pseudomorphically strained heterostructures. E_{cL}: conduction band minimum at the L-point of the BZ. $E_{c\Gamma}$: conduction band minimum at the Γ-point of the BZ. *hh* (*lh*): heavy (light) hole band at the Γ-point of the BZ. The strain is indicated below each of the layers.

From an optical perspective, a disadvantage of the "graded" layer approach is that the intrinsic layer with a higher Sn concentration is under compressive strain, which makes the semiconductor less direct. Figure 12(a) shows a band diagram for a $Ge_{0.89}Sn_{0.11}/Ge_{0.84}Sn_{0.16}$ heterostructure in which the strained $Ge_{0.84}Sn_{0.16}$ alloy is direct by only 33 meV. In addition, the structure is Type-II, which is unsuitable for light emission. A possible solution to this problem would be to grade the buffer layer to match the intrinsic layer Sn-concentration, so that the intrinsic layer is relaxed and the *n*/*p* layers are under tensile strain. The corresponding band lineup is shown in Figure 12(b), and the band gap "directness" has markedly improved to 81 meV. However, the heterostructure remains Type-II. A possible way to achieve a Type-I alignment is to add Si to the barrier layer, as shown in Figure 12(c). However, this increases the strain in this layer, suggesting that the desired Type-I alignment may require very thin layers to avoid strain relaxation.

While the calculations in Figure 12 provide some guidance for future advances, it is important to stress that they depend on some very poorly known parameters, such as the band offsets in the Si-Ge-Sn system and the compositional dependence of the band gaps in the ternary $Ge_{1-x-y}Si_xSn_y$ alloys. In addition, several deformation potentials are needed for the alloy system, and these are usually taken as linear interpolations between experimental or theoretical values for the elemental semiconductors. The general scheme for the calculations was given in Ref. 60. The compositional dependence of the direct and indirect edges in $Ge_{1-y}Sn_y$ alloys was taken from Ref. 6, and for the ternary $Ge_{1-x-y}Si_xSn_y$ a quadratic polynomial with a bowing parameter b^{SiSn} = 14 eV was used.[61] For the deformation potentials the values recommended in Refs. 57 and 62 were used. The band offsets depend on the relative alignment of the average valence band value $E_{v,av}$, as defined by Van de Walle.[63] In Refs. 64 and 60, and in many subsequent papers modeling heterostructures containing $Ge_{1-y}Sn_y$ and $Ge_{1-x-y}Si_xSn_y$ layers, the relative alignment of $E_{v,av}$ for Si, Ge, and α-Sn was taken from a simplified theory of band offsets by Jaros.[65] This was done due to the dearth of theoretical and experimental data for α-Sn. More recently, however, Li *et al*.[66] published new *ab initio* calculations of band offsets that imply $E_{v,av}$ values quite different from those previously calculated. If one conventionally assumes $E_{v,av}(Ge) = 0$, Li *et al*. predict $E_{v,av}(Si) = -0.755$ eV for Si, substantially larger than the value $E_{v,av}(Si) = -0.48$ eV from Jaros' theory, and also higher than Van de Walle's values $E_{v,av}(Si) = -0.53$ eV (Ref. 39) eV and $E_{v,av}(Si) = -0.68$ eV (Ref. 67). Interestingly, recent work has shown that the Type-II band alignment at a $Si_{0.70}Ge_{0.30}$/Si heterostructure, as obtained by Thewalt *et al*. from photoluminescence measurements,[68]

imply $E_{v,\mathrm{av}}(\mathrm{Si})$ = -0.800 eV, and subsequent capacitance-voltage measurements at Si/$Ge_{1-x}Si_x$ interfaces are also in very good agreement with this value.[62] These results provide strong support for Li's theoretical results. Accordingly, for a $Ge_{1-x-y}Si_xSn_y$ alloy Equation (1) is used.

$$E_{v,\mathrm{av}}(x,y) = 3(1-x-y)a_v^{\mathrm{Ge}}\frac{\left[a_0(x,y)-a_0^{\mathrm{Ge}}\right]}{a_0^{\mathrm{Ge}}} + x\left\{E_{v,\mathrm{av}}(\mathrm{Si}) + 3a_v^{\mathrm{Si}}\frac{\left[a_0(x,y)-a_0^{\mathrm{Si}}\right]}{a_0^{\mathrm{Si}}}\right\} + y\left\{E_{v,\mathrm{av}}(\mathrm{Sn}) + 3a_v^{\mathrm{Sn}}\frac{\left[a_0(x,y)-a_0^{\mathrm{Sn}}\right]}{a_0^{\mathrm{Sn}}}\right\} \quad (1)$$

Where $E_{v,\mathrm{av}}(\mathrm{Si})$ = -0.800 eV and $E_{v,\mathrm{av}}(\mathrm{Sn})$ = 0.904 eV. The latter is obtained from the Li value $E_{v,\mathrm{av}}(\mathrm{Sn})$ = 0.852 eV after renormalizing by the same factor (0.800/0.755) that in the Ge-Si system brings theory into exact agreement with experiment. Equation (1) implies that $E_{v,\mathrm{av}}$ for the alloy is computed as a linear interpolation of the $E_{v,\mathrm{av}}$'s for Si, Ge, and α-Sn, corrected for their hydrostatic shift to account for the difference between the cubic lattice parameter $a_0(x,y)$ of the alloy and the cubic lattice parameters $a_0^{\mathrm{Si}}, a_0^{\mathrm{Ge}}, a_0^{\mathrm{Sn}}$ of the elemental semiconductors. The correction terms contain the absolute valence band hydrostatic deformation potentials for Si (a_v^{Si}) , Ge (a_v^{Ge}), and α-Sn (a_v^{Sn}). Where a_v^{Si} = 2.24 eV, a_v^{Ge} =2.10 eV and a_v^{Sn} = 1.49 eV. These values were obtained by multiplying the *ab initio* predictions of Li *et al*. (Ref. 69) times 0.94, so that the band gap deformation potential in Ge is matched exactly. The procedure is described in Ref. 62. Recently, Yamaha *et al*. published band offset measurements at Ge/$Ge_{1-x-y}Si_xSn_y$ interfaces.[70] For a Ge/$Ge_{0.44}Si_{0.41}Sn_{0.15}$ alloy the valence band offset was found to be 0.11

eV (higher on the Ge side), which should be compared with 0.15 eV predicted in a calculation of the heterostructure using Equation (1) for $E_{v,av}(x,y)$. Moreover, if the Si concentration is reduced to 39% in order to match the measured strain exactly, a valence band offset of 0.13 eV is predicted, in even better agreement with the measurements. This level of agreement can be considered very satisfactory given the sensitivity to the compositions and the fact that the band offsets were extracted by approximating the valence band density of states as a linear function of energy near the band edge, rather than by trying to model it using realistic expressions. Nevertheless, it is apparent that further work is needed to determine the validity of Equation (1) as well as the compositional dependence of band gaps in the $Ge_{1-x-y}Si_xSn_y$ layers, which affects strongly the range of Type-I structures that can be obtained. In order to investigate the feasibility of $Ge_{1-x-y}Si_xSn_y$ cladding layers, depositions of high Sn content $Ge_{1-x-y}Si_xSn_y$ films were performed.

2.4 High Sn Content $Ge_{1-x-y}Si_xSn_y$ Materials and Insights into Si-Sn Bandgap Bowing

2.4.1 Routes Toward High Sn Content $Ge_{1-x-y}Si_xSn_y$ Films

Synthesis of $Ge_{1-x-y}Si_xSn_y$ films was achieved using the same UHV-CVD batch reactor described in section 2.2 above. The films were deposited onto Ge buffered Si substrates produced in a separate GSME system described elsewhere.[71] Before use the Ge/Si substrates underwent an *ex situ* wet etch in a 5% HF/DI water solution to remove

Table 1: List of Sn-rich $Ge_{1-x-y}Si_xSn_y$ films and experimental growth conditions

Sample	Film Sn Content	Film Si Content	Growth Temp. (°C)	Thick. (nm)	Strain %	Relaxation %	Doping
Ge715SiSn	0.105	0.05	290	225	-0.8544	33.66	$2.9x10^{19}$
Ge568SiSn	0.11	0.05	290	380	-0.4568	63.40	$2.4x10^{19}$
Ge747SiSn	0.117	0.06	292	300	-0.3931	68.62	$3.4x10^{19}$
Ge564SiSn	0.12	0.055	295	800	-0.4722	65.07	$1.7x10^{19}$
Ge735SiSn	0.135	0.06	278	175	-1.4915	8.25	$1.15x10^{19}$
Ge744SiSn	0.14	0.06	278	375	-1.5627	7.32	$2.07x10^{19}$
Ge715SiSn2	0.14	0.05	280	250	-1.7019	1.71	$7.42x10^{19}$
Ge735SiSn2	0.15	0.08	275	190	-1.6678	5.52	$2.58x10^{19}$

the native oxide, and were dried under a flow of N_2. In the UHV-CVD system, a Ge refreshing layer was deposited to produce a clean epi-ready surface. Ge_3H_8, Si_4H_{10}, and SnD_4 were selected as Ge, Si, and Sn sources, respectively. Deposition temperatures ranged from 275 – 295 °C depending on the target composition, and a pressure of 200 mTorr was used in all films. Films were grown as *n*-type materials utilizing $P(SiH_3)_3$ as a doping precursor. The resulting films, which are listed in Table 1, contain high Sn contents (y = 0.105 – 0.15) and relatively low Si contents (x = 0.05 – 0.08) which should have absorption edges in the 2200 – 2800 nm range.

2.4.2 Structural and compositional characterization of $Ge_{1-x-y}Si_xSn_y$ materials

High-resolution X-ray diffraction (HR-XRD) was used to probe the structure and crystallinity of the resulting films. Figure 13 shows a HR-XRD spectra of the highest Sn content film, $Ge_{0.77}Si_{0.08}Sn_{0.15}$. The film has a single intense peak, which can be seen at 63.7° in the 004 spectra (main panel) which indicates a monocrystalline material has been produced. The inset shows a (224) reciprocal space map (RSM) of the same material, the $Ge_{0.77}Si_{0.08}Sn_{0.15}$ peak is located directly beneath that of the Ge buffer layer along the pseudomorphic line. This indicates that the film has grown pseudomorphic to the Ge buffer layer. Pseudomorphic growth has been observed in all of the $Ge_{1-x-y}Si_xSn_y$ samples

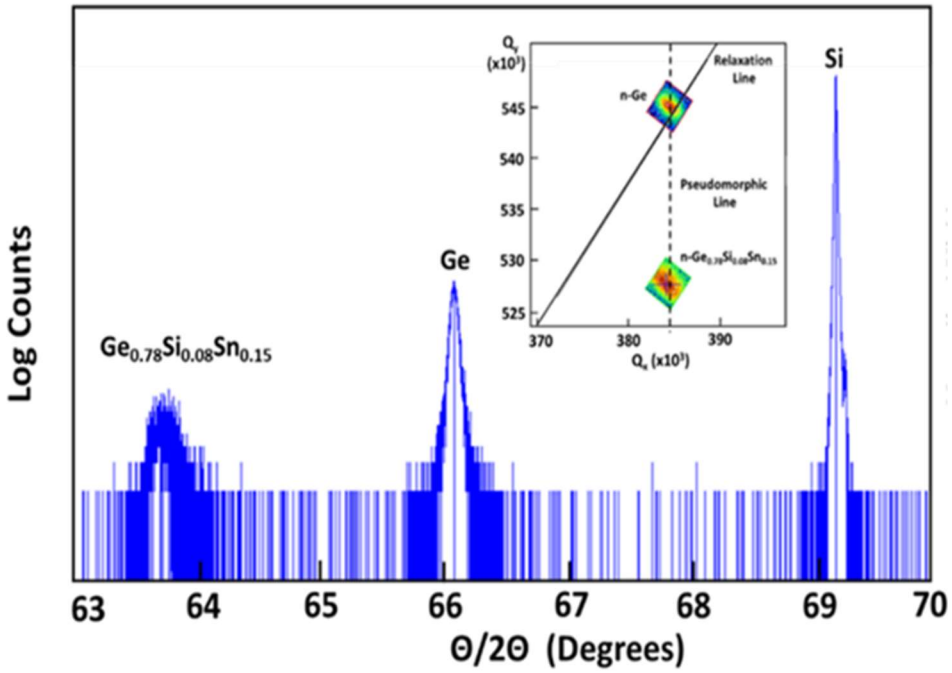

Figure 13: Main panel - HR-XRD (004) spectra of *n*-$Ge_{0.77}Si_{0.08}Sn_{0.15}$ grown on Ge buffered Si. A single distinct peak can be seen at 63.7° indicating a single crystal film was produced. Inset, (224) RSM of the same film, here the pseudomorphic nature of the film can be observed given its position along the pseudomorphic line.

with y > 0.12, even at thicknesses of 375 nm as in the case of Ge744SiSn. Comparatively, $Ge_{1-y}Sn_y$ films are observed to relax at ~200 nm. The incorporation of Si into the film is known to increase the thermal stability of the material; it may be the case that the Si also causes the material to become more resistant to relaxation under the growth conditions used.

Figure 14 shows a 2.0 MeV Rutherford backscattering (RBS) spectra of the same $Ge_{0.77}Si_{0.08}Sn_{0.15}$ film, the black trace is collected with the sample at a random angle. Here distinct peaks can be seen for the Ge, Si, and Sn signals from the epilayer. The profile of each peak is flat, and the composition is determined to be uniform throughout the layer.

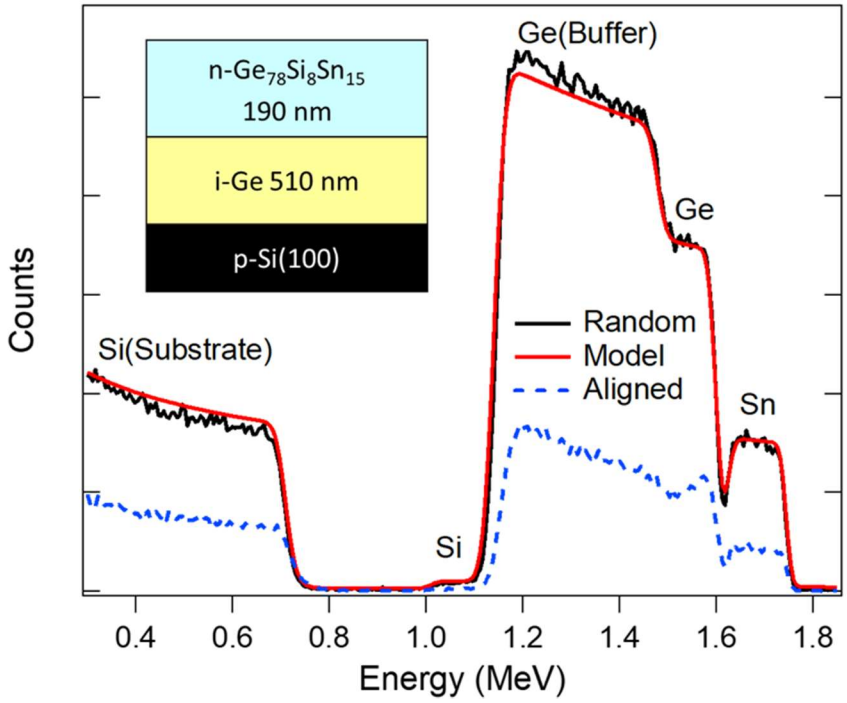

Figure 14: 2.0 MeV RBS spectra of a $Ge_{0.77}Si_{0.08}Sn_{0.15}$ film grown on a Ge/Si buffer. The black trace is the random spectrum, the blue dashed line is a channeled spectrum, and the red trace is a model of the random spectrum. Distinct peaks can be seen for the Ge, Si, and Sn peaks on the epilayer as well as the Ge and Si contribution of the Ge buffer and Si substrate respectively.

A computational model was produced (red trace) which allowed film thickness and composition to be obtained. The epilayer is modeled as $Ge_{0.77}Si_{0.08}Sn_{0.15}$, and 190 nm thick which fits well with the experimental data. The layer thickness is further corroborated via spectroscopic ellipsometry which is in good agreement with the thicknesses determined by RBS. The blue dashed line seen in Figure 14 is a channeled spectra where the sample is aligned perpendicular to the incident beam. This trace is significantly less intense than the random spectra (black trace) indicating good epitaxial alignment between the layers, providing further evidence of a monocrystalline film which compliments the HR-XRD data.

2.4.3 Photoluminescence Studies of $Ge_{1-x-y}Si_xSn_y$ Films

A range of samples with Sn contents spanning y = 0.051 – 0.15 and Si contents of x = 0.024 – 0.08 have been produced with uniform compositions and a high degree of crystallinity. PL studies were performed using a 980 nm, 400 mW laser source modulated at 191 Hz with an optical chopper. Spectra was collected using an InGaAs detector with a range of 1300 – 2300 nm and a lock-in amplifier. Figure 15 shows PL spectra of two of the high Sn content $Ge_{1-x-y}Si_xSn_y$ films produced in this study, compositions $Ge_{0.84}Si_{0.05}Sn_{0.11}$ and $Ge_{0.825}Si_{0.055}Sn_{0.12,}$ along with selected $Ge_{1-x-y}Si_xSn_y$ samples produced previously for comparison. A clear trend can be seen as Sn content increases the peak position shifts to lower energies as the energy level of both the L-point and the Γ-point decrease and the material becomes less Ge-like and shifts further into the

infrared. The second observation to be made is the dramatic increase in the peak intensity as Sn content is increased which is especially notable in the two highest Sn content films, $Ge_{0.84}Si_{0.05}Sn_{0.11}$ and $Ge_{0.825}Si_{0.055}Sn_{0.12}$. Despite their higher Si content, the two films have an extreme 3- 4 fold increase in intensity over the lower Sn content samples. This increase in intensity can be attributed to the composition crossing into the direct gap

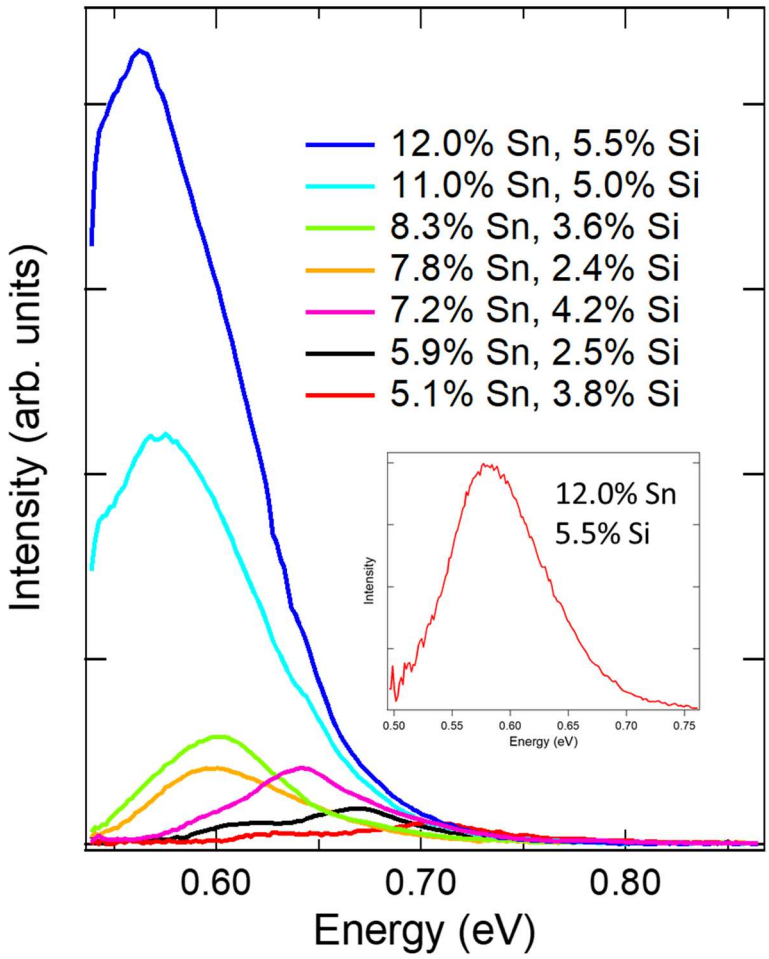

Figure 15: Photoluminescence spectra of $Ge_{1-x-y}Si_xSn_y$ materials spanning a range of compositions. Note the dramatic increase in peak intensity as Sn content increases regardless of increased Si content. The inset shows the same $Ge_{0.825}Si_{0.055}Sn_{0.12}$ film taken with a different detector so the full peak can be seen. The peak is redshifted to 0.58 eV relative to lower Sn content samples.

regime increasing the probability of photon emission. The inset of Figure 15 shows a PL spectra of just the $Ge_{0.825}Si_{0.055}Sn_{0.12}$ film alone collected using an extended InGaAs detector with a cutoff at 2500 nm. In this spectrum the entire peak profile can be seen clearly at 0.58 eV, the single peak observed in this spectra is indicative of direct or near direct gap behavior. This means that even with Si content over 5% $Ge_{1-x-y}Si_xSn_y$ is capable of direct gap behavior with as little as 12% Sn. Increasing the Si content incrementally in parallel with Sn is a sound method for transitioning toward direct gap materials while suppressing lattice mismatch between high Sn content films and underlying Ge virtual substrates. Higher Sn content samples with $y > 0.12$ did not demonstrate intense PL signals due to the large compressive strain associated with the pseudomorphic nature of the material.

2.4.4 Insights into Si-Sn Band Gap Bowing

Significant efforts have been made in the determination of bowing parameters between Group IV alloys, and these efforts are of critical importance for calculating ideal compositions to achieve direct gap behavior. In the case of Ge-Si the relationship is known to be nearly linear and there is no notable bowing observed, while in the case of Ge-Sn a bowing on the order of ~2 eV has been found experimentally.[72,73] However, the bowing of Si-Sn is significantly more difficult to deduce experimentally because of the difficulty in producing high quality $Si_{1-x}Sn_x$ alloys due to the large lattice mismatch between the two elements. Several theoretical predictions have been made for Si-Sn

bowing, though they vary widely between 3.92 eV as suggested by Moontragoon *et al*. to -5.95 eV by Sant and Schenk.[74,75] This large discrepancy in the theoretical determination of the Si-Sn bowing parameter makes it nearly impossible to calculate a predicted value for the band gap of a $Ge_{1-x-y}Si_xSn_y$ film.

In this study, $Ge_{1-x-y}Si_xSn_y$ has been used to determine Si-Sn bowing. This is a difficult process due to the three compositional dimensions of the material requiring a large selection of samples in order to produce statistically significant results. Previous

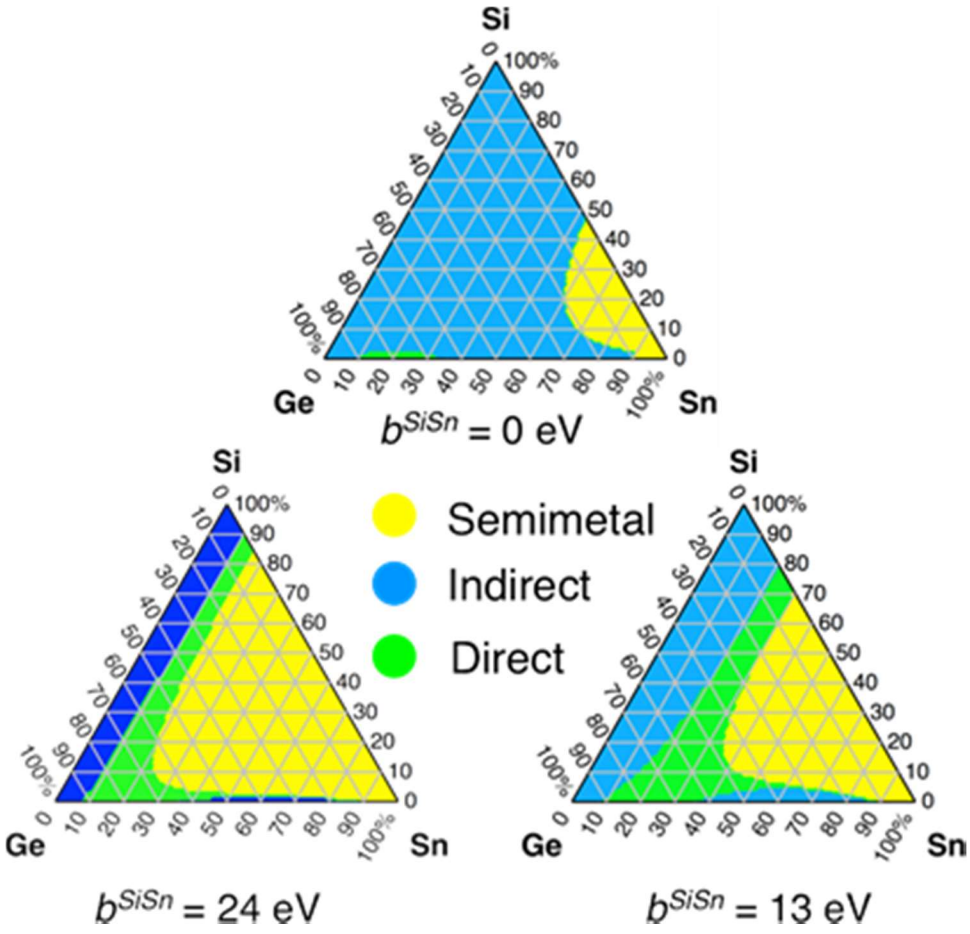

Figure 16: Three determinations of the Si-Sn bowing parameter, 0, 13, and 24 eV. The diagrams show the band gap behavior at various compositions for each bowing parameter prediction.

efforts made by D'Costa *et al*. determined the Si-Sn bowing parameter to be 13.2 eV experimentally,[62] and more recently a study by Wenday *et al*. suggested an even larger Si-Sn bowing parameter as high as 24 eV.[76] The simplest expression for the band gap energy of $Ge_{1-x-y}Si_xSn_y$ is shown in Equation (2) below.

$$E_g\,(x,y) = E_g^{Ge}(1-x-y) + E_g^{Si}x + E_g^{Sn}y - b^{GeSi}(1-x-y)x - b^{GeSn}(1-x-y)y - b^{SiSn}xy \qquad (2)$$

Where E_g denotes a band gap energy and b denotes the bowing parameter of the pertinent material. Several potential scenarios are given in Figure 16 where a linear dependence (b^{SiSn} = 0 eV) is shown along with the determinations made by both D'Costa *et al*. (b^{SiSn} = 13 eV), and Wenday *et al*. (b^{SiSn} = 24 eV). From the three plots shown it is clear that the precise determination of the Si-Sn bowing parameter is necessary in order to make accurate predictions of the band gap behavior of $Ge_{1-x-y}Si_xSn_y$ films, and large variations in the direct gap areas are notable between the three plots.

A large selection of EL and PL as well as absorption edges of $Ge_{1-x-y}Si_xSn_y$ films collected over a wide range of compositions was used in order to determine the Si-Sn bowing parameter experimentally. The results of this study are shown in Figure 17 where the blue spheres represent the band gap energies at various compositions. The light blue surface shown in the plot is a fit of the data points using Equation (2) described above, and the blue grid is the result when using b^{SiSn} = 0 eV. The value of b^{SiSn} is found to be

25.6 ± 1.9 eV by fitting of the experimental data, this is in good agreement with the determination made by Wenday *et al.* of 24 eV.

From the plot shown in Figure 17 it is clear that a large bowing parameter is needed in order to fit the experimental data. This is an exciting discovery for $Ge_{1-x-y}Si_xSn_y$ alloys as the large bowing means that at higher concentrations of Si, the band gap energy will be shifted to even lower energies as opposed to what would be expected through linear interpolation. The large bowing parameter of Si-Sn also means that there is

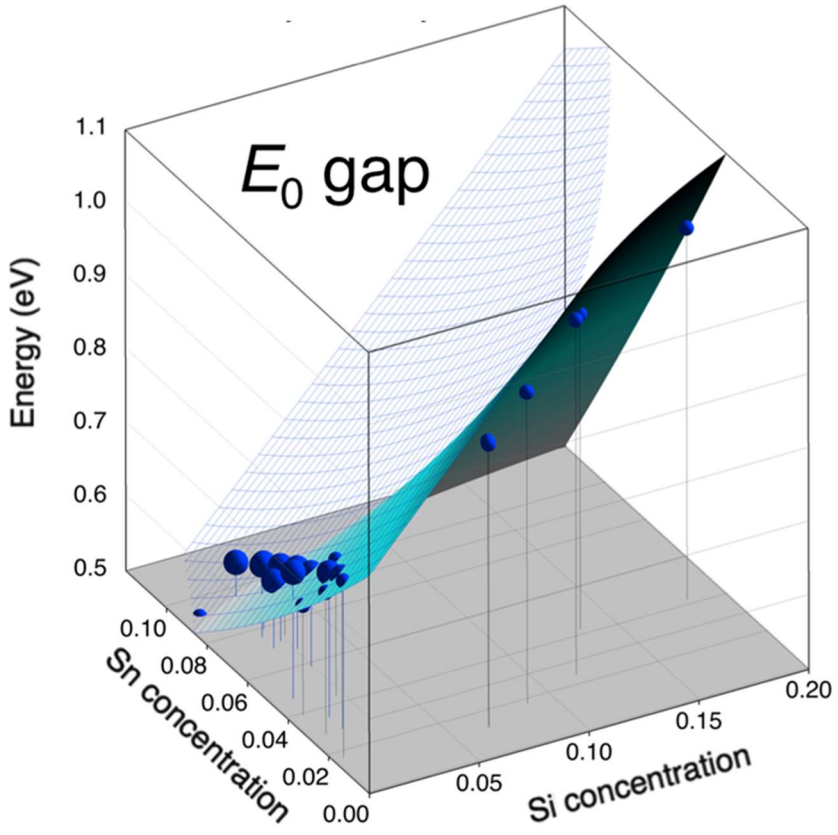

Figure 17: Experimental band gap energies (blue spheres) plotted along three dimensions, Si vs. Sn concentration vs. energy. The light blue surface is a fit of the spheres using Equation 2. The blue grid is a plot where $b^{SiSn} = 0$ eV.

a very wide range of compositions available to produce a direct gap material from $Ge_{1-x-y}Si_xSn_y$, including those which lattice match Ge. This is extremely beneficial from a photonics perspective where a wide range of light absorption is possible from a single alloy system with low defectivity, which is essential for reducing radiative recombination in devices.

2.5 Summary

Development of CVD reactions that have enabled the fabrication of thick, highly concentrated $Ge_{1-y}Sn_y$ layers (y = 0.12 - 0.16) possessing tunable band gaps within the desirable long wave mid-IR range have been described. These materials are grown on Ge buffered Si wafers and in turn used to fabricate working *p-i-n* diodes. For devices with 12 - 14 % Sn contents, the active layers are grown directly on the Ge buffer and capped with a $Ge_{1-z}Sn_z$ top electrode thus producing a partially lattice matched stack of the form *n*-Ge/*i*-$Ge_{1-y}Sn_y$/*p*-$Ge_{1-z}Sn_z$ containing a single defected bottom interface. For 15 - 16 % Sn devices an intermediate $Ge_{1-x}Sn_x$ layer is needed to overcome the ever increasing strain mismatch of the active material and the Ge buffer. This creates lattice-matched hetero-structures of the form *n*-$Ge_{1-x}Sn_x$/*i*-$Ge_{1-y}Sn_y$/*p*-$Ge_{1-z}Sn_z$ featuring slightly compressive and fully coherent active materials that are devoid of extended defects induced by strain relaxation. In spite of the excellent crystal quality observed by XTEM, the dark currents of the latter devices are two orders of magnitude higher than the former. This behavior is explained by a band-to-band-tunneling mechanism that is further enhanced when the *n*-

type bottom layer is a direct gap material as in the case of the *n*-$Ge_{1-x}Sn_x$/*i*-$Ge_{1-y}Sn_y$/*p*-$Ge_{1-z}Sn_z$ prototype. In light of this observation, it is proposed that various device alternatives that promote the formation of Type-I designs should be used for applications in future generation lasers and LEDs operating in the mid-IR.

Experiments performed in pursuit of high Sn content $Ge_{1-x-y}Si_xSn_y$ materials have been successful, and several samples in the high Sn regime have been produced which incorporate small quantities of Si. PL studies performed on these films have demonstrated intense single peak features indicating direct gap behavior is possible even at increased Si content. PL and EL studies have provided insight into the bowing parameter of Si-Sn. The findings indicate that there is a large bowing associated with Si-Sn on the order of ~25 eV, this agrees well with observations in previous studies. This large bowing means that the additional compositional degree of freedom allowed by $Ge_{1-x-y}Si_xSn_y$ may allow a shift toward even lower energies at high Si and Sn compositions. This is especially advantageous in the pursuit of mid-IR active materials. This class of materials is extremely promising, and may be the ideal candidate for future Group IV mid-IR devices combining both the thermal stability of Si with the band gap tunability of $Ge_{1-y}Sn_y$.

Chapter 3

MOLECULAR EPITAXY OF PSEUDOMORPHIC $Ge_{1-Y}Sn_Y$ (Y = 0.06-0.17) MATERIALS AND DEVICES ON Si/Ge AT ULTRA-LOW TEMPERATURES VIA REACTIONS OF Ge_4H_{10} AND SnD_4

Portions of this chapter were reprinted from Wallace, P.M.; Xu, C.; Senaratne, C.L.; Sims, P.; Kouvetakis, J.; Menéndez, J. *Semicond. Sci. Tech.* **2017**, *32*, 025093 with permission of IOP Publishing.

Synopsis

In this chapter, a low-pressure MBE-like deposition technique for the growth of $Ge_{1-y}Sn_y$ is described. Using this method, pseudomorphic $Ge_{1-y}Sn_y$ alloys with compositions as high as y = 0.17 were grown directly onto Ge buffered Si(100) wafers. The thicknesses of the resultant $Ge_{1-y}Sn_y$ films were far greater than those predicted by thermodynamic considerations. Additionally, fully pseudomorphic *p-n* junction diodes were produced in order to determine the feasibility of this growth method in device fabrication. Photoluminescence studies performed on the samples indicated that the pseudomorphic $Ge_{1-y}Sn_y$ alloys have a decreased light emission relative to relaxed samples produced through standard CVD methods.

3.1 Introduction

In addition to the optoelectronic applications afforded by $Ge_{1-y}Sn_y$, the lower and more direct bandgap afforded by high Sn alloying also increases tunneling probability, making $Ge_{1-y}Sn_y$ a potential candidate for fabrication of tunnel field effect transistors (TFETs).[77-80] Finally, $Ge_{1-y}Sn_y$ has higher carrier mobility than Ge, making this alloy suitable for use as a channel material in Ge-based metal-oxide-semiconductor field effect transistors (MOSFETs).[81-85]

The optical and electronic properties of $Ge_{1-y}Sn_y$ alloys grown on Si and Ge platforms are known to exhibit a strong dependence on the strain state of the material. A high degree of strain relaxation generates greater band gap directness, and is therefore preferred when the alloy is used in optical applications.[49] The synthesis of relaxed $Ge_{1-y}Sn_y$ alloys is typically accomplished by chemical vapor deposition (CVD) using reactions of higher order Ge hydrides as the source of Ge. Two different approaches have proven to be most successful for syntheses of device quality samples. The first utilized ultra-high vacuum chemical vapor deposition (UHV-CVD) of SnD_4 and Ge_2H_6 to fabricate prototype models of detectors and electrically injected LEDs.[86,87] This paved the way for the development of first generation devices with properties extending the optoelectronic capabilities of Ge. Subsequently, Ge_3H_8 was employed in place of Ge_2H_6 due to its better chemical compatibility with SnD_4, leading to the formation of $Ge_{1-y}Sn_y$ samples that enabled a systematic development of optical devices spanning a wide composition range from the short-wave IR to the mid-wave IR up to 3.0 μm and beyond.[37,88] Another reduced pressure CVD approach was also developed using Ge_2H_6

and the more conventional $SnCl_4$ source suitable for industrial scale production. This methodology provided access to next generation materials and devices culminating with the first demonstration of lasing from this class of Group IV alloys.[12,89]

While the above methods produced mostly relaxed samples for applications in photonics, the synthesis of compressively strained counterparts is also desirable for high frequency electronics. The latter samples exhibit higher hole mobility than pure Ge, and have therefore been used as a device channel material in MOSFETs.[90,91] Thus far, the preferred method for growing compressively strained samples has been solid source molecular beam epitaxy (MBE) on Ge wafers and on Ge-buffered Si substrates. The ultra-low temperatures afforded by this technique ensures pseudomorphic growth of the epilayers on the underlying Ge platform, leading to lattice-coherent films with thicknesses comparable to the critical values.[82-98] Such films have been used to study the fundamental optical properties of strained alloys,[99,100] to investigate their relaxation behavior,[89,96-98] and to fabricate LEDs and photodetectors as a function of composition.[54,101,102]

Notwithstanding the successful demonstration of strained samples by MBE, it is desirable for practical applications to develop CVD methods. This would facilitate industrial scale production and large area selective growth of compressive channels and stressors as required for low cost high performance technologies. The work described in this chapter addresses this potential innovation and introduces a CVD technique capable of producing fully strained films on Ge/Si substrates over a wide composition ranging from 6-17% Sn. This strategy utilizes depositions of SnD_4 with the highly reactive

Ge_4H_{10} hydride compound in place of Ge_3H_8 and Ge_2H_6. The larger mass of the molecule reduces the surface mobility and increases the sticking coefficient, promoting unprecedented low growth temperatures down to at least 150 °C. This leads to the formation of crystalline layers with compressively strained states via complete H_2 elimination at gas pressures in the range of 10^{-4} Torr. Therefore, this work expands the reach of CVD of high order Ge hydrides to MBE-like fabrication regimes where pseudomorphic growth is attained and strain relaxation is prevented. The additional flexibility for strain engineering afforded by this method may be particularly valuable in an industrial setting where CVD is preferred over MBE for epitaxial crystal assembly. In addition, this method may be useful for fundamental research involving integration of multilayer $Ge_{1-y}Sn_y$ heterostructures in which relaxation between device components must be avoided. Examples include multi-quantum-well diodes.[102]

The depositions were conducted on Ge-buffered Si wafers using a gas source molecular epitaxy (GSME) reactor described in previous work.[103] The resultant $Ge_{1-y}Sn_y$ films are fully pseudomorphic to the Ge buffer layers, despite having thicknesses far above the critical limit for strain relaxation predicted by the Matthews-Blakeslee model.[89,96,104] The compressive strains are as high as -2.2% for a 17% Sn epilayer, and the thicknesses range from at least 400 nm to 40 nm depending on composition. The substrate temperatures are in the 150 – 200 °C range, higher than those reported for MBE of $Ge_{1-y}Sn_y$ alloys with similar compositions (100 – 150 °C).[92,96] Despite this higher temperature, the thickness of the fully strained films is somewhat larger than MBE counterparts with no indication of surface roughening, in the form of cross hatch patterns,

or epitaxial breakdown in the as grown films. The possible reasons for such differences between the two methods will be discussed below, together with the advantages offered by the Ge_4H_{10} method in synthesizing fully strained films at MBE like conditions. In addition, it is demonstrated that device quality alloys can be obtained using this novel Ge_4H_{10}/SnD_4 method. Lastly it was found that strain relaxation eventually occurs in these materials as the thickness is further increased, leading to the formation of bulk-like films that exhibit superior optical performance compared with CVD-grown analogues, with no sign of phase segregation and surface degradation. This indicates that the ultraclean conditions afforded by the MBE-like procedure produces better quality materials. The added benefit of this approach will be discussed relative to materials produced by conventional methods in the context of device applications in the near-IR.

3.2 Experimental

The initial step of the deposition process is the production of the Ge buffer layers on commercially available 4-inch Si(100) substrates. These were first cleaned with a modified RCA process, and then dipped in 5% HF/methanol solution to etch the ambient oxide and hydrogen-passivate the surface prior to growth. These substrates were subsequently loaded into the deposition chamber at a base pressure of 1×10^{-10} Torr, which is obtained via a combination of turbomolecular and cryogenic pumps. The wafers are outgassed on the sample stage under these UHV conditions up to a temperature of 450 °C and thereafter flashed at 800 °C to remove residual contaminants and generate a

deposition ready surface. The formation of the Ge buffer layers was conducted at temperatures around 350 °C using a gas mixture of Ge_4H_{10} and H_2, as described in detail elsewhere.[103] The resultant buffers are typically ~800 nm thick and exhibit atomically flat surfaces (atomic force microscopy root mean square roughness of ~0.5 nm). After deposition, the crystallinity of the materials is optimized by *in situ* annealing at 650 °C for 3 min to generate a suitable template for subsequent growth of the $Ge_{1-y}Sn_y$ epilayers.[103]

The latter are deposited either *in situ* or *ex situ* (by taking the wafer out and reinserting upon cleaning) using stock mixtures of gaseous Ge_4H_{10} and SnD_4 diluted with H_2. The precursors were mixed in a 3.0 L container ensuring a uniform precursor ratio in the gas supply fed into the chamber during deposition. The amount of Ge_4H_{10} in each container was kept constant at 1.0 Torr, while that of SnD_4 was varied from 3-10 Torr to obtain the desired composition in the range of y = 0.06-0.17, indicating that an excess of

Table 2: Properties of representative pseudomorphic $Ge_{1-y}Sn_y$ films in the composition range y = 0.06 - 0.17 grown using Ge_4H_{10}. The average growth rate obtained from the thickness and overall deposition time is reported here.

Sample	Relaxed lattice parameter (Å)	Sn content (%)	Thickness (nm)	Rate (nm/min)	Growth temperature (°C)	Strain (%)
A	5.7082	6.4	370	2.60	200	-0.82
B	5.7278	8.1	300	1.84	190	-1.01
C	5.7385	9.8	80	0.80	180	-1.22
D	5.7744	13.6	58	0.40	160	-1.84
E	5.7849	15.2	43	0.32	155	-2.01
F	5.7980	17.1	39	0.30	150	-2.22

SnD_4 is required under these conditions**.** This is likely due to the lower sticking coefficient of the compound on the growth surface, reducing its efficiency in spite of the expected facile reactivity associated with the relatively weak and thermally unstable Sn-D bonds. A similar behavior has been observed when the analogous SbH_3 (SbD_3) molecule is used to grow GaSb at low temperatures via reactions with Ga metalorganics,[105] indicating that the high reactivity does not necessarily translate into efficient Sb incorporation. Thus, additional activation was employed using cracking techniques, suggesting that a similar approach might apply to SnD_4 to increase its reaction efficiency. It was found that the excess SnD_4 in these experiments is pumped away and does not decompose into elemental Sn that can potentially contaminate the samples.

The growth temperatures used for the depositions were progressively reduced with increasing Sn content of the target alloy layers in order to prevent decomposition of the metastable material. For $y = 0.06$, a relatively high temperature of 200 °C was used. For $y = 0.17$ the temperature was reduced to 150 °C, and intermediate compositions were produced at temperatures between the two extremes. The total pressure of the gaseous reactants within the chamber during deposition was kept constant at 1×10^{-4} Torr for samples in the $y = 0.06$-0.11 range. At concentrations $y > 0.11$, the pressure was increased to 2.5×10^{-4} Torr in an effort to enhance the lower growth rates resulting from the reduced temperatures required to produce single-phase alloys.

3.3 Results and Discussion

3.3.1 Composition and Structural Analysis

A series of representative samples produced using the above conditions and their corresponding growth parameters and properties are listed in Table 2. Rutherford backscattering spectrometry (RBS) was used to measure the bulk compositions and thickness of the samples and the results are listed in columns 3 and 4, respectively (the concentration error is ~ 0.1%). Typical spectra are shown in Figure 19. Note that the thickness decreases with decreasing growth temperature and increasing composition as expected, limiting the overall film thickness that can be achieved under these conditions. Nevertheless, these thicknesses are slightly higher by ~10-20% compared to those reported for fully strained samples obtained via MBE with similar compositions.[96,97] High-resolution X-ray diffraction (HR-XRD) was used to measure the in-plane and vertical lattice parameters of all samples. Representative spectra are shown in Figure 18 which contains the (004) peaks for films with Sn compositions 10%, 13% and 17% designated as C, D and F in the table, respectively. A systematic increase of the out-of-plane lattice parameter (c) is observed with increasing Sn content, from 5.7910 Å for the 10% sample Sn up to 5.8961 Å for the 17% Sn sample causing the shift of the peak position to lower Bragg angles in the main panel of the figure. The inset shows a representative (224) reciprocal space map (RSM) from the 13% sample (lower peak) indicating that the in-plane lattice parameter (a) is identical to that of the Ge buffer

(upper peak) as evidenced by the vertical alignment of the diffraction peaks along the pseudomorphic direction. The measured value of (a) in both cases is 5.664 Å which is slightly larger than the ~5.657 Å of bulk Ge. This is due to the tensile strain of the buffers resulting from the thermal expansion mismatch between the Si and Ge materials. The above data was used to calculate the relaxed lattice constants of the samples using standard elasticity theory and the results are listed in column 2 of Table 2. The trend reveals a monotonic increase with Sn content from 5.7082 Å for 6% Sn to 5.7980 Å for 17% Sn. These values were then used to calculate the compressive strains, which increase from -0.82% for the 6% to -2.22% for the 17% Sn, in agreement with the extreme tetragonal distortion of these films (see column 6).

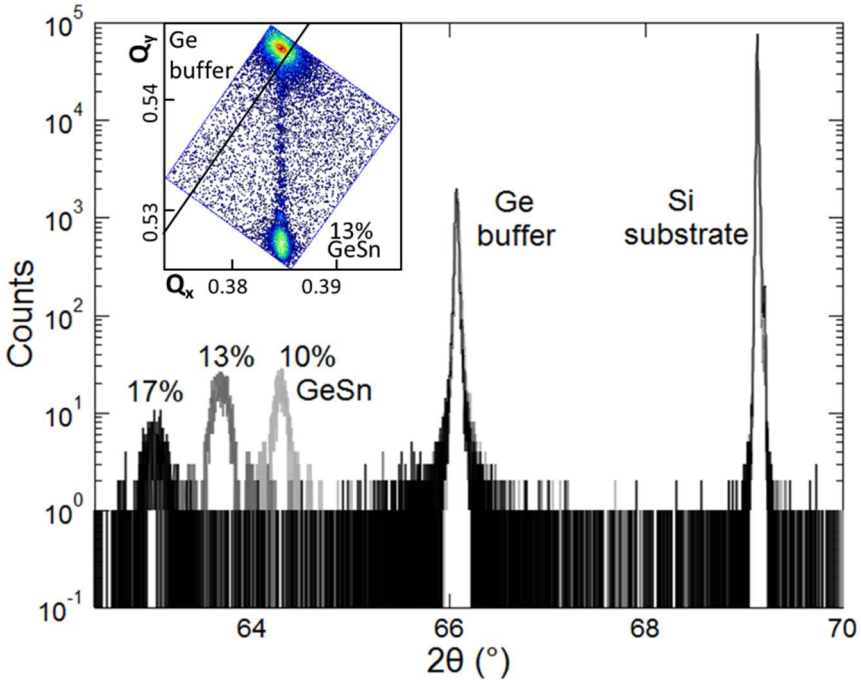

Figure 18: Series of 004 θ/2θ scans from $Ge_{1-y}Sn_y$ alloy films in the y = 0.10-0.17 composition range. The peak position shifts to smaller angles with increasing Sn content, illustrating the expansion of the lattice. The inset is a representative 224 RSM used to calculate the lattice parameters and strain states of the alloy layers.

The RBS spectra in Figure 19 correspond to $Ge_{0.83}Sn_{0.17}$ (main panel) and $Ge_{0.936}Sn_{0.064}$ (inset) films. They were obtained in random and aligned (channeling) geometries. The channeled signal of the epilayer for the latter film has similar intensity profiles to that of the buffer indicating comparable crystallinity between the two materials. The film in this case remains fully pseudomorphic in spite of the 370 nm thickness of the epilayer approaching bulk-like values. Finally, note that the RBS compositions are in close agreement with the XRD estimates. The latter were determined using the relaxed lattice parameters in conjunction with compositional dependence of the lattice constant for these materials. This indicates that the Sn atoms occupy substitutional positions within the Ge lattice, a conclusion that is also supported by RBS channeling

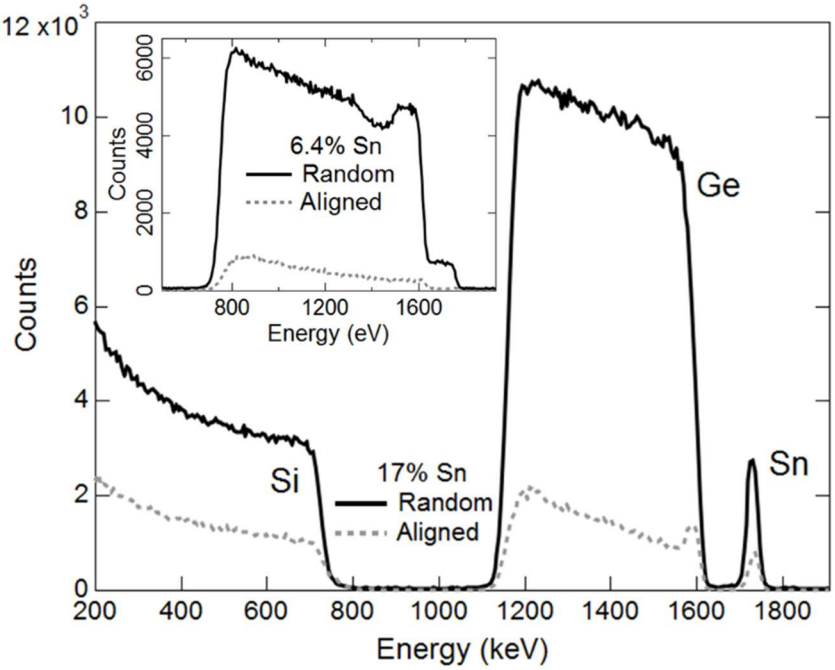

Figure 19: Comparison random (solid line) and channeled (dashed line) spectra from a 40 nm thick $Ge_{0.83}Sn_{0.17}$ film (sample F in Table 2). The inset shows a similar comparison for a 380 nm thick $Ge_{0.94}Sn_{0.06}$ alloy.

experiments (the ratio of the channeled over the aligned spectra intensities is the same for the two atoms at 5.9 %).

The film morphology was examined with optical imaging, atomic force microcopy (AFM) and cross sectional transmission electron microscopy (XTEM), all indicating planar and featureless samples. In particular, AFM showed that the surfaces were smooth and flat, with root mean square (RMS) roughness spanning from 0.8 nm to 1.4 nm across the composition range of 9% to 17% Sn. No evidence of cross hatch patterns or undulations were observed in all strained films, indicating low density of relaxation induced defects. As mentioned earlier, this behavior is a result of the ultra-low growth temperatures afforded by this method. Under these conditions, the relaxation process is limited by kinetic considerations, as will be discussed in greater detail below. Therefore, the film thicknesses given in Table 2 far exceed the equilibrium critical values for strain relaxation at a given composition. Figure 20 shows XTEM images for a 40 nm thick layer of a $Ge_{0.83}Sn_{0.17}$ alloy, the highest Sn content material produced in this study. The data were acquired in scanning mode (XSTEM) using a JEOL ARM200F microscope. Panel (a) is a z-contrast image of the full layer in (110) projection including the interface marked by arrow. The material is a fully coherent single-crystal devoid of dislocations as evidenced by the uniform contrast throughout the image. The high-magnification image in the inset illustrates the dimers or “dumbbells” demonstrating an average diamond cubic lattice with no evidence of crystallographic disorder or Sn clustering. These observations further validate the phase purity of the highly concentrated alloy at the atomic scale. Panel (b) shows a lower magnification diffraction-contrast

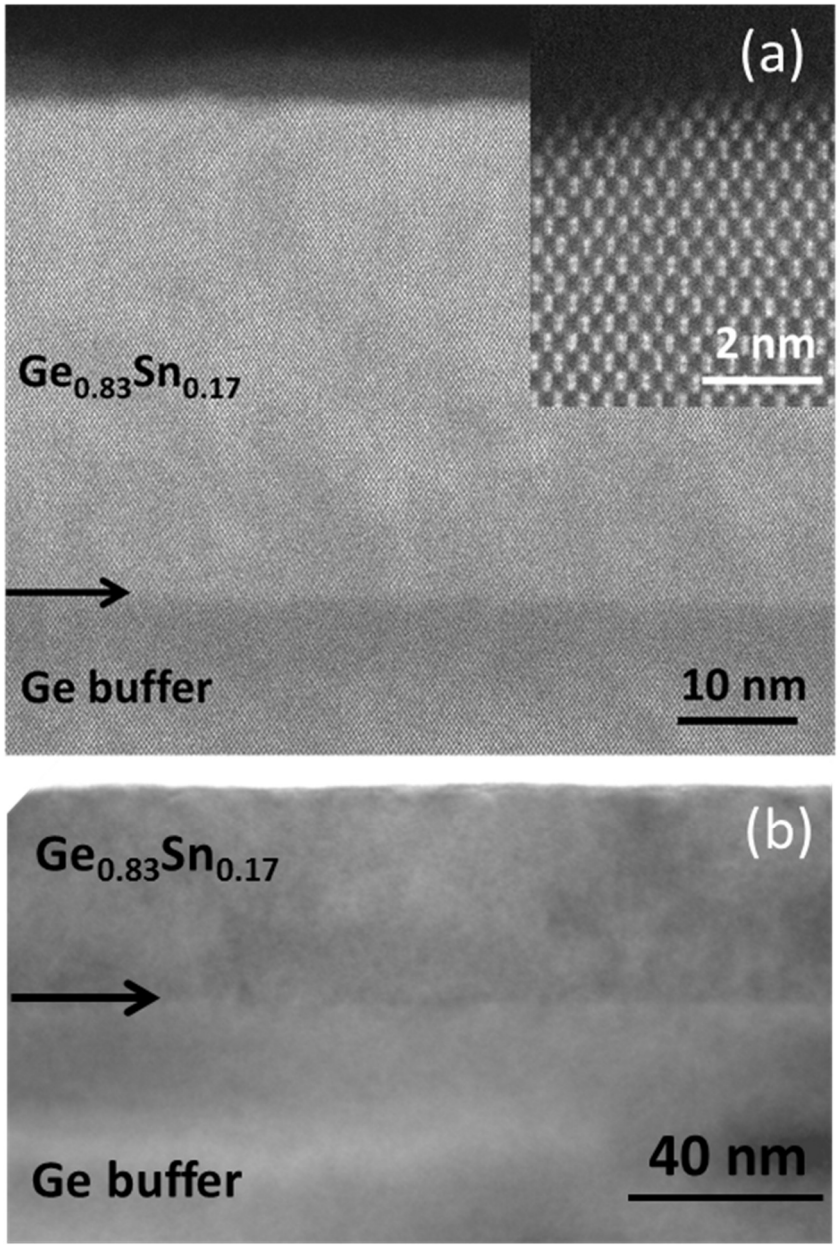

Figure 20: X(S)TEM images of $Ge_{0.83}Sn_{0.17}$ alloy on Ge buffered Si. Panel (a) shows a Z-contrast aberration corrected image of the entire layer and a higher magnification analogue in the inset. Panel (b) shows a diffraction contrast micrograph of the same material illustrating defect free microstructure. The latter was acquired using a FEI Titan 80-300 microscope.

image of the same material. The surface is flat and the interface is uniform and defect-free which is consistent with the lack of cross hatch patterns in the AFM images.

3.3.2 Doping and Device Fabrication

It was found that the strained alloys could be readily doped *n*-type *in situ* by including the $P(GeH_3)_3$ single source in the precursor mixture. Infrared ellipsometry measurements indicated that doping levels up to $4\times10^{19}/cm^3$ were achieved at 160 °C, demonstrating that the dopant molecules readily incorporate into the strained films despite the low growth temperatures without the need of thermal activation, as observed earlier for relaxed films. Secondary ion mass spectrometry (SIMS) profiles showed that the dopant atoms are uniformly distributed within the layers with no evidence of accumulation at the interface and top surface. A representative spectrum is shown in Figure 21 illustrating the elemental profiles of P, Ge and Sn for a sample with 11% Sn content.

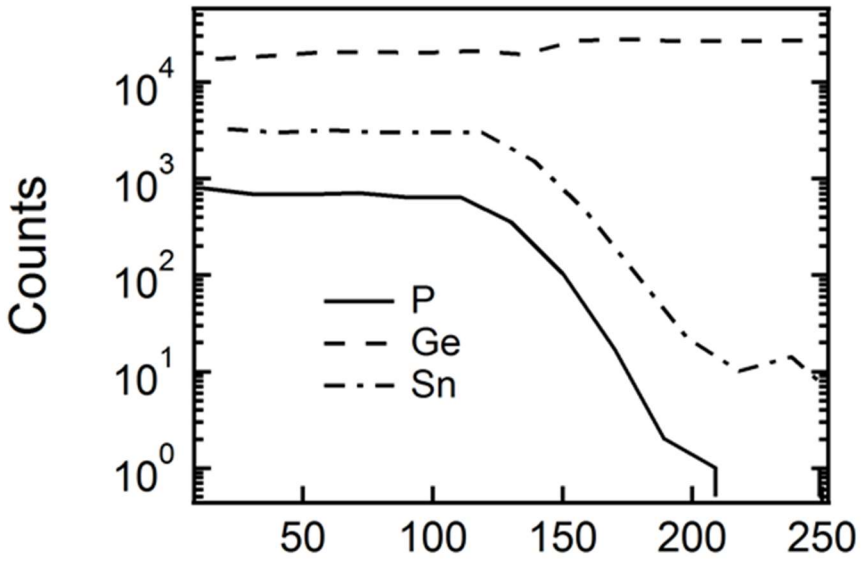

Figure 21: Representative SIMS spectrum for a sample with 11% Sn content doped by P using the $P(GeH_3)_3$ compound.

Recent MBE studies have utilized post growth implantation methods[104-108] to *n*-type dope fully strained $Ge_{1-y}Sn_y$ followed by annealing to activate the dopants. This process is not ideal since it can potentially lead to phase segregation in metastable high Sn content alloys needed to achieve direct gap conditions. In a more recent study, *in situ* doping was successfully applied using solid antimony to activate fully strained samples with 6% Sn content.[105] In this study, the ability to dope higher concertation materials ($y \geq$ 9% Sn) using *in situ* growth and the control of the atom donor distribution afforded by this chemical method provides further validation of the practical relevance of the new CVD route. To demonstrate the potential device applications of doped, fully strained films, a representative y = 0.09 sample activated with $n = 1.7\times10^{19}$ atoms/cm^3 was chosen for the fabrication of a prototype *p*-*n* diode (the activated dopants have been measured by infrared spectroscopic ellipsometry). The $Ge_{0.91}Sn_{0.09}$ *n*-layer was grown at ~190 ºC on a 900 nm thick Ge buffer using appropriate concentrations of Ge_4H_{10}, SnD_4 and $P(GeH_3)_3$ in the reaction mixture. The final film thickness was ~300 nm which far exceeds the equilibrium limit of 10 nm with no evidence of strain relaxation in the XRD and AFM measurements. Figure 22(a) depicts the (224) RSM and (004) θ/2θ scan of the device sample. The $Ge_{0.91}Sn_{0.09}$ layer peak is sharp and symmetric, indicating a single-phase material throughout the layer. The full width at half maximum (FWHM) of the rocking curve (not shown) is 0.050°, a value comparable to that of the Ge buffer (0.047°). The above observation leads to the conclusion that the crystallinity of the alloy is comparable to that of the buffer. The *p*-type layer of the *p*-*n* diode was deposited in a separate UHV-CVD reactor that is specially calibrated for boron doping using diborane. In a typical

experiment the 4-inch wafer was characterized for quality control and then cleaved into

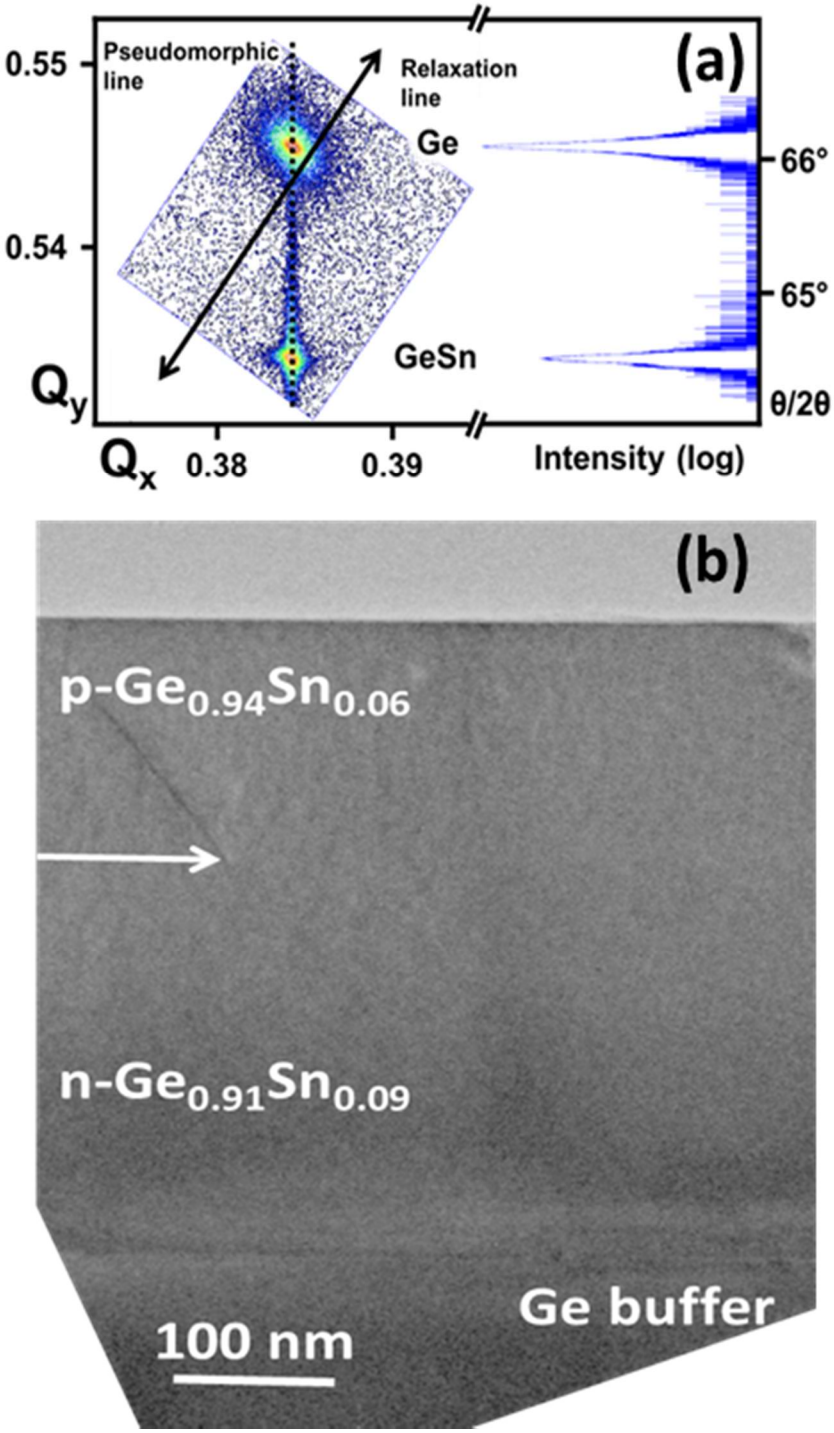

Figure 22: (a) (224) RSM and (004) θ/2θ scan of *n*-type doped $Ge_{0.91}Sn_{0.09}$ epilayer. (b) XTEM image of the *n*-$Ge_{0.91}Sn_{0.09}$/*p*-$Ge_{0.94}Sn_{0.06}$ diode incorporating the active layer described in panel (a). The interface between the *n*- and *p*-layers is marked by the arrow. The Ge buffer layer is also visible.

45 mm × 45 mm quadrants which were then used for the fabrication of the device stacks. Each quadrant was cleaned using 5% aqueous HF and loaded into the reactor under a flow of background hydrogen at 320 °C. Immediately thereafter, a mixture of Ge_2H_6, SnD_4 and B_2H_6 were introduced into the reaction zone to deposit the *p*-type top contact layer. The latter exhibited a composition of $Ge_{0.94}Sn_{0.06}$ and contained a doping level of 3×10^{19} /cm^3. A thickness of 140 nm ensured full commensuration with the underlying material, thereby yielding a defect free *p-n* interface in the depletion region. Figure 22(b) displays a representative XTEM image of the entire diode stack grown on Ge showing that the *n*-layer is defect-free within the field of view as expected due to the pseudomorphic nature of the material. A dislocation is visible at the interface with the *p*-type top layer marked by the white arrow in the image.

Fabrication of the prototype *p-n* junction was conducted using previously developed techniques as described in Ref. 110. Briefly, the fully characterized $Ge_{1-y}Sn_y$ device stack was coated with a protective SiO_2 layer and then circular mesas with diameters ranging from 50 μm to 300 μm were patterned using standard photolithography techniques. The material was etched 200 nm down into the *n*-$Ge_{1-y}Sn_y$ layer using a BCl_3 plasma source. A passivating SiO_2 layer was used to minimize light reflectance and 200 nm thick Cr/Au contacts were defined via thermal evaporation. The current voltage (I-V) characteristics of the fabricated devices were measured from -1.0 V to 1.0 V and the results are plotted in Figure 23. Here the differential conductance (d*I*/d*V*) vs. applied bias plots show a minimum at less than 0.2 V forward bias. This is due to quenching of the band-to-band tunnel current on account of the heavy doping density present in the *p-n*

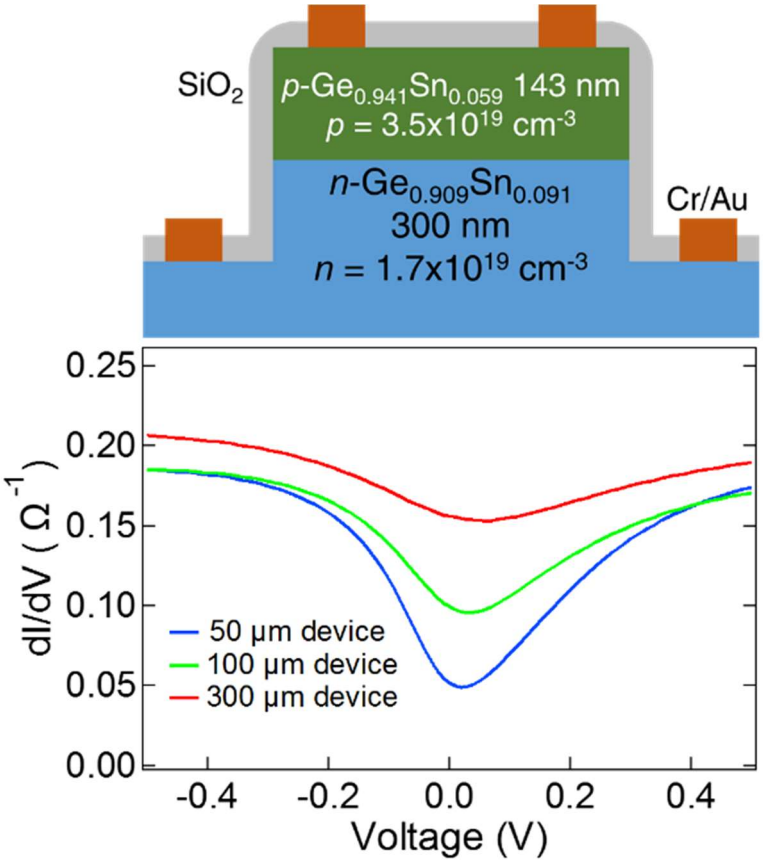

Figure 23: (top) Schematic of the *n*-$Ge_{0.91}Sn_{0.09}$/*p*-$Ge_{0.94}Sn_{0.06}$ heterostructure diode showing the various device elements. (bottom) Differential conductance vs. voltage obtained from representative device mesas of the above diode.

junction, and this is consistent with previously fabricated $Ge_{1-y}Sn_y$ *p-n* diodes reported by Gallagher *et al*.[110] The plots also show that the smaller devices have a lower conductance minimum relative to the larger counterparts. The fabrication and testing of degenerate *p-n* junctions demonstrates that functional devices can be developed from fully strained $Ge_{1-y}Sn_y$ materials with band gaps approaching direct conditions. This is made possible by the ability to activate those materials *in situ* without relaxing the compressive strains, a testament to the ultra-low temperature approach developed in this study using highly reactive chemicals.

3.3.3 Strain Relaxed $Ge_{1-y}Sn_y$ /Ge/Si(100) Films via Ge_4H_{10} and SnD_4

Reports of $Ge_{1-y}Sn_y$ epilayers deposited using MBE at low temperatures (100-160 ^oC) indicate that beyond a certain critical thickness, surface roughening and subsequent epitaxial breakdown take place.[92,97,111] For samples with 17% Sn, Oehme *et al.* report a critical thickness for epitaxial breakdown of 5 nm grown at 160 °C,[92] and a similar value of 10 nm was reported by Gurdal *et al.* for layers deposited at 100 °C.[97] On the other hand Wang *et al*. reported a higher critical thickness of 30 nm for samples deposited at 100-150 °C.[96] In these experiments, a comparable 40 nm thickness was obtained for the same Sn concentration, despite the higher nominal growth temperature employed, indicating that these materials can be grown thicker than 30 nm with no sign of epitaxial break down. A similar trend is observed in these samples with y < 17% Sn which also show thicknesses somewhat above the critical limits determined by Wang *et al*. Therefore, it appears that the tetragermane method can be used to produce fully strained, high crystal quality films beyond the thicknesses possible with MBE techniques.

Figure 24 summarizes the strain relaxation findings in these samples and compares them with the MBE studies by Bhargava *et al*. (Ref. 95) and Wang *et al.* (Ref. 96) as well as the CVD experiments by Gencarelli *et al*. (Ref. 112). In all cases, solid symbols are used to indicate fully strained samples. Empty symbols correspond to partially or totally relaxed samples. The results are comparable to the findings by Wang *et al.* As indicated above, the critical thicknesses are somewhat higher than those reported

in Ref 96. Part of the discrepancy could be due to the fact that the Ge buffer layers exhibit slight tensile strains between 0.1 - 0.13%. These increase the in-plane lattice parameter of the Ge buffer relative to the bulk, so that for a given Sn composition the epilayers would display slightly lower compressive strains than they would if they were grown on bulk wafers, as was the case in Ref. 96. On the other hand, these samples were grown at higher temperatures, and therefore it is quite remarkable that they show evidence for critical thicknesses exceeding those reported in Ref. 96. The shaded region in Figure 24 approximately indicates the range of thicknesses corresponding to fully strained samples according to the data and Ref. 96. Note that this range exceeds the Matthews-Blakeslee critical thickness by at least one order of magnitude. In order to gain insight into the critical thickness limit of such $Ge_{1-y}Sn_y$ films on Ge/Si substrates, a series of depositions were conducted in which the epilayers with 6.5% and 7.8% Sn were grown for longer time periods until strain relaxation occurred. The resultant films were grown on 800 nm thick Ge buffers and were found to follow a similar relaxation mechanism to those produced via the conventional $Ge_2H_6/SnCl_4$ or Ge_3H_8/SnD_4 CVD methods on similar platforms. The layers mostly relaxed *in situ* by ~70 % during growth via generation of misfit dislocation (as evidenced by the cross hatch patterns) yielding single phase materials with planar surfaces and bulk-like thicknesses approaching 400 nm and above.

In Ref. 49 the strain measurements were explained from all references available at the time using a kinetic relaxation model proposed by Hull *et al.*[113] and successfully applied by Houghton *et al*. to strain relaxation in $Si_{1-x}Ge_x/Si$. (Ref. 114). This model

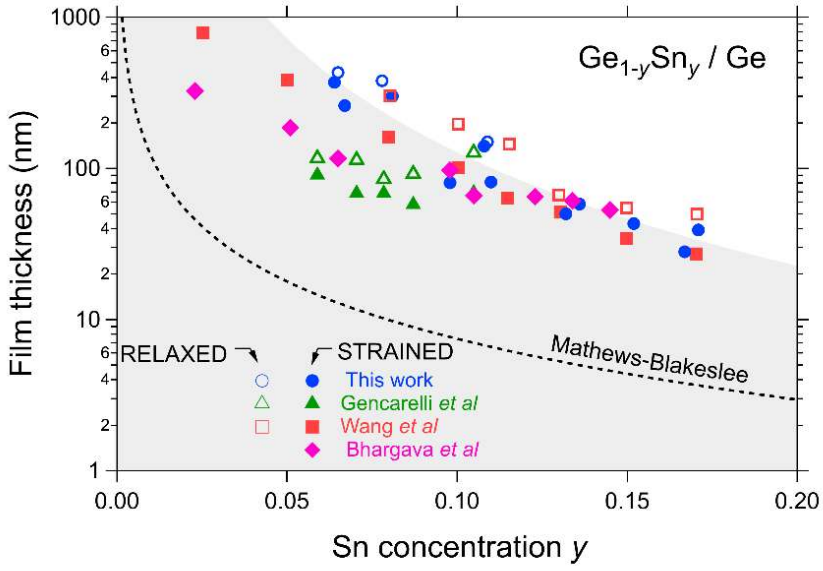

Figure 24: Thickness vs. composition for fully strained and partially relaxed $Ge_{1-y}Sn_y$ alloys on Ge for samples produced in this work (circles) compared with MBE grown samples reported in Refs.112 (triangles), 96 (squares), and 95 (diamonds). The dashed line is the equilibrium critical thickness for strain relaxation calculated from the Matthews-Blakeslee model, and the gray area represents the critical thickness predicted in Ref. 92 based on the People-Bean model.

contains three material parameters that characterize the dislocation nucleation rate and three additional parameters that characterize the dislocation velocity. These parameters were determined by Houghton via systematic studies of Si-rich $Si_{1-x}Ge_x$ alloys. Subsequent work by Yonenaga *et al.*[115] yielded new parameters for the dislocation velocity in pure Ge, which were used for $Ge_{1-y}Sn_y$ instead of those originally proposed by Houghton. The only truly adjustable parameter of the relaxation model is the so-called density of incipient dislocation nuclei n_0, which characterizes the defects at the interface that seed the generation of dislocations. Using the value of n_0 fit to the data in Ref. 49, combined with the same material parameters, one may not explain the new data. For example, one would predict all but one of the samples reported here to be fully strained.

It is found that one can restore the agreement with experiment by reducing the activation energy Q_n for dislocation nucleation, a change that makes physical sense because the Houghton value which was used in Ref. 49 corresponds to Si-rich alloys. However, there is no choice of Q_n with which one may explain all the data in Figure 24, including the results from Wang *et al*. (Ref. 96), using a single value of n_0. In particular, the model requires drastically (and probably unphysically) higher values of n_0 for the data from Ref. 96 to accommodate the fact that the critical thicknesses in their work are only slightly lower than these, but their samples were grown at significantly lower temperatures. These results are reminiscent of previous findings in the $Si_{1-x}Ge_x$ system,[116] for which it was also shown that the strain relaxation observed in films grown at very low temperatures requires much higher values of n_0 than found in modeling strain relaxation at higher growth temperatures. These results suggest that the Hull-Houghton kinetic strain relaxation model may ignore strain relaxation mechanisms that become dominant at low temperatures.

It is interesting to note that in models that simulate kinetic barriers to strain relaxation there is no well-defined critical thickness beyond that obtained from the Matthews-Blakeslee model, also shown in Figure 24. Instead, the metastable critical thickness is conventionally defined as the largest thickness for which strain relaxation can be observed experimentally. In Refs. 49 and 114, this limit was arbitrarily defined as a relaxation strain of 10^{-5}. On the other hand, Wang *et al*. utilized the equilibrium model due to People and Bean,[117] which predicts a critical thickness consistent with the borderline between shaded and white areas in Figure 24. A possible way to distinguish

between the two types of models is to perform annealing experiments. If the critical thickness is a truly equilibrium quantity, it is expected to be robust against thermal excursions, whereas in kinetic-limit models the strain relaxation should accelerate upon annealing. Annealing experiments were carried out on the 13% Sn sample by placing it in a heated quartz tube under H_2 ambient. It was found that its lattice constants remain unchanged relative to as grown after annealing up to 350 °C. Increasing the temperature beyond this threshold up to 400 °C produced a decrease in substitutional Sn as measured by XRD. This is accompanied by the formation of large islands and clusters of Sn precipitates randomly distributed on the film surface. These features are presumably enriched in Sn, indicating phase separation due to Sn migration. Similar observations have been reported by other authors upon annealing of strained $Ge_{1-y}Sn_y$ films.[94,118] From these results, it can be concluded that phase separation is preferred over strain relaxation when pseudomorphic $Ge_{1-y}Sn_y$ films with high Sn contents are subjected to thermal treatments. This result lends support to the People-Bean theory invoked in Ref. 96. On the other hand, similar annealing experiments in $Si_{1-x}Ge_x$ alloys clearly indicate that the Matthews-Blakeslee expression, not the People-Bean prediction, gives the true equilibrium critical thickness.[119,120] The People-Bean expression has also been questioned based on theoretical considerations.[121,122] Therefore, it is believed that a satisfactory model for strain relaxation in $Ge_{1-y}Sn_y$ and SiGe films is still outstanding, particularly for growth at low temperatures.

For the partially relaxed 6.5% and 7.8% Sn films described above, it was found that the photoluminescence (PL) intensities are significantly enhanced relative to those of

CVD grown samples in prior work via the Ge_2H_6 / Ge_3H_8 approach (reported elsewhere). For example, the PL signal of a 400 nm $Ge_{0.922}Sn_{0.078}$ film was stronger than that of a 600 nm $Ge_{0.91}Sn_{0.09}$ analogue grown via Ge_3H_8 /SnD_4, even though the latter is closer to the onset of the direct gap transition. This indicates that the cleaner deposition environment afforded by the MBE-like growth methods reported here produces alloys with superior optical performance. Furthermore, it was found that the residual compressive strains in the as grown samples were low (~ -0.26%) indicating that near cubic crystals could be obtained. Representative PL spectra from these samples are depicted in Figure 25, for which the excitation was accomplished via a 980 nm laser and the emission signal was detected using a thermoelectrically cooled InGaAs detector with an extended cutoff at 2500 nm. As expected, the peak of the higher Sn alloy is redshifted (2240 nm) relative to

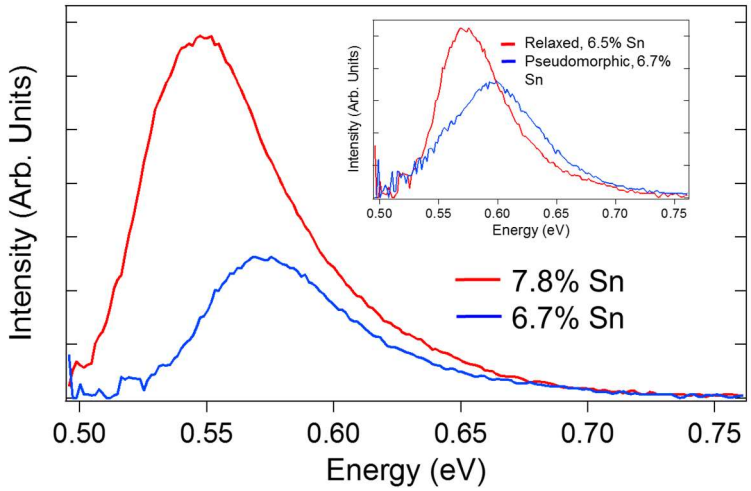

Figure 25: PL spectra obtained from relaxed $Ge_{0.922}Sn_{0.078}$ and $Ge_{0.933}Sn_{0.067}$ films, in which the former exhibits stronger PL intensity due to its more direct nature. The inset compares the PL intensity of the relaxed $Ge_{0.935}Sn_{0.065}$ film with that of a fully strained counterpart. Since the samples contain similar Sn contents, the shift in peak position is mainly attributed to the strain difference in the films.

the lower Sn alloy (2160 nm), and a sharp increase in PL intensity is seen as the compositions near the indirect-direct crossover.

To investigate the influence of the compressive strain on the emission properties the PL intensities and peak positions of a pseudomorphic 6.7 % Sn (260 nm) were compared to those of a mostly relaxed 6.5 % Sn counterpart (430 nm). The two spectra are given in the inset of Figure 25. The latter sample exhibits a stronger PL signal, as can be expected based on its larger thickness. Furthermore, the lower degree of compressive strain makes the materials more direct, further enhancing the PL intensity although experimental variation cannot be ruled out. The blue shift of the fully strained PL spectrum relative to the relaxed is also an effect of the large compressive strain, which increases the separation between the conduction and valence bands. It is also of interest to note that the PL from the strained sample is significantly broadened. This is attributed to the splitting of the light-hole and heavy-hole bands due to strain.

3.4 Summary

A new series of fully compressive $Ge_{1-y}Sn_y$ films have been grown on Ge-buffered Si via reactions of Ge_4H_{10} and SnD_4 at ultra-low temperatures, similar to those typically employed for conventional MBE. The growth conditions enabled fabrication of pseudomorphic layers with Sn contents up to 17% exhibiting large thickness far exceeding the thermodynamic critical limits with no sign of epitaxial breakdown or surface degradation. These thicknesses are generally larger than in previous MBE/CVD

studies reported in the literature making the materials potential candidates for applications in high mobility transistor technologies using industrial scale CVD techniques. The films were doped *in situ* with P atoms at concentrations approaching $4x10^{19}/cm^3$ and selected activated samples were used to produce *p-n* junction diodes which exhibited tunneling behavior indicating that the method produces device quality materials. Unlike films produced by MBE, these materials relax the misfit strain when increasing the thickness of the epilayer, producing strain-relaxed analogues with bulk like properties that include strong, tunable photoluminescence as a function of composition.

Chapter 4

FABRICATION OF Ge:Ga HYPER-DOPED MATERIALS AND DEVICES USING CMOS COMPATIBLE Ga AND Ge HYDRIDE CHEMISTRIES

Synopsis

Chapter 3 of this thesis describes a method for achieving highly strained $Ge_{1-y}Sn_y$ films for applications as MOSFET channel materials. Ultra-low resistivity materials are required in order to maximize carrier mobility for CMOS compatibility and this is typically achieved through high doping levels. Considerable progress has been made in the development of *n*-type doping techniques for $Ge_{1-y}Sn_y$. However, new routes toward *p*-type doping are crucial in order to achieve the low resistivities necessary for use as *p*-channel materials. This chapter describes a CVD route toward *in situ p*-type doping of Ge with Ga. This method utilizes $[D_2GaN(CH_3)_2]_2$ as a chemical source of Ga atoms that can be used in conjunction with Ge_4H_{10} to produce *p*-type Ge films with carrier concentrations up to $2.7x10^{20}$ cm^{-3}. The growth rates of these films were as high as 45 nm/min producing monocrystalline films over a micron thick. Photoluminescence studies revealed a strong emission peak at 0.79 eV corresponding to the E_0 transition, and a secondary peak at 0.85 eV due to a transition at the Γ-point without momentum conservation. Prototype *p-i-n* structure diodes were produced using this doping technique, and the resultant devices showed electroluminescence, and rectifying I-V characteristics on par with previously produced Ge devices

4.1 Introduction

Doping is an essential requirement for semiconductor device fabrication. In addition to traditional bulk doping,[123] numerous doping methods have been developed over the past decades, including implantation followed by annealing,[124,125] delta-doping,[126] and *in situ* doping during epitaxial growth.[127] Bulk doping methods can only be applied during crystal growth and are of limited value for applications in thin-film technologies. Implantation methods usually require the deposition of a SiO_2 capping layer, as well as high temperature treatments to activate the dopants and recrystallize the lattice. These may not be compatible with low temperature complementary metal-oxide-semiconductor (CMOS) processing, and make it very difficult to control doping level and junction depth independently.

In situ doping during film growth is a simple alternative that allows for high dopant levels with activation ratios (defined as the ratio of the carrier density over the chemical concentration of dopant atoms) approaching unity. Furthermore, by eliminating the need for recrystallization post-growth annealings, this approach makes it possible achieve box-like dopant profiles. *In situ* doping can be accomplished via Chemical Vapor Deposition (CVD) or Molecular Beam Epitaxy (MBE) methods. CVD is generally considered to be the more practical approach. CVD *n*-type doping of Ge is typically conducted using commercial PH_3[128] and AsH_3[129] sources. These require high processing temperatures to reach optimal incorporation and full activation, making them less attractive for certain applications. Recently, the focus has been shifting toward

developing ultra-low temperature (200-350 ºC) methods compatible with CMOS processing. Common new approaches involve custom hydride precursors, including the $P(GeH_3)_3$,[55] $As(GeH_3)_3$,[130] and SbD_3[16] families of compounds. The results of these endeavors include record high dopant concentrations, ultra-low resistivities, uniform dopant profiles, sharp interfaces, and near perfect activation ratios, enabling the fabrication of working devices.

For *p*-type doping of Ge, boron (B) is the most common source. It is traditionally incorporated by direct implantation from solid B sources. Activation methods include laser annealing or rapid thermal annealing.[124,125] Regardless of the method, the activation ratio has never exceeded 20% at high dopant concentrations beyond 1×10^{20} cm^{-3}. Preamorphization-implantation (PAI) is an alternative strategy to increase the dopant activation of B in Ge. In this case a dose of Ge atoms is first implanted to amorphize the lattice followed by B implantation.[131,132] Although this is proven to work better, it introduces an additional layer of complexity into the doping process. For *in situ* B doping, B_2H_6 has long been the only gaseous source suitable for CVD. This is in sharp contrast with *n*-type doping, for which several CVD alternatives exist, as discussed above. Bogumilowitcz *et al.*[127] reviewed previous work on Ge-doping and reported fabrication of Ge:B materials via reactions of GeH_4 and B_2H_6 at 400°C, obtaining carrier concentrations up to 1×10^{20} cm^{-3} with a substitutional B concentration of 2.2×10^{20} cm^{-3}. D'Costa *et al.* reported studies of *p*-type films grown by CVD of Ge_2H_6 and B_2H_6. They obtained hole concentrations as high as 6.5×10^{19} cm^{-3} with a resistivity of 7×10^{-4} **Ω**·cm,[17] while Fang *et al.* extended the approach to $Ge_{1-x-y}Si_xSn_y$ alloys achieving hole

concentrations of 2.1×10^{20} cm^{-3} with a resistivity of 3.8×10^{-4} Ωcm.[18] On the other hand, MBE *in situ* doping using B is not as common. Radamson *et al*.[19] reported B-doping of Ge at concentrations as high as 8×10^{20} cm^{-3} with a resistivity as low as 3×10^{-4} Ω·cm. However, B-precipitation along (001) and (113) planes began to appear at 1.8×10^{20} cm^{-3} and became more severe at higher levels, hindering possible applications in practical devices.

Gallium is a desirable alternative to B for doping Ge because it has much higher equilibrium solubility (8×10^{19} cm^{-3} at room temperature, and 3×10^{20} cm^{-3} at 350°C, as compared to the negligible solubility for B in Ge in all temperatures),[133,134] offering the possibility for achieving ultrahigh carrier concentrations in Group IV devices. This is particularly useful in the fabrication of *p*-type Ge MOSFETs, in which activated *p*-type carrier concentrations must be above 1×10^{20} atoms/cm^3 in order to reduce the parasitic resistance in the source and drain (S/D) regions. The convenience of using Ga was demonstrated recently in $Ge_{0.95}Sn_{0.05}$ alloys for which the contact resistivity was found to be as low as 1.4×10^{-9} Ω·cm.[135] Furthermore, compared to the small but observable diffusion observed for implanted B in Ge,[123,125] implanted Ga in Ge shows no discernible diffusion after annealing up to 700°C.[136] In addition to the above benefits, prior studies have also reported the observation of superconductivity in highly doped Ge:Ga materials, but a Ga concentration up to 1.4×10^{21} cm^{-3} or 3% Ga is required to achieve this behavior.[137] This represents the highest value reported to date, consistent with the enhanced solubility of Ga compared with B in a Ge host. Note that one issue with these samples is a sizable segregation of Ga atoms near the surface, as evidenced by Rutherford

backscattering spectrometry (RBS), making the material questionable for electronic applications.

Unlike molecular beam epitaxy (MBE) *in situ n*-type doping of Ge, which has been extensively applied utilizing solid sources such as GaAs[138] and Sb,[139] only a handful of studies about MBE *in situ* Ga doping of Ge materials exist. In addition to Ref. 133, Shimura *et al*. reported MBE *in situ* Ga doping of both Ge and $Ge_{1-y}Sn_y$. In the case of the latter, acceptor levels of 1×10^{20} cm^{-3} were achieved in a 7.1% Sn sample.[140] However, this sample had inferior crystallinity, as evidenced by transmission electron microscopy (TEM). Similar Sn content samples (7.8% Sn) with better crystallinity could only be doped up to $p = 5.5\times10^{19}$ cm^{-3}. In the case of pure Ge, a much lower carrier concentration $p < 1\times10^{19}$ cm^{-3} was obtained with an activation ratio of 18%, clearly insufficient for Ge *p*-MOSFET applications. Wang *et al.*[141] reported Ga doping of $Ge_{1-x}Sn_x$ *in situ* using MBE, and claimed active doping up to 3.2×10^{20} cm^{-3}. However, secondary-ion mass spectrometry (SIMS) elemental profiles showed that the Ga levels increase towards the surface due to segregation. This problem becomes more pronounced at higher dopant levels, resulting in rough surfaces and reduced crystallinity as evidenced by X-ray diffraction (XRD). Moreover, this study does not report doping of pure Ge, which, in combination with Ref. 133, suggest that it is difficult to dope Ge with Ga atomic beams using MBE methods. Previous works[20] also investigated the reaction of Ga atomic beams with $P(SiH_3)_3$ and found out that the Ga atoms were not reactive enough to bond with $P(SiH_3)_3$ and form single crystal materials. The above observations imply that Ga atomic beams are not optimal for producing materials containing both Ga and Group IV

elements. In order to get high Ga doping levels in Ge one should either introduce Sn while using an atomic Ga beam, or alternatively consider a more reactive Ga source.

A significant roadblock for the development of viable Ga-doping technologies is the lack of suitable precursors for CVD *in situ* doping. The classic gallium hydride Ga_2H_6 —analogous to B_2H_6—is unstable above -75ºC, precluding its use for practical applications. The ubiquitous metalorganic derivative $Ga(CH_3)_3$, typically used in vapor phase epitaxy of III-V semiconductors[143] has been recently applied as a possible dopant source of Ga.[129] However, this study was using iso-butyl germane as the germanium source, the optimum growth temperature was found to be 670 °C, and the highest dopant concentrations achieved while maintaining reasonable structural quality did not exceed 1×10^{19} Ga atoms/cm^3. Furthermore, carbon contamination is a potential issue due to the presence of multiple methyl groups.

In this chapter, a CVD method to dope Ge films with Ga atoms *in situ* is introduced. The approach is based on a stable and volatile Ga deuteride, $[D_2GaN(CH_3)_2]_2$, which reacts readily with Ge_4H_{10} to deliver Ga dopants controllably and systematically at CMOS compatible ultra-low temperatures of ~360 °C. The CVD Ga-doping method has several key advantages over the state of the art. It can dope Ge over a broad concentration range with nearly full activation ratios, yielding carrier densities between 3×10^{18} cm^{-3} and ~2.6×10^{20} cm^{-3}. This eliminates the need for further annealing or activation steps, which makes the process simple and potentially deployable beyond the laboratory scale. Furthermore, the *in situ* nature of the method allows for independent control of doping

level and junction depth, while delivering flat dopant profiles and sharply defined *p-i* interfaces.

4.2 Experimental

$[D_2GaN(CH_3)_2]_2$ (dimethylamine-gallane, or DMA-Ga) is a relatively stable and reasonably volatile Ga deuteride which was found to be a viable gas source of Ga atoms. The compound is a colorless liquid with a vapor pressure of ~ 1 Torr at room temperature, making it suitable for CVD experiments. It was recently utilized to fabricate a novel class of hybrid semiconductor compounds with compositions $GaPSi_3$,[20] $GaAsGe_3$ and $Ga_{1-x}P_xGe_3$[143] by reactions of the compound with $P(SiH_3)_3$ and $As(GeH_3)_3$ between 370 and 500 °C. The $[D_2GaN(CH_3)_2]_2$ gas source delivers pure Ga atoms at low temperatures by eliminating robust D_2 and $DN(CH_3)_2$ byproducts as described by the reaction

$$[D_2GaN(CH_3)_2]_2 \rightarrow 2Ga + D_2 + 2DN(CH_3)_2 \qquad (4)$$

The $DN(CH_3)_2$ species is pumped away and does not participate in the growth process, leaving behind pure and crystalline epitaxial films devoid of C and N impurities. Calculations of the above decomposition reaction show that the change in Gibbs free energy (ΔG) is negative under the temperature and pressure employed, indicating that the process is thermodynamically favorable. Detailed discussion regarding the reaction of

$[D_2GaN(CH_3)_2]_2$ could be found in Ref. 20. The successful application of the dimethylamine-gallane approach to the growth of Ga-containing III-V-IV alloys motivated the current study to dope elemental Ge with Ga acceptors.

4.2.1 Deposition Methods

Two types of reactors were used to grow the Ga-doped Ge films in this study: a custom-built low-pressure CVD reactor capable of accommodating 1 cm×1.5 cm substrate segments, and a gas source molecular epitaxy chamber (GSME) with full size 4-inch wafer capabilities. Both instruments operate at ultra-low pressures of 10^{-4}-10^{-5} Torr and temperatures below 400 °C. The first reactor was initially employed to establish deposition conditions for optimal incorporation of the Ga dopants. The system provided a convenient way to demonstrate feasibility of the approach by growing multiple samples at high throughput rate using small amounts of specialty chemicals. The gas source molecular epitaxy reactor allowed transitioning the technology to large area Si platforms for preparation of samples that were subsequently used to produce the devices. In both cases, Ge or $Ge_{0.95}Si_{0.05}$ buffer layers were used as template for deposition. These were freshly grown on Si following procedures described in Ref. 71 and Ref. 73. The $Ge_{0.95}Si_{0.05}$ buffers were employed to allow for the separation of the XRD peaks of the Ga:Ge epilayer from those of the buffer layer, allowing unambiguous determination of the lattice constants as a function of Ga content. It is worth mentioning that the initial proof of concept depositions using the low pressure CVD reactor were performed by

growing the Ge buffer layers first *in situ* on the bare Si surface. The Ge source Ge_4H_{10} was synthesized by pyrolysis of commercial Ge_2H_6 and purified as described in Ref. 144. In a typical experiment an appropriate flux of $[D_2GaN(CH_3)_2]_2$ and Ge_4H_{10} was injected directly into the chamber and was adjusted to give a deposition pressure of 1×10^{-5} Torr using a high precision needle valve. The molecular flow was directed towards the growth surface using a nozzle terminating one inch away from the substrate. The latter was heated to 380 °C by passing current through the wafer. Under these conditions, layers with thickness approaching 1.3 μm were produced at an average growth rate of 25-50 nm/min.

The growth on 4" Si substrates was conducted using similar parameters of 1×10^{-4} Torr and 370 °C. In this case, a gaseous mixture of $[D_2GaN(CH_3)_2]_2$ and Ge_4H_{10} in H_2 diluent was used to ensure a homogeneous doping profile over the entire wafer. The growth rate using this approach was slightly lower than above at 15-20 nm/min, yielding layers with final thicknesses ranging from 200-300 nm. The resultant samples produced from either reactor exhibited a smooth and mirror-like appearance devoid of any haziness or other visible surface features, indicating a flat topology in all cases.

4.3 Results and Discussion

4.3.1 Doping and Activation Characterizations

The concentration of Ga atoms incorporated in the films using this new deposition protocol were obtained by SIMS, and the corresponding hole concentrations were determined by infrared spectroscopic ellipsometry (IRSE). The data are summarized in Table 3 for representative samples grown by GSME and CVD. The combination of IRSE and SIMS data allowed for systematic estimates of the activation ratios in the samples, as

Table 3: Atomic concentrations, carrier concentrations and resistivities for representative samples doped with Ga in the range of $3.5x10^{18}$ and $2.67x10^{20}$ cm^{-3}. The absolute SIMS concentrations are very close to the ellipsometry counterparts indicating a high degree of carrier activation over a broad range.

Sample	SIMS Ga concentration ($x10^{19}$ cm^{-3})	IRSE carrier concentration ($x10^{19}$ cm^{-3})	IRSE resistivity ($\Omega \cdot cm$)
Ge:Ga 1 GSME	0.345	0.360	0.01
Ge:Ga 2 GSME	1.74	2.32	0.00115
Ge:Ga 3 GSME	3.29	2.98	0.0018
Ge:Ga 4 GSME	2.18	2.99	0.0016
Ge:Ga 5 GSME	12.5	8.55	0.00085
Ge:Ga 6 GSME	10.3	9.91	0.00074
Ge:Ga 7 GSME	25.2	16.8	0.00045
Ge:Ga 8 GSME	N/A	26.7	0.0004

described below. Figure 27 shows a typical SIMS plot for a Ga doped Ge sample grown on a $Ge_{0.95}Si_{0.05}$ buffer, revealing flat elemental profiles across the film that indicate a homogeneous distribution of the dopant atoms. In addition, a sharp decrease of the concentration profile is observed at the interface, indicating that no diffusion has occurred into the buffer or accumulation onto the surface. A concentration dip is also observed near the interface. This was previously illustrated by SIMS data of MBE *in situ* doped Ge:Ga systems,[133,138] and its origin was attributed to an imbalance between segregation and incorporation of the Ga dopants that occurs at the onset of the deposition process.[133] The Ga contents from SIMS were quantified using a bulk Ge standard implanted with 5×10^{19} atoms/cm^3 of ^{69}Ga. They appear in the second column of Table 3.

The IRSE measurements were conducted at room temperature on a J.A. Woollam instrument. Typical scans were taken at an incident angle of 70° within a photon energy range of 0.03-0.8 eV, with a step size of 0.001 eV. The raw data were fitted using a multi-layer model which consisted of the Si substrate, the Ge buffer layer, a parameterized *p*-type Ge layer, a thin GeO_2 layer and a surface roughness layer. This approach was applied to both sample types grown on $Ge_{0.95}Si_{0.05}$ and Ge buffers and no significant difference was found between them, indicating that the buffer layer does not influence the behavior in any significant manner. The thicknesses of each layer were fitted first, followed by adjustment of the parameters in the *p*-type Ge layer. Generally, the fitting method introduced in Ref. 17 is adopted, in which a Drude term (see appendix) was employed to represent the free carrier response at the long wavelength limit, and 2 or 3 Gaussian oscillators were used to fit the optical transitions between the split-off (*so*),

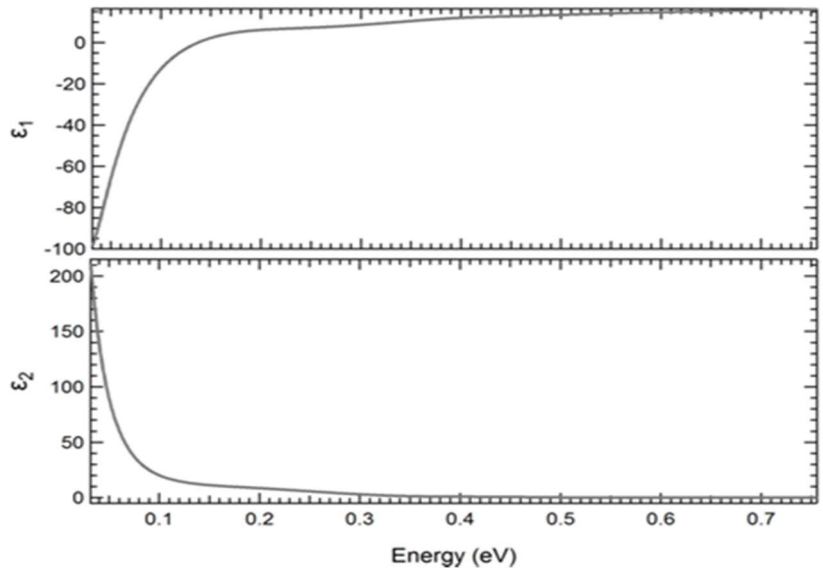

Figure 26: Real and imaginary dielectric functions ε_1 and ε_2 for a Ga doped Ge sample with a carrier concentration of 9.91×10^{19} cm^{-3}.

light-hole (*lh*), and heavy-hole (*hh*) bands. Figure 26 shows plots of the real and imaginary parts of the dielectric function for a heavily doped sample. The Drude response can be clearly seen below 0.1 eV, whereas the shoulder around 0.2 eV corresponds to transitions between the valence bands. The theoretical fits yield the material's static resistivity and average relaxation time. The resistivity values are presented in the fourth column of Table 3 for a series of representative samples along with the active carrier concentrations in the third column. The latter span a wide range of values from 10^{18} to 10^{20} /cm^3, illustrating the effectiveness of the doping approach in tuning the doping levels over a wide window as required for device flexibility. Note that the determination of active concentrations from IRSE requires the additional knowledge of the carrier effective mass m^*. In previous work on B-doped Ge, D'Costa and coworkers used an effective mass $m^* = 0.28m_0$, where m_0 is the free-electron mass.[17] At low doping levels

the calculated effective mass is in excellent agreement with the value proposed by D'Costa.[17] But as the hole concentration increases beyond $p \sim 2\times10^{19}$ cm^{-3}, the non-parabolicity effects cannot be neglected. The carrier concentrations that are quoted in Table 3 use the calculated doping-dependent effective mass shown in Figure 26, which for each sample is obtained self-consistently in an iterative fit.

The ellipsometry active carrier concentrations and the SIMS Ga contents were used to obtain the activation ratio values. These are plotted in Figure 28 (red dots) and compared with trends from prior studies of *p*-type doping of Ge in the literature. The methods used in these studies are summarized in the legend. Ion implantation methods are referred to as "II". They require complicated multistep treatments including the SiO_2 capping of the films, chemical rinsing, rapid thermal annealing (RTA) or excimer laser annealing (ELA). In the case of the samples produced by preamorphization implantation

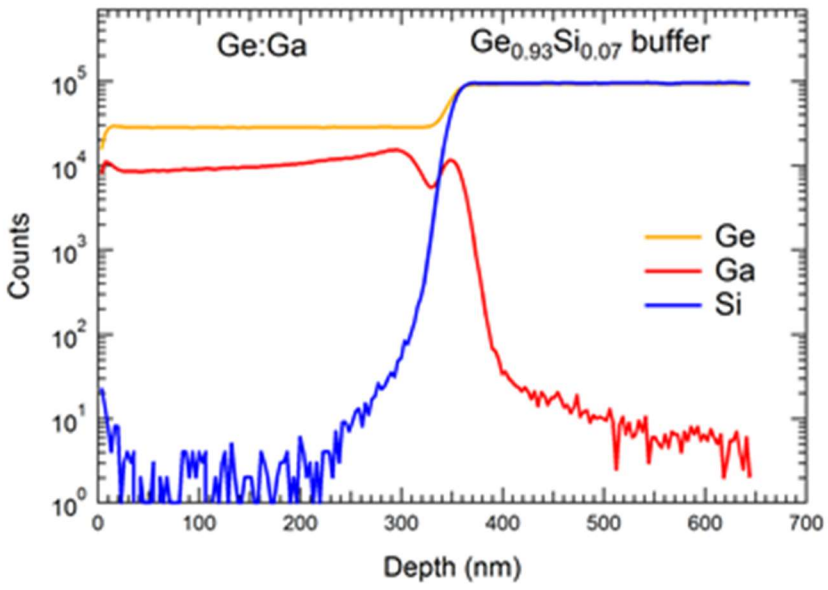

Figure 27: SIMS profile for a Ga doped Ge sample grown on top of a $Ge_{0.95}Si_{0.05}$ buffered Si. The Ga atomic concentration is N_{Ga} =1.03×10^{20} cm^{-3}.

methods (denoted as PAI in the figure) the process is further complicated by the implantation of Ge atoms prior to the dopant atom implantation. It is apparent from Figure 28 that within experimental error near full activation has been achieved in this study for Ga concentrations up to about 10^{20} atoms/cm^3, a dramatic improvement over all other *p*-type doping protocols. For samples with higher concentrations the activation drops down to ~70%. Here it is emphasized that the near-unity activation ratio over a broad doping range is likely a result of the low temperature (360 - 400 °C) conditions employed in these experiments and afforded by the high reactivity of the Ga hydride source. The facile dissociation of the latter likely facilitates substitutional incorporation

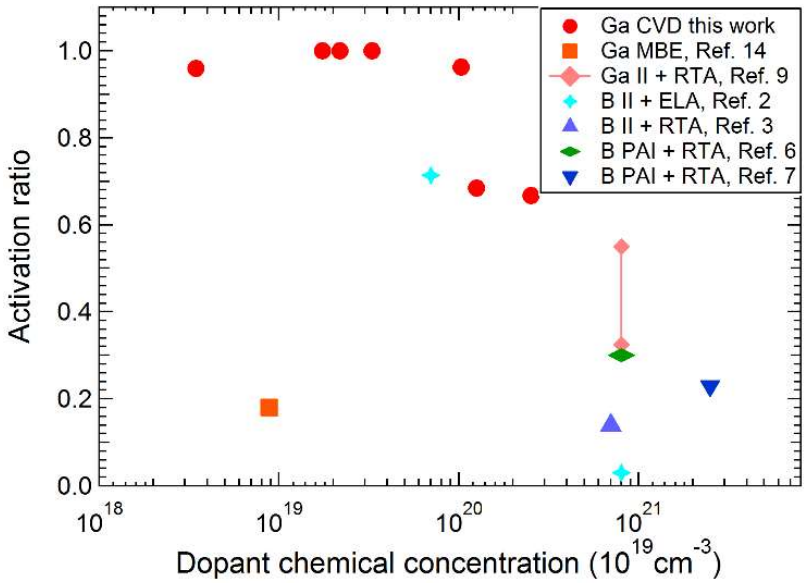

Figure 28: Plots of Ga dopant activation ratios in Ge. Results obtained from this study are shown by red dots. Analogous results from literature accounts are presented by the various colored symbols and are also summarized in the inset. The "II" sign indicates ion implantation while ELA and RTA denote excimer laser annealing and rapid thermal annealing, respectively. The data clearly make the case that the current study represents one of the more versatile and efficient methods for doping and super doping Ge.

and full activation without the need for further thermal treatments and activation steps. By contrast, previously reported activation ratios for B and Ga doping by other methods mostly lie below 40%, with the exception of Ref. 124 in Figure 28, which shows an activation ratio of ~ 70% for a single sample doped with B atoms. In this case, the sample was prepared by ion implantation followed by excimer laser annealing (ELA). The orange square in the plot corresponds the results reported in Ref. 18 for *in situ* MBE doping Ge by Ga yielding an activation ratio of ~20% for concentrations near $10^{19}/cm^3$. Similarly low doping ratios are reported by Refs. 125, 128, and 129 for B-doped Ge by ion implantation routes followed by RTA processing.

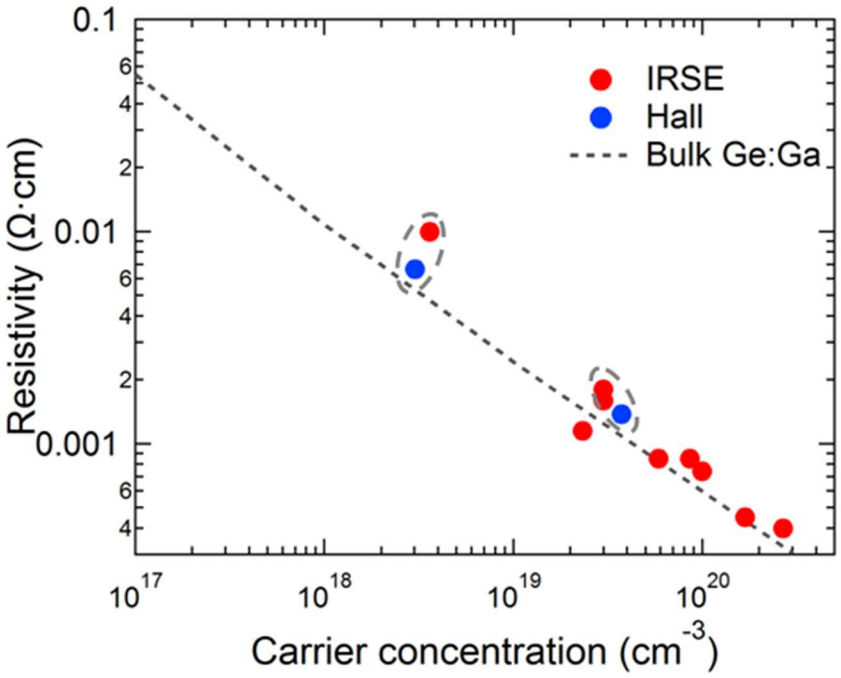

Figure 29: Resistivity of Ge:Ga samples obtained from electrical and ellipsometry measurements. The dashed curve shows a fit to bulk *p*-type Ge samples with $p < 6\times10^{19}$ cm^{-3}(Ref. 73). Data points circled together are from the same samples.

The resistivity values for these samples listed in Table 3 are plotted in Figure 29 as a function of the hole concentration (red dots). Electrical measurements of the resistivity are also shown for selected samples (blue dots) plotted against Hall values of the carrier concentrations. There is good agreement with the IRSE data. The resistivity is further compared with an extrapolation of the best-fit curve for bulk *p*-type Ge data provided in Ref. 145. The samples in this case were mostly doped with Ga at $p < 6\times10^{19}$ cm^{-3}. The trends in Figure 29 indicate that the film resistivities are consistent with those in bulk materials, further validating the CVD approach to Ga doping.

Table 4, Comparison of this CVD approach to Ga doping and various literature methods focusing on Ga as well as B doping (PAI: preamorphization implantation; II: ion implantation; ELA: excimer laser annealing). The table highlights best carrier concentration and resisitivities. The values with asterisks were calculated from published sheet resistances and may be affected by large errors whenever the dopant distribution is not box-like.

Approach	Dopant	Method	Max. p ($\times10^{19}$ cm^{-3})	resistivity($\Omega\cdot$cm)
this study	Ga	CVD	26.7	4×10^{-4}
Shimura[140]	Ga	MBE	0.8	3.3×10^{-3}
Hellings[136]	Ga	II + RTA	26(44)	2.2×10^{-4}*
Bogumilowicz[127]	B	CVD	10	6×10^{-4}*
Radamson[19]	B	MBE	30*	3×10^{-4}
Impellizzeri[124]	B	II + ELA	0.5	N/A
Satta[131]	B	PAI + RTA	24	5.6×10^{-4}*
Mirabella[132]	B	PAI + RTA	57	2.2×10^{-4}*

The advances offered by this new approach are further highlighted in Table 4 which summarizes data from the different studies mentioned above focusing on growth of *p*-type Ge, including Ga and B doping performed by CVD, MBE, and implantation-annealing methods. Carrier concentrations (*p*) and resistivity values are listed and compared. Again, in this format, the data further confirm the viability of the CVD approach to Ga-doping in Ge. In fact, the carrier concentrations are higher and the resistivities are lower than in any other CVD experiment (with reasonable sample quality), regardless of *p*-type dopant. Here the highest hole concentrations are comparable to the values obtained by the preamorphization implantation (PAI)+RTA method,[131,132] which requires at least four steps including SiO_2 capping layers, Ge implantation and thermal treatments.

4.3.2 Structural and Morphological Properties

The materials properties of all samples produced in the study were characterized for structure and morphology by high-resolution X-ray diffraction, Rutherford backscattering (RBS), cross sectional transmission electron microscopy (XTEM) and atomic force microscopy (AFM). Most samples were grown on Ge buffered Si wafers to facilitate growth of defect-free epilayers via homo-epitaxy. However, for the purpose of investigating the substitution of Ga atoms in the lattice parameters of the Ge host lattice several samples on $Ge_{0.95}Si_{0.05}$/Si platforms were produced. Figure 30 shows diffraction spectra including on axis (004) peaks (blue line) and (224) reciprocal space maps

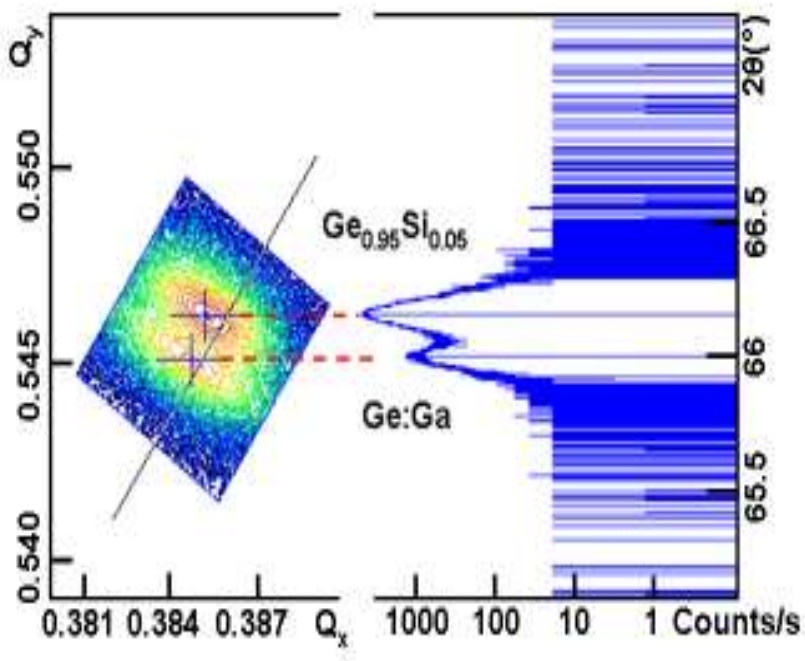

Figure 30: XRD (004) and (224) scans for a Ga doped Ge sample grown on top of $Ge_{0.95}Si_{0.05}$ buffered Si with a $1.0x10^{20}$ cm^{-3} Ga active concentration. Distinct sets of peaks corresponding to the buffer and epilayer are shown making it possible to determine the in-plane and vertical lattice parameters of the heavily doped material.

(colored contours) of the $Ge_{0.95}Si_{0.05}$ buffer and the Ge:Ga epilayer for a sample doped with ~$1.0x10^{20}$ cm^{-3} Ga acceptor atoms. The epilayer is seen to be fully relaxed relative to the buffer and slightly tensile strained to Si as indicated by the position of the peak maximum above the relaxation line. The relaxed (cubic) lattice parameter is determined to be 5.65766 Å which is nearly identical to the average Ge reference value 5.65694 Å measured under the same conditions. Note that no contraction of the Ge lattice was observed in these experiments due to the smaller size of the Ga atom size and a reduced value of the valence band absolute deformation potential relative to the band gap

deformation potential. For samples grown on Ge/Si(100) the peaks from the Ge and Ga:Ge components completely overlapped particularly for the low Ga content materials making it impossible to differentiate the relative contributions. Regardless of the template used for growth, the XRD plots of the samples corroborated the single crystal nature and epitaxial alignment between the Si wafer, the Ge(Si) buffer, and the doped Ge:Ga epilayer. RBS measurements were performed to investigate the film thickness and crystallinity by comparing the random and channeled backscattering spectra. Since the Ga contents in the samples were all below 1%, the Ga signal could not be clearly detected, even for the higher Ga content cases, given the close proximity of the Ga backscattering energy and that of Ge. This is illustrated in Figure 31 which shows random and channeled data of a Ge:Ga sample grown on Ge-buffered Si, with 9×10^{19}

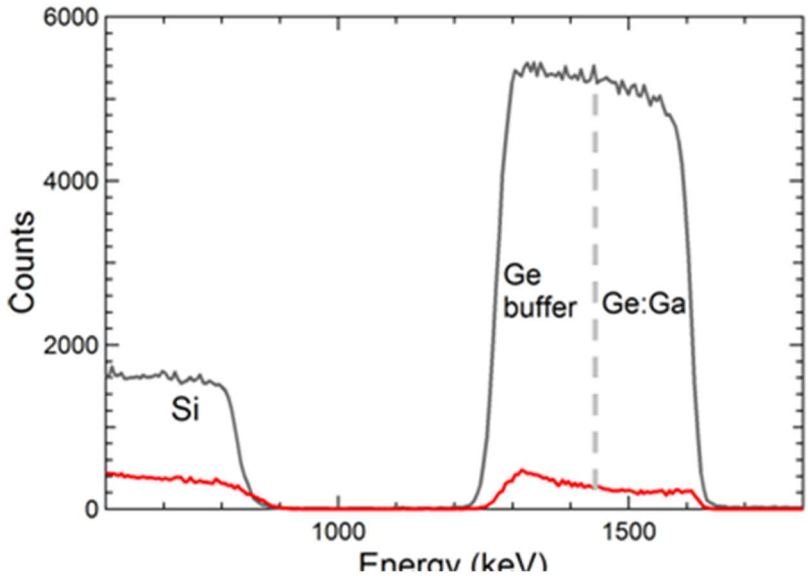

Figure 31: RBS random (black line) and channeled (red line) spectra for a Ga doped Ge sample with carrier concentration of 1×10^{20} cm^{-3}. The vertical dotted line delineates the Ge:Ga epilayer from the Ge buffer. No Ga signal is observed due to the potential overlap with the neighboring Ge background.

cm^{-3} carrier concentration and 230 nm *p*-layer thickness. Excellent channeling has been achieved as seen by the reduced intensity of the red line spectrum over the entire film thickness. The χ_{min} ratio of the aligned over the random peak heights is ~4% indicating that the doped layer is fully commensurate upon the Ge buffer and the microstructure is likely devoid of interfacial defects. The excellent crystallinity revealed by RBS and corroborated by HR-XRD is consistent with the near-unity dopant activation obtained from SIMS and IRSE measurements.

Figure 32 shows RBS and SIMS data for a 1300 nm thick sample incorporating 2.32×10^{19} cm^{-3} carrier concentration. A comparison of the random (black line) and aligned (red line) spectra supports excellent crystallinity as expected due to the homo-

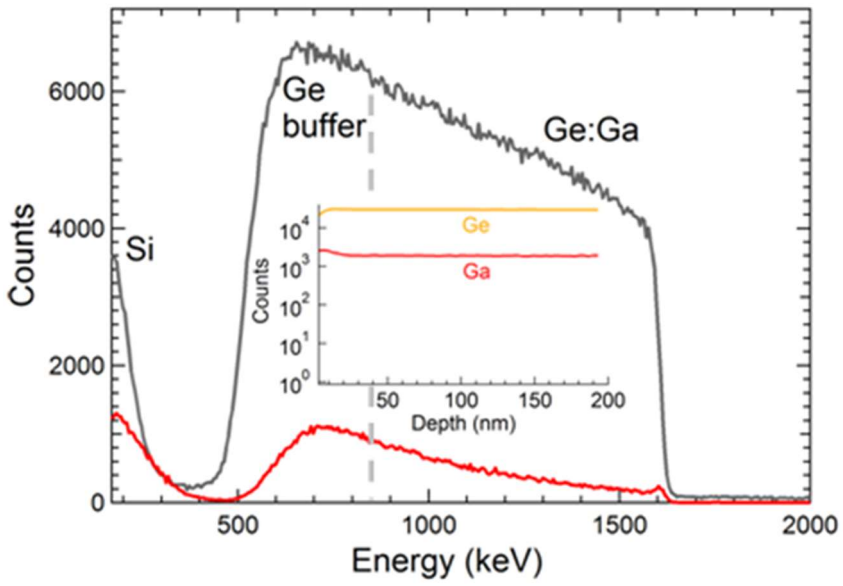

Figure 32: RBS random (grey line) and channeled (red line) spectra for a 1.3 μm thick Ge:Ga layer grown upon Ge buffered Si(100), exhibiting a carrier concentration of 2.32×10^{19} atoms/cm^3. The inset shows the SIMS profile for the top 200 nm thickness, revealing a homogeneous distribution of the elements. The grey line in the main panel delineates the Ge buffer and Ge:Ga segments of the *i-n* layer spectrum.

epitaxial nature of the crystal growth and the large thickness of the resultant epilayer. The grey line marks the transition from the Ge buffer to the doped epilayer, illustrating qualitatively the relative thicknesses. The inset of Figure 32 shows the SIMS profiles for Ge and Ga atoms in the top 200 nm segment of the same sample, revealing a homogeneous Ga distribution with no sign of surface accumulation. The large thickness combined with the near perfect crystallinity and uniform doping is a significant advancement due to the potential for rapid deposition of full *p-n* or *p-i-n* diode stacks with thick bulk-like active layers.

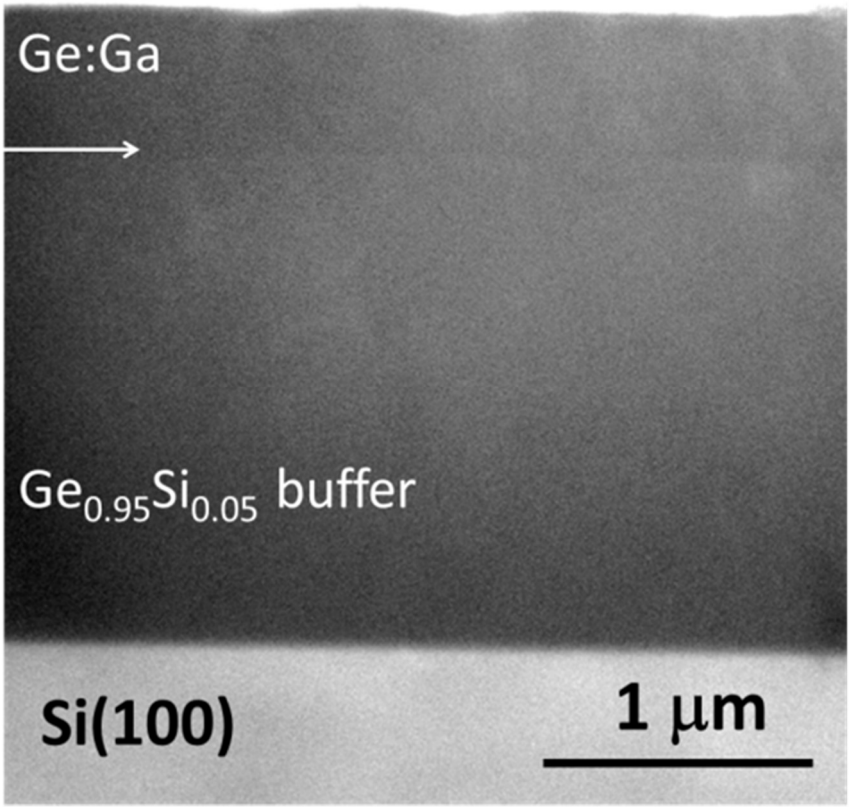

Figure 33: XTEM image of a Ge:Ga layer grown upon a $Ge_{0.95}Si_{0.05}$ buffered Si wafer. The carrier content is 9.9×10^{19} cm^{-3} and the thickness is 500 nm. Horizontal arrows show the *p/i* interface.

Finally, cross-sectional transmission electron microscopy (XTEM) was employed to investigate the bulk microstructure. Figure 33 shows a typical image of a Ge:Ga layer grown upon a $Ge_{0.95}Si_{0.05}$ buffer with a high carrier concentration of 9.9×10^{19} cm^{-3}. No discernible interface defects or threading dislocations are visible in the epitaxial layer within the field of view of the low magnification image. The *p/i* interface (highlighted by horizontal arrows) is uniform and the top surface is fairly planar. No clustering or segregation is apparent, corroborating the homogeneous distributions of Ga revealed by the SIMS measurements

4.3.3 Photoluminescence Properties

Room temperature photoluminescence (PL) measurements were carried out on a custom-built PL system, consisting of a 980 nm CW IR laser with a 400 mW output power, an optical chopper that provides modulation and reduces the average power by a factor of 2, a 1064 nm long-pass filter, a lock-in amplifier, a Horiba Jobin-Ivan monochromator, and a LN_2-cooled InGaAs photodetector. A detailed description of the PL system can be found in Ref. 146. The PL spectra of the samples were collected and corrected for filter and detector responses, and then fitted using a multi-peak model. For intrinsic or *n*-type doped Ge, a typical PL profile comprises a main strong peak associated with emission from the direct band gap E_0 and a weaker counterpart attributed to indirect-gap emission. The case of *p*-type Ge was studied by Wagner and Viña[147] in experiments performed at low temperatures, with carrier concentrations ranging from

6×10^{18} to 7.8×10^{19} cm^{-3}. Wagner and Viña observed some additional transitions in the PL spectra. Similar peaks were observed in these Ge:Ga samples. Figure 34 shows PL spectra (after filter and detector response correction) of Ge:Ga samples with p = 2.32×10^{19} cm^{-3}, 9.9×10^{19} cm^{-3} and 2.67×10^{20} cm^{-3}, and thicknesses of 1300 nm, 400 nm, and 360 nm, respectively. The spectrum from the $p = 2.32\times10^{19}$ cm^{-3} sample shows a

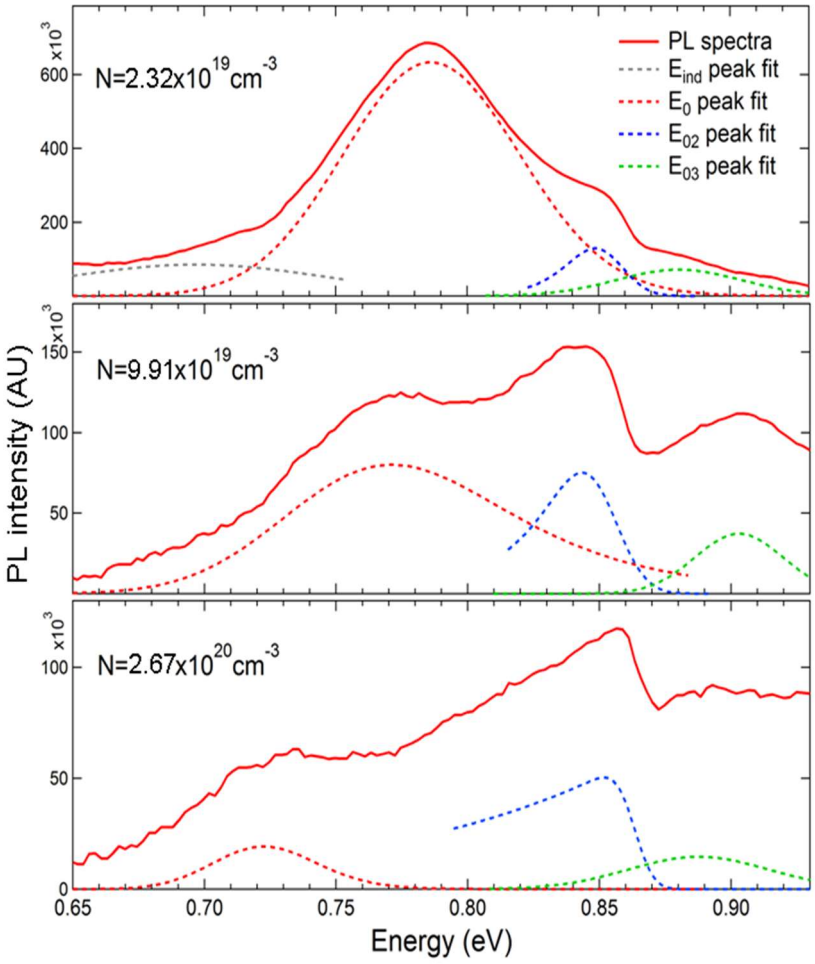

Figure 34: PL spectra and peak fitting for Ge:Ga samples with carrier concentrations of 2.17×10^{19} cm^{-3}, 8.63×10^{19} cm^{-3} and 2.17×10^{20} cm^{-3}. Gray, red, blue, and green dashed lines represent best fits to different transition peaks. For the middle and bottom panels, linear bases (not shown) were used in data fitting.

main peak near 0.79 eV, which is assigned to the direct gap, and a very weak feature below 0.70 eV which is believed to be associated with the indirect gap. In addition to these peaks, there is a clear high-energy feature near 0.85 eV and a shoulder at even higher energies. As the doping concentration increases, the high-energy peaks become dominant and the E_0 peak shifts to lower energy due to band gap renormalization. A reduction of the E_0 peak intensity was also observed. One possible reason is non-radiative recombinations associated with increased doping, such as Auger recombination, which has an exponential relationship with doping levels. Another plausible explanation to the characteristic PL line shapes of *p*-type Ge requires understanding to the physical origin of the high-energy PL feature. This high-energy peak has been assigned by Wagner and Viña to direct transitions without momentum conservation, but here a somewhat different explanation is provided. It is speculated that this extra peak is caused by "hot electrons" that were excited to positions away from the Γ minimum in the conduction band. For the cases with no *p*-type doping, these electrons will cascade down to the Γ valley minimum and contribute to E_0 transition. However, with the presence of a large amount of holes in the valence band expanding away from the Γ valley maximum, a hot electron could readily combine with a hole right below it, emitting a photon with higher energy. As a result, with increasing *p*-type doping there is an increase in this high-energy peak intensity and a decrease in E_0 intensity, simply because fewer electrons made to the Γ valley minimum. Note that the energy of this peak remains almost constant at ~0.85 eV over the whole doping range. This might be due to a fortuitous cancellation of the negative renormalization shift with the positive shift observed as the Fermi level moves

further into the valence band. A full account of these phenomena will be published elsewhere.

4.3.4 Diode Fabrication and Testing

The results above illustrate that reactions between Ge_4H_{10} and $[D_2GaN(CH_3)_2]_2$ produces *p*-type Ge using conventional low-temperature CVD. To investigate the device implications of this discovery, prototype photodiodes were fabricated and the I-V curves and electroluminescence response were measured. The devices are based on a simple design containing a *n*-Ge/*i*-Ge/*p*-Ge stack, as schematically illustrated in Figure 35(a). The whole architecture was grown using Ge_4H_{10} as the Ge source on Si (100) substrates. First, a 560 nm *n*-Ge layer was grown using $P(GeH_3)_3$ as the source of P dopants. This bypasses the inherently defective Si interface, eliminating the effect of carrier recombination traps and problems due to contacts with the Si substrate. Immediately thereafter, a 560 nm thick intrinsic region was produced, followed by a 200 nm *p*-Ge:Ga top electrode. The whole stack was fabricated entirely in the same reactor without interruptions or *ex situ* processing steps, allowing for seamless integration of the different layers without introducing undesirable oxide interfaces or other external impurities. The devices in circular mesa geometries were produced using procedures similar to those previously reported for the fabrication of analogous Ge photodiodes.[142] Figure 35 provides details of diode sizes, metal contacts, doping levels and thicknesses of the diode components. Current-voltage measurements were conducted and the plots are shown in

Figure 35(b) revealing similar diode behavior in all cases regardless of mesa size. The dark current densities at 1.0 V reverse bias fall in the 5×10^{-3} ~1×10^{-2} A/cm^2 range. This is

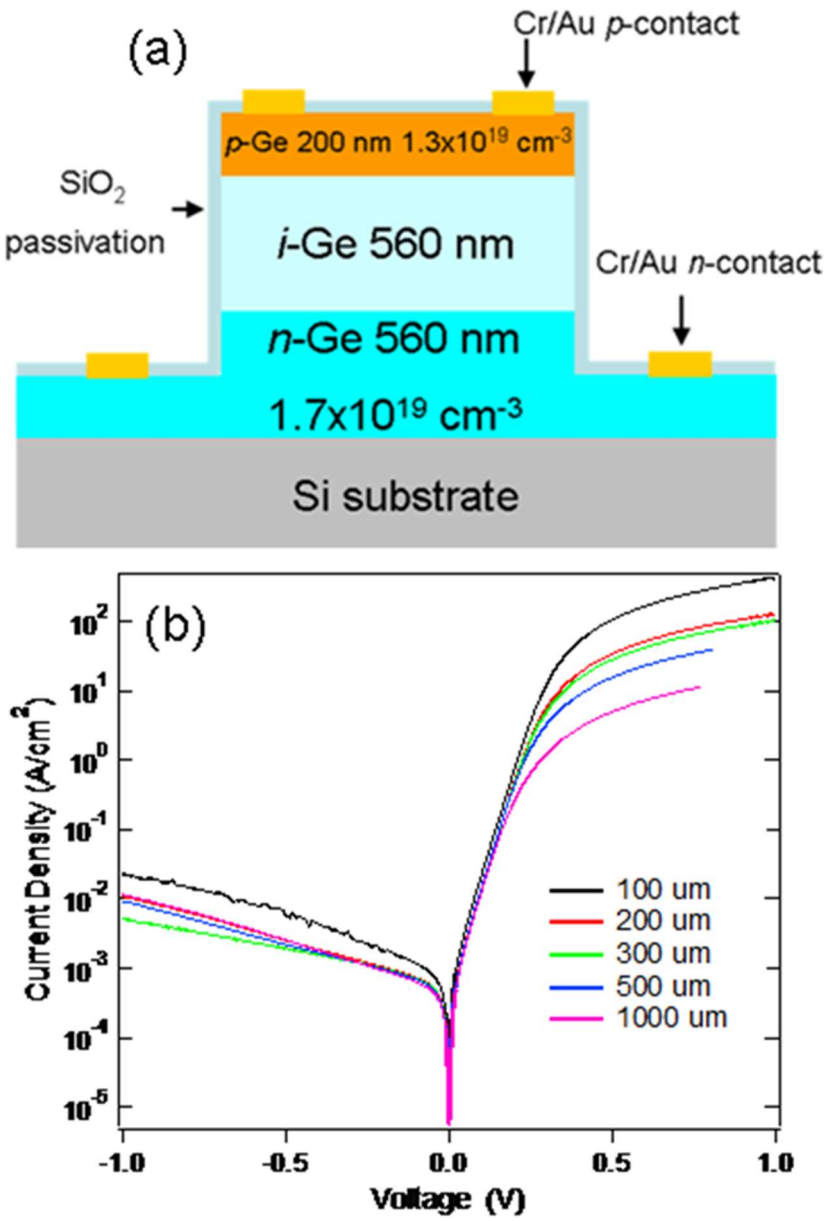

Figure 35: (a) Schematic of the Ge *p-i-n* device showing layer thicknesses, doping and compositions. (b) Current voltage plots of diodes with mesa diameters ranging from 100 µm to 1000 µm.

comparable to the best performing Ge *p-i-n* photodiodes reported earlier using Ge:B *p*-type layers.[148]

The above diodes were then used to measure electroluminescence (EL). The spectra from a representative 300 micron size device are plotted in Figure 36 as a function of injection current. All spectra contain a strong peak centered at ~0.78 eV corresponding to direct gap emission. This is slightly red-shifted relative to bulk Ge at 0.80 eV due the presence of a residual tensile strain in the Ge layers. Furthermore, the peak position shifts slightly towards to lower energy with increasing injection current, likely due to the heating induced by the high current flowing through the device.

In addition to the main peak, a second lower intensity peak is seen at ~0.67 eV and this is attributed to indirect band gap emission. The line shapes of both features are

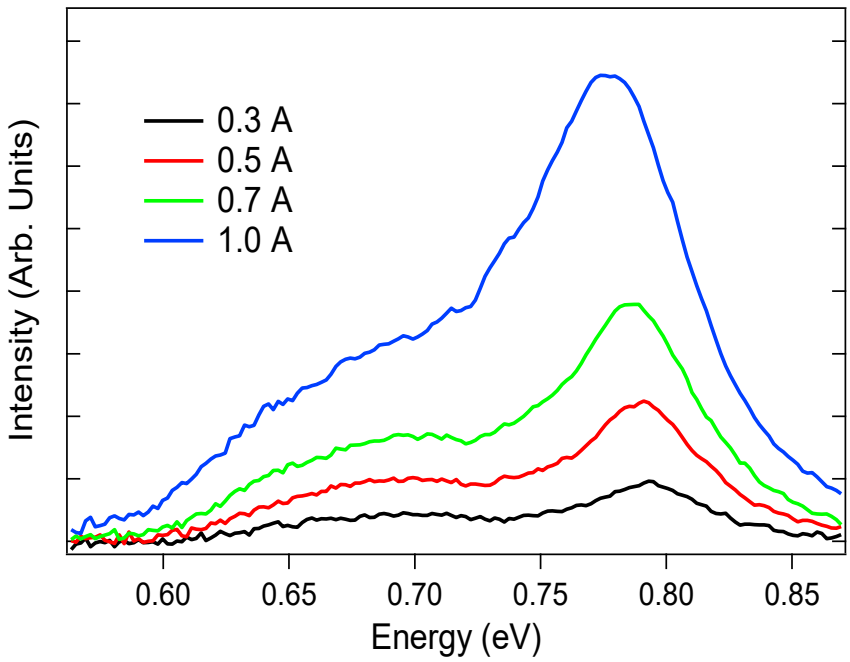

Figure 36: EL spectra of a 300 µm Ge *p-i-n* photodiode using Ge:Ga as the *p*-layer under different injection currents.

consistent with those observed from analogous studies involving Group IV materials containing Ge. Notice that in a *p-i-n* device the emission originates predominantly from the intrinsic layer. Therefore, the EL spectra in Figure 36 do not show the emission features in Figure 34 that are characteristic of *p*-type Ge. Collectively the results indicate that the newly introduced Ga hydride is a promising *in situ* source for achieving device quality doping under low thermal processing conditions.

4.4 Summary

In summary, a CVD approach to *p*-type doping of Ge with Ga has been presented. This approach takes advantage of the $[D_2GaN(CH_3)_2]_2$ (dimethylamine-gallane, or DMA-Ga) precursor, a reasonably volatile Ga deuteride which at the growth temperature decomposes yielding Ga atoms that are readily incorporated into the growing film. The resulting films have structural properties comparable to those of pure Ge films, with no signs of Ga-induced defects or precipitation. Doping concentrations and activation ratios are shown to be superior to those previously measured in *p*-type Ge films prepared by any method, providing a striking confirmation of the benefits expected from the higher solubility of Ga in Ge relative to B, which until now represented the state-of-the-art *p*-type dopant for Ge. A *pin* device containing a Ga-doped *p*-layer is shown to have I-V characteristics and optical properties comparable to the best B-doped analogues fabricated in this laboratory. The study presented here suggests that the $[D_2GaN(CH_3)_2]_2$

route represents an intriguing alternative to achieve the ultra-low resistivities needed for Ge-based CMOS.

Chapter 5

SYNTHESIS AND STRUCTURAL AND OPTICAL PROPERTIES OF III-V-IV HYBRID ALLOYS: $Ga(As_{1-X}P_X)Ge_3$ AND $Al(P_{1-X}Sb_X)Si_3$ SEMICONDUCTORS

Portions of this chapter were reprinted from Wallace, P.M.; Sims, P.E.; Xu, C.; Poweleit, C.D.; Kouvetakis, J.; Menéndez, J. *ACS Appl. Mater. Inter.* **2017**, *9*, 35105 with permission from ACS Publishing.

Synopsis

In this chapter synthesis of $Ga(As_{1-x}P_x)Ge_3$ alloys on Si(100) substrates is described using chemical vapor deposition reactions between $[D_2GaN(CH_3)_2]_2$, and $P(GeH_3)_3$ and $As(GeH_3)_3$ precursors. These compounds were chosen to promote the formation of $GaAsGe_3$ and $GaPGe_3$ building blocks, which interlink to produce the desired crystalline product. $Ge_{1-x}Si_x$ buffer layers were used whose lattice constants were matched to the epilayer. This approach yielded single phase materials with excellent crystallinity devoid of mismatch induced dislocations. As-rich samples exhibited photoluminescence with wavelengths similar to those observed previously in pure $GaAsGe_3$ indicating that the emission profile does not change in any measurable manner by replacing As by P over a broad range up to $x = 0.2$. Furthermore the PL data suggested a large negative bowing of the band gap as expected due to strong valence band localization on the As atoms. A second material system comprising of Al-Sb and Al-P

pairs in a Si matrix are presented with the hope of inducing unique optical properties due to the inclusion of a heavy Group V element.

5.1 Introduction

Since the 1960s, compound III-V semiconductors have been used for the fabrication of light emission and detection devices such as LEDs and solar cells. Many of the most useful materials incorporate Ga as the group-III element. Examples include GaP green LEDs and GaAs-based high efficiency solar cells.[149] Significant effort has been applied to improve the efficiency of these devices and to tune the band structure to incorporate a wide range of operating wavelengths, from the UV to IR. However, much of this work has focused on alloys between the various III-V compounds, and the opportunities afforded by alloying the latter with group IV semiconductors have been largely limited to lattice matched systems such as $(Ge_2)_{1-x}(GaAs)_x$.[22,150-152] This is due to the difficulties encountered in synthesizing device quality III-V-IV alloys, including phase separation and formation of anti-phase domains.[152]

Recently a new approach for synthesizing hybrid III-V-IV alloys was demonstrated by utilizing custom made chemical precursors that avoid the above issues by enabling the incorporation of pre-formed tetrahedral building blocks with direct III-V bonds into the growing crystal.[24-26,153] While the initial work in this area made use of atomic beams of the Group III atoms, molecular sources have proved more successful for this purpose by enabling the synthesis of a broader range of alloy materials. Specifically,

the use of Ga-hydride precursors, in combination with $P(SiH_3)_3$ and $As(GeH_3)_3$, allowed the exploration of the $(GaP)_ySi_{5-2y}$ and $(GaAs)_yGe_{5-2y}$ alloy systems, respectively.[20,143] Epitaxial films of the former alloy were found to have increased absorption relative to crystalline Si in the visible portion of the spectrum, suggesting that it may be useful for solar cell applications. It was also found to have a lattice constant between that of GaP and Si, fairly close to the Vegard's law prediction of a linear average. This allows the alloy to be grown on Si substrates with only a minor lattice mismatch. In contrast, the $(GaAs)_yGe_{5-2y}$ system exhibited large variations from the values predicted by linear interpolation between the two end members, both in terms of band gap and lattice constant. The band gap was measured to be between 0.5 - 0.6 eV by photoluminescence indicating significant negative bowing, in agreement with theoretical predictions and prior absorption measurements.[23,154] On the other hand the lattice constants exhibited a large positive deviation from the calculated values. A possible explanation is the formation of ordered bonding arrangements by interlinking $GaAsGe_3$ tetrahedral units featuring the III and the V components as third nearest neighbors. Based on these observations, one can conclude that the scope for tuning the properties of III-V-IV alloys based on composition is broader than previously thought. Further exploration of such alloys and even ternary and quaternary systems with different compositions may reveal further opportunities for band gap and lattice engineering. Moreover, such studies are extremely interesting from a fundamental scientific perspective, since they may disclose hitherto unknown phenomena.

With the above considerations in mind, the synthesis of a new series of $Ga(As_{1-x}P_x)Ge_3$ alloys assembled from $GaPGe_3$ and $GaAsGe_3$ building blocks is reported. The choice of the above system as a potential target was partly motivated by interest in exploring light emission with tunable wavelengths above that of $GaAsGe_3$ (E_g > 0.5 - 0.6 eV) by incorporating P in place of As in the Group IV sub-lattice. The synthetic strategy followed CVD reactions of $[D_2GaN(CH_3)_2]_2$, with $P(GeH_3)_3$ and $As(GeH_3)_3$ precursors. This approach produced monocrystalline $Ga(As_{1-x}P_x)Ge_3$ films with concentrations x = 0 - 1 thus providing samples for systematic band gap and lattice engineering over the entire composition range. The principal outcome of this study was the development of new single-phase alloys that exhibited excellent crystallinity allowing an unambiguous determination of the fundamental properties. Samples with As-rich compositions featured PL with wavelengths similar to that observed for $GaAsGe_3$ analogues, indicating that the alloys possess the necessary quality for optical applications.

The creation of functional alloys in this case was enabled by utilizing for the first time lattice engineered $Ge_{1-x}Si_x$ buffer layers with continuously tunable lattice constants that exactly matched the dimensions of the desired product. The buffers were grown at ultra-low temperatures using chemically designed CVD routes. They exhibited strain free microstructures, flat surfaces and large thicknesses—exceeding 2 microns—making them ideal platforms for subsequent integration of defect-free $Ga(As_{1-x}P_x)Ge_3$ epilayers.

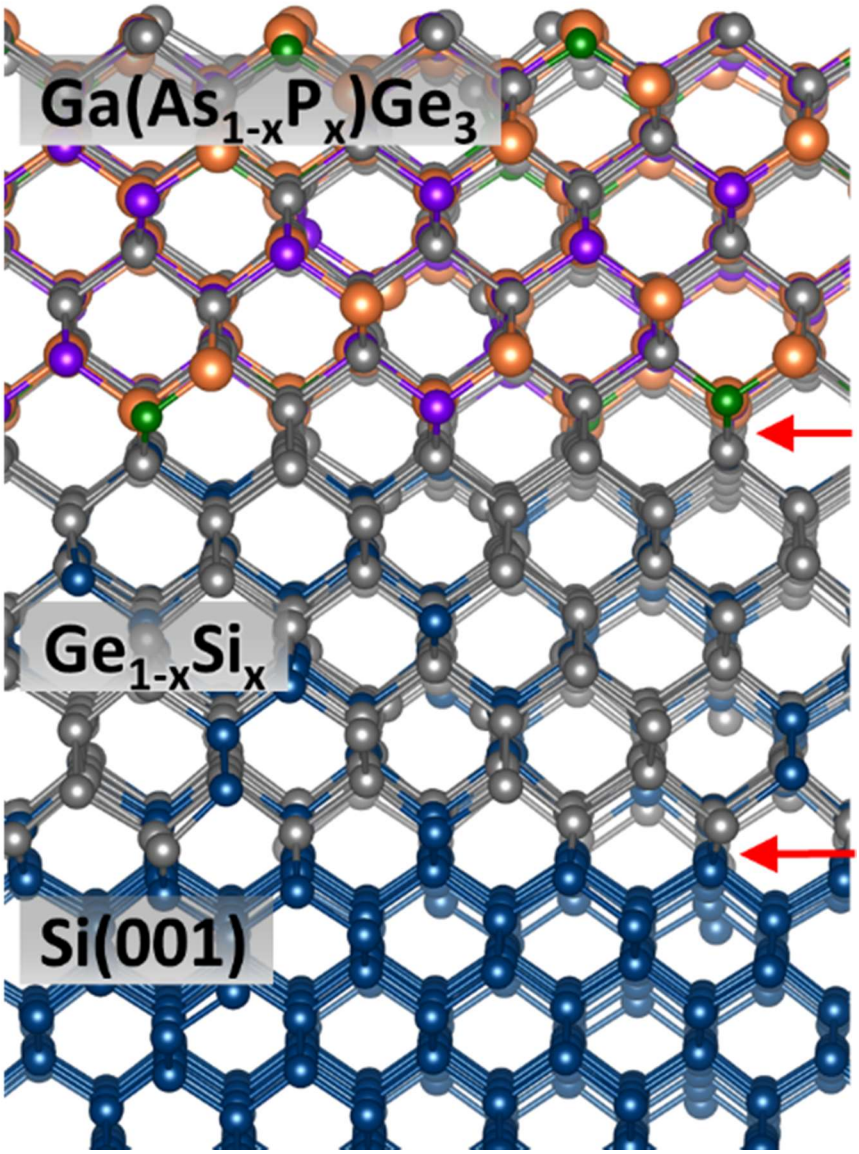

Figure 37: Structural model showing the $Ge_{1-x}Si_x$ buffer layer grown upon Si(100). The amount of Si (x) can be tuned to produce templates that reflect the dimensions of the ternary phase leading to seamless integrations of the two materials. The Ge, Si, As, P, and Ga atoms are represented by grey, blue, purple, green, and orange spheres, respectively. The interfaces in the hetero-structure are marked by red arrows.

In addition to the $Ga(As_{1-x}P_x)Ge_3$ system, alternative Si-based III-V-IV hybrids with the formula $Al(P_{1-x}Sb_x)Si_3$ were pursued. This system is similar to well-established $(AlP)_ySi_{5-2y}$ alloys with the additional incorporation of a AlSb pairs alongside AlP. Pure AlSb has a large lattice constant (6.1 Å) relative to Si (5.43 Å). While the large difference in size between the two material classes is a hurdle for growth of these alloys, it may also result in unique and interesting optical properties in the near-IR range. In addition to favorable optical properties, some compositions of $Al(P_{1-x}Sb_x)Si_3$ lattice match to Ge and GaAs. These alloys could potentially be used as buffer layers between Ge and GaAs to allow integration of III-V and Group IV materials.

5.2 Experimental

As indicated above, the growth of $Ga(As_{1-x}P_x)Ge_3$ films was conducted using $[D_2GaN(CH_3)_2]_2$ as the source of Ga. The compound was synthesized using previously reported methods.[154,155] The deuterated Ga precursor was used in this case because it is kinetically more stable than the isotopic H analogue making the material easier to handle and store for extended time periods. A mixture of $P(GeH_3)_3$ and $As(GeH_3)_3$ was used as sources of P, As, and Ge. Appropriate molar amounts were combined to form mixtures of P, As, and Ge in proportions that closely controlled the target alloy composition within the desired range. Note that in all cases, the P/As ratio in the films was half that of the P/As ratio in the mixture, presumably due to the higher reactivity of $As(GeH_3)_3$ relative to $P(GeH_3)_3$. Accordingly, the mixtures were adjusted to compensate for this condition.

All depositions were performed on $Ge_{1-x}Si_x$ buffer layers grown upon four-inch Si(100) wafers with resistivities of 0.01 Ω·cm. $Ge_{1-x}Si_x$ alloys are the templates of choice for this purpose because the lattice constant of Si (5.431 Å) and Ge (5.657 Å) closely match those of GaP (5.450 Å), GaAs (5.654 Å) and Ge (5.657 Å) end members, allowing design of platforms with continuously tunable lattice parameters akin to those of the corresponding $Ga(As_{1-x}P_x)Ge_3$ alloys. Figure 37 illustrates the $Ge_{1-x}Si_x$ on Si(100) buffer layer concept for epitaxy-driven synthesis of $Ga(As_{1-x}P_x)Ge_3$ alloys. This strategy provides unprecedented flexibility in lattice engineering for epitaxial stabilization of

Table 5: Summary of $Ga(As_{1-x}P_x)Ge_3/Ge_{1-x}Si_x$ sample data for pseudomorphic films (top segment of the table) and lattice matched analogues (lower segment). The absolute compositions for the epilayers and the buffers were measured by RBS. The cubic lattice parameters (a_0), the deviations (Δa_0) from Vegard's law, and the strain values for all samples were obtained from XRD data.

Film Composition (RBS)	Buffer Composition (RBS)	a_0 (Å)	Δa_0 (Å)	Strain %	Relaxation %
Pseudomorphic films					
$GaP_{0.01}As_{0.99}Ge_3$	$Ge_{0.88}Si_{0.12}$	5.6624	+0.0066	-0.3970	32.67
$GaP_{0.20}As_{0.80}Ge_3$	$Ge_{0.88}Si_{0.12}$	5.6452	+0.0052	-0.2585	21.52
$GaP_{0.50}As_{0.50}Ge_3$	$Ge_{0.88}Si_{0.12}$	5.6186	+0.0030	+0.2776	49.98
$GaP_{0.60}As_{0.40}Ge_3$	$Ge_{0.83}Si_{0.17}$	5.6098	+0.0023	+0.3245	8.33
$GaP_{0.75}As_{0.25}Ge_3$	$Ge_{0.83}Si_{0.17}$	5.5970	+0.0018	+0.5073	4.05
$GaP_{0.90}As_{0.10}Ge_3$	$Ge_{0.83}Si_{0.17}$	5.5849	+0.0017	+0.6643	4.43
Lattice matched films					
$GaP_{0.20}As_{0.80}Ge_3$	$Ge_{0.93}Si_{0.07}$	5.6468	+0.0068	-0.0899	106.28
$GaP_{0.30}As_{0.70}Ge_3$	$Ge_{0.88}Si_{0.12}$	5.6368	+0.0050	-0.0284	79.45
$GaP_{0.35}As_{0.65}Ge_3$	$Ge_{0.88}Si_{0.12}$	5.6317	+0.0039	-0.0727	52.09
$GaP_{0.45}As_{0.55}Ge_3$	$Ge_{0.83}Si_{0.17}$	5.6233	+0.0036	+0.0364	82.83
$GaP_{0.85}As_{0.15}Ge_3$	$Ge_{0.70}Si_{0.30}$	5.5886	+0.0014	+0.0179	74.40
$GaPGe_{3.3}$	$Ge_{0.70}Si_{0.30}$	5.5889	+0.0000	+0.0389	100

metastable epilayers on Group IV platforms. Another major advantage is that synthetic procedures for growing $Ge_{1-x}Si_x$ alloys on Si are well established, enabling straightforward integration of low defectivity crystals with flat surfaces and large thickness approaching bulk values, as needed for the fabrication of viable buffer layers. The foregoing $Ge_{1-x}Si_x$ samples were grown in a gas-source molecular epitaxy chamber via reactions of gaseous Ge_4H_{10} and Si_4H_{10} at 360-400 °C. It was found that increasing the temperature in this range produced materials at enhanced growth rates and with better crystallinity. The films were subjected to an *in situ* annealing step to reduce residual strains and improve crystal orientation and alignment with the wafer. Analysis of the resultant samples by high-resolution X-ray diffraction (HR-XRD) showed that the full width at half maximum (FWHM) of the (004) reflection was reduced after annealing to values ranging from 0.05° to 0.2° for $x = 0.075$ to $x = 0.30$, respectively. Rutherford backscattering (RBS) showed that the layers ranged in thickness from 0.5 μm to 2 μm and exhibited Si/Ge concentrations similar to those determined by XRD. AFM revealed a route mean square (RMS) roughness of ~ 0.5 nm, indicating planar surfaces suitable for subsequent epitaxy.

A separate molecular epitaxy chamber was employed to perform depositions of the $Ga(As_{1-x}P_x)Ge_3$ epilayers under ultra-low pressures in the 10^{-6} Torr range.. Substrates were cut from the four-inch wafers into 1.0 x 1.5 cm pieces to fit on the sample stage on the reactor. They were chemically prepared for subsequent epitaxy by etching the native oxide from the surface using a 5% HF solution. The substrates were then loaded into the UHV chamber and heated under vacuum to 550 °C for several hours to desorb the

hydrogen passivation and remove remaining impurities until the chamber pressure was restored to levels below 1 x 10^{-8} Torr. After degassing, the temperature was set to 450 °C to commence deposition of all samples. High precision needle valves were used to deliver the flux of the $[D_2GaN(CH_3)_2]_2$ reactant and the $P(GeH_3)_3/As(GeH_3)_3$ co-reactants into the chamber. Separate inlet nozzles directed the molecular flow onto the sample stage to prevent gas phase interactions of the compounds before reaching the substrate surface. The pressure ratio of $[D_2GaN(CH_3)_2]_2$ to the $P/As(GeH_3)_3$ mixtures was adjusted to be approximately 1:1, leading to a total final pressure of ~ 4.0 x 10^{-6} Torr inside the reactor.

Using this approach two sets of samples were produced and the results are summarized in Table 5. The samples include proof-of-concept prototypes grown at the initial stages of the work to explore feasibility of the approach, followed by a series of lattice-matched analogues to improve crystallinity and eliminate residual strains and misfit defects. The initial samples, listed in the upper segment of Table 5, were grown on $Ge_{0.88}Si_{0.12}$ and $Ge_{0.83}Si_{0.17}$ buffer layers. This effort aimed to establish the growth parameters including flux ratios, gas flows, and temperature/pressure protocols needed to tune the $Ga(As_{1-x}P_x)Ge_3$ compositions across the target range reliably. All samples were grown at 450 °C with an average rate of 13 nm per minute. Alloys with higher As contents $x < 0.5$ were grown on $Ge_{0.88}Si_{0.12}$ while alloys with higher P content $x > 0.5$ were grown on $Ge_{0.83}Si_{0.17}$. In both cases the buffers were selected to be slightly mismatched relative to the epilayers, allowing a clear separation of the XRD peaks between the two materials in a given sample. This enabled an unambiguous measurement of the lattice constants and provided a rough estimate of the film composition using

XRD. However, the misfit strains were found to restrict the maximum thickness that could be achieved and in some cases resulted in inferior quality defected films, limiting the ability to explore the full potential of the innate properties of the crystals. To circumvent the possible deleterious strain effects in these materials the development of relaxed, bulk-like layers on lattice matched $Ge_{1-x}Si_x$ templates with x = 0.07 - 0.30 was pursued. These samples are listed in the lower half of Table 5. From a crystal growth perspective, this task also provides the opportunity to demonstrate the full benefits of the $Ge_{1-x}Si_x$ buffers for systematic integration of III-V based structures of Si wafers and explore how the bonding arrangements delivered by assembly of intact III-V-IV building blocks conform to the interface microstructure. The samples in this case were grown at nearly identical temperature, pressure, and precursor flux conditions as the mismatched counterparts.

Ge-rich $(GaP)_yGe_{5-2y}$ films with tunable Ge contents up to 90% were also grown in this study by increasing the partial pressure of the $P(GeH_3)_3$ compound from 1:1 to 4:1 relative to $[D_2GaN(CH_3)_2]_2$. This action resulted in an overall increase of the final deposition pressures inside the chamber from 4.0×10^{-6} Torr to 1.0×10^{-5} Torr, respectively. Under these conditions monocrystalline films with thicknesses of 140 – 650 nm were produced at growth rates varying from 17 – 32 nm/min depending on the relative amount of $P(GeH_3)_3$ in a given experiment. Characterizations by RBS and XRD, described below, reveal that these materials are single-phase alloys exhibiting tunable lattice constants as a function of Ge content. This approach provides access to dilute diamond-like solid solutions incorporating highly dispersed Ga-P pairs within the parent

Ge framework. New functionalities are expected by altering the electronic structure while preserving the random diamond lattice of the resultant crystal.

Growth of $Al(P_{1-x}Sb_x)Si_3$ alloys was achieved via similar means. In this case silicon containing Group V compounds, $Sb(SiH_3)_3$ and $P(SiH_3)_3$ were used, and $Al(BH_4)_3$ as a chemical source of Al. In later experiments, an Al Knudsen cell was used in place of $Al(BH_4)_3$. A Si buffer layer was grown on the substrate using a 10% mixture of Si_4H_{10} diluted with H_2. All $Al(P_{1-x}Sb_x)Si_3$ alloys were grown at $8.0x10^{-6}$ Torr at 600 °C. In order to control the film composition, the ratio of P:Sb in the mixture was adjusted stoichiometrically. The growth was begun through the introduction of Al atoms from a solid Al source, and the flow of $P/Sb(SiH_3)_3$ mixtures was introduced through a high precision needle valve. A constant temperature and pressure was maintained throughout the deposition process. In experiments utilizing $Al(BH_4)_3$ as an Al source, single mixtures

Table 6: List of selected $Al(P_{1-x}Sb_x)Si_3$ films

Sample Number	Substrate	Composition	Al Source	Thickness (nm)	a_0 (Å)
P-rich samples					
AlPSbSi 21	Si(100)	$AlP_{0.99}Sb_{0.01}Si_3$	Al cell	160	5.4413
AlPSbSi 8	Si(100)	$AlP_{0.95}Sb_{0.05}Si_3$	$Al(BH_4)_3$	120	5.4444
AlPSbSi 6	Si(100)	$AlP_{0.92}Sb_{0.08}Si_3$	$Al(BH_4)_3$	650	5.4721
AlPSbSi 18	Si(100)	$AlP_{0.91}Sb_{0.09}Si_3$	Al cell	145	5.4731
AlPSbSi 24	Si(100)	$AlP_{0.89}Sb_{0.11}Si_3$	Al cell	80	5.4844
AlPSbSi 25	Si(100)	$AlP_{0.88}Sb_{0.12}Si_3$	Al cell	140	5.4797
AlPSbSi 22	Si(100)	$AlP_{0.85}Sb_{0.15}Si_3$	Al cell	175	5.4870
Sb-rich samples					
AlPSbSi_Ge 10	Ge/Si(100)	$AlP_{0.10}Sb_{0.90}Si_3$	Al cell	155	N/A
AlSbSi 10	Ge/Si(100)	$AlSbSi_{2.5}$	Al cell	360	N/A
AlPSbSi_Ge 5	Ge/Si(100)	$AlSbSi_3$	Al cell	80	N/A

containing $Al(BH_4)_3$ as well as $P/Sb(SiH_3)_3$ were made in a 1:2 molar ratio with the Group V components in excess. The growth rate varied from 4-8 nm/min producing film thicknesses between 80 and 160 nm. A range of $Al(P_{1-x}Sb_x)Si_3$ compositions is provided in Table 6.

5.3 Results and Discussion

5.3.1 $Ga(As_{1-x}P_x)Ge_3$ Composition and Structural Analysis

RBS was used to determine the absolute elemental compositions of the synthesized $Ga(As_{1-x}P_x)Ge_3$ alloys. In the low P content films ($x \sim 0.01$-0.05) the Ga, Ge, and As signals in the RBS spectra tend to overlap and blend together into a single peak due to the close proximity of atomic numbers. This makes it impossible to determine the compositions solely from RBS. However, as the P content increases the As signal intensity decreases, producing a clear separation of the Ga peak from the combined As/Ge contributions. One can then obtain accurate concentrations by assuming perfect III/V compensation, so that the film compositions are given by $Ga(As_{1-x}P_x)_yGe_{5-y}$. Figure 38 shows the 2.0 MeV RBS spectra for a representative film grown on a $Ge_{0.70}Si_{0.30}$ buffer. Although the spectrum features a distinct Ge signal for the buffer, its counterpart in the epilayer significantly overlaps with the corresponding As signal. However, the distinct P and Ga features in the spectra constrain the As content in a way that allows all concentrations to be determined by using standard RBS modeling

packages. A fit is shown by the red trace in Figure 38, and the agreement with the data is excellent. The sample compositions obtained by this method were then corroborated using the 3.7 MeV spectra (inset). The latter provide a complete separation of the P signal from the Ge background, making the determination of the P concentration unambiguous even without fitting. It was found that y = 1 for all films that contain both As and P, strongly supporting the suggested growth mechanism via Ga-P-Ge_3 and Ga-As-Ge_3 tetrahedra. It was also found that the films span the entire range of concentrations from x = 0 ($GaAsGe_3$) to x = 1 ($GaPGe_3$), although in the latter case it was found that y = 0.94, so that the Ge concentration is slightly above the $GaPGe_3$ stoichiometry.

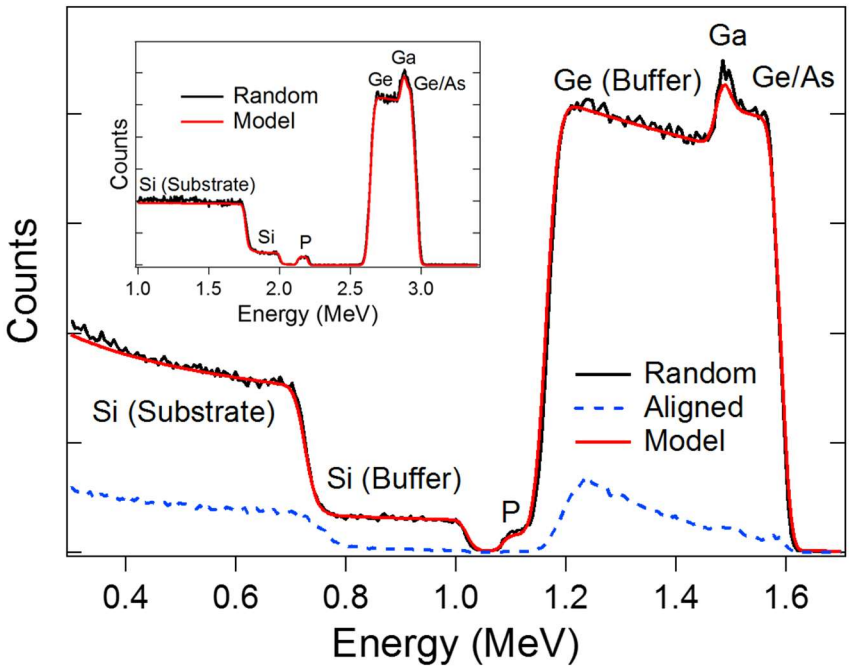

Figure 38: 2.0 MeV RBS spectrum of $GaAs_{0.15}P_{0.85}Ge_3/Ge_{0.70}Si_{0.30}$ sample. Red trace is a composition model overlaid onto the random spectrum (black trace). The blue dotted line corresponds to the channeled spectrum indicating a high level of epitaxial registry along [100]. Inset shows a 3.7 MeV spectrum of the same sample illustrating a fully resolved P peak.

The RBS model yields the thicknesses of all samples, which are found to lie in the 160 – 300 nm range depending on the deposition times. These values were further

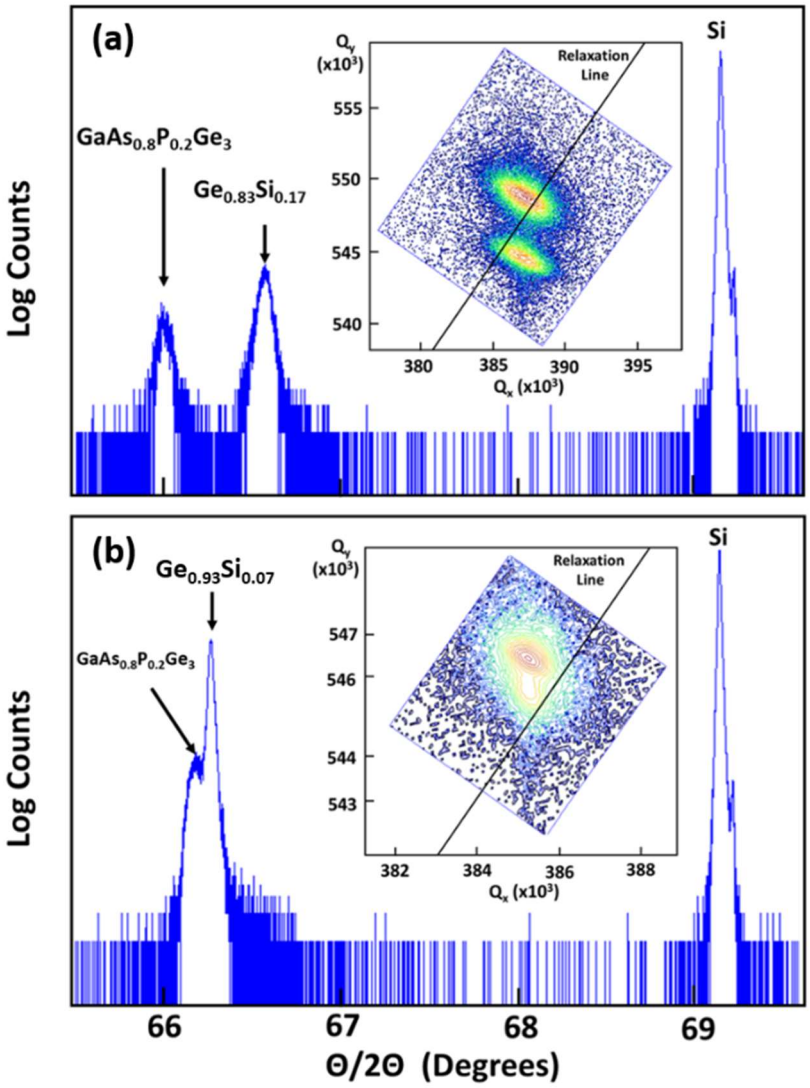

Figure 39: HR-XRD on-axis plots and (224) reciprocal space maps of $GaAs_{0.8}P_{0.2}Ge_3$ epilayer grown on $Ge_{0.83}Si_{0.17}$ and $Ge_{0.93}Si_{0.07}$ buffer layers. In panel (a) the epilayer is fully coherent and compressively strained on the mis-matched buffer layer. In panel (b) the two materials are nearly lattice matched as evidenced by the close proximity of the XRD peaks. This leads to better quality crystals as demonstrated by significant narrowing of the XRD signatures in the spectra.

corroborated by spectroscopic ellipsometry. In addition, the RBS analysis provided insights into the sample crystallinity, phase purity and epitaxial alignment. Figure 38 compares the channeled 2.0 MeV spectrum (dotted line) with the random analogue (black line) showing a precipitous drop in the signal intensity across the buffer and epilayer peaks. This observation indicates that the material is epitaxial and perfectly aligned along the [100] direction of the underlying GeSi/Si wafer. The uniform channeling profile across the film provides strong indication that the epilayer is a single-phase alloy and the constituent elements occupy substitutional sites within the same diamond lattice.

The RBS composition determinations are dramatically confirmed by XRD studies of the lattice parameter. Figure 39 shows high resolution XRD spectra of a $Ga(As_{0.80}P_{0.20})Ge_3$ film grown on a $Ge_{0.83}Si_{0.17}$ buffer. The θ-2θ plots and off-axis reciprocal space maps both show distinct (004) and (224) peaks for the buffer and the epilayer, indicating monocrystalline alloys with diamond like structures. The (224) peaks in the inset are vertically aligned and exhibit a common Q_x value. This indicates that the buffer and epilayer are pseudomorphically strained and possess virtually equal in-plane lattice parameters $a_{\text{epilayer}} = 5.6306$ Å and $a_{\text{buffer}} = 5.6326$ Å. The corresponding vertical parameters of the two materials are found to be $c = 5.6570$ Å and $c = 5.6133$ Å, respectively. From these data one can use linear elasticity theory to compute the relaxed cubic lattice parameter as

$$a_0 = \frac{c + Ka}{1 + K} \qquad (2)$$

where $K = 2C_{12}/C_{11}$ is a ratio of elastic moduli. These ratios are quite similar for zincblende and diamond-structure semiconductors, and therefore one can approximate the unknown alloy value as a linear interpolation

$$K^{\text{alloy}} = \frac{5-2y}{5}K^{\text{Ge}} + \frac{2(1-x)y}{5}K^{\text{GaAs}} + \frac{2xy}{5}K^{\text{GaP}} \qquad (3)$$

Here $K^{\text{Ge}} = 0.750$,[156] $K^{\text{GaAs}} = 0.905$,[157] and $K^{\text{GaP}} = 0.905$ were used.[158] For the alloy in Figure 39(a), $a_0 = 5.645$ Å. Results for all samples are shown in Figure 40 and it can be seen that the lattice parameters are very strongly correlated with the phosphorus fraction *x*, which implies that the III-V:IV fraction must be approximately constant, exactly as concluded from the RBS fits, which indicate y = 1. The relaxed lattice parameter can be used to estimate the mismatch strain with the buffer layer as $\varepsilon_{||} = (a_{\text{epilayer}}-a_0)/a_0$. Note that residual *tensile* strains up to 0.09% appear in some of the $Ge_{1-x}Si_x$ buffers. These arise during the cooling cycle as a result of the thermal expansion differential between the film and the Si wafer. Accordingly, it was observed that there are slightly different in-plane parameters for the same *x* value in some buffers, as illustrated for the $Ge_{0.88}Si_{0.12}$ case in Table 5. This suggests that strain can be used as an additional degree of freedom for tuning the buffer layer dimensions in the $Ge_{1-x}Si_x$ on Si system. Note also that for the As-free compounds, the $(GaP)_{0.94}Ge_{3.12}$ film (denoted as $GaPGe_{3.3}$ in Table 5) is in nearly perfect lattice match with the $Ge_{0.70}Si_{0.30}$ buffer layer. However, efforts to produce the exact stoichiometry $GaPGe_3$ using a lattice-matched buffer layer $Ge_{0.66}Si_{0.34}$ and widely varied reaction conditions were not successful, as discussed later.

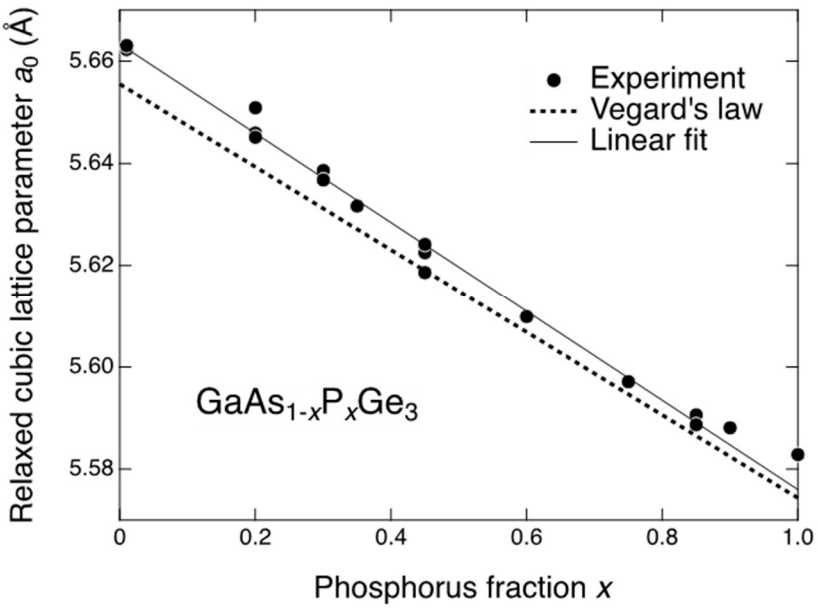

Figure 40: Relaxed cubic lattice parameter a_0 for $Ga(As_{1-x}P_x)_yGe_{5-2y}$ alloys. The dotted line represents Vegard's law using a linear interpolation of lattice parameters between Ge, GaAs, and GaP. A small systematic positive departure from Vegard's Law is apparent from the data. The departure becomes larger near the GaAs end in qualitative agreement with theoretical predictions. The linear fit uses only the samples for which y = 1.

The dotted line in Figure 40 shows the lattice parameter interpolated between Ge, GaAs, and GaP as in Equation (3), which is denoted as "Vegard's law". This simple interpolation is in very good agreement with the data, confirming that the P/As ratio is varied over its entire range. The residual deviation from Vegard's law is positive and seems to grow toward the $GaAsGe_3$ end. To see if this result can be predicted theoretically, density functional theory (DFT) *ab initio* calculations were carried out using the Quantum ESPRESSO (QE) package.[159] The generalized gradient approximation (GGA) optimized for solids (PBEsol) was applied in this case along with ultrasoft

pseudopotentials.[160] The structural parameters were optimized until the atomic forces and stresses were reduced below 2.0×10^{-3} eV/Å and 1.0×10^{-4} eV/Å^3, respectively.

Figure 41(a) and (d) show models of the fully relaxed structures with 10-atom unit cell description in which the GaAs and GaP units are orientationally aligned to form the

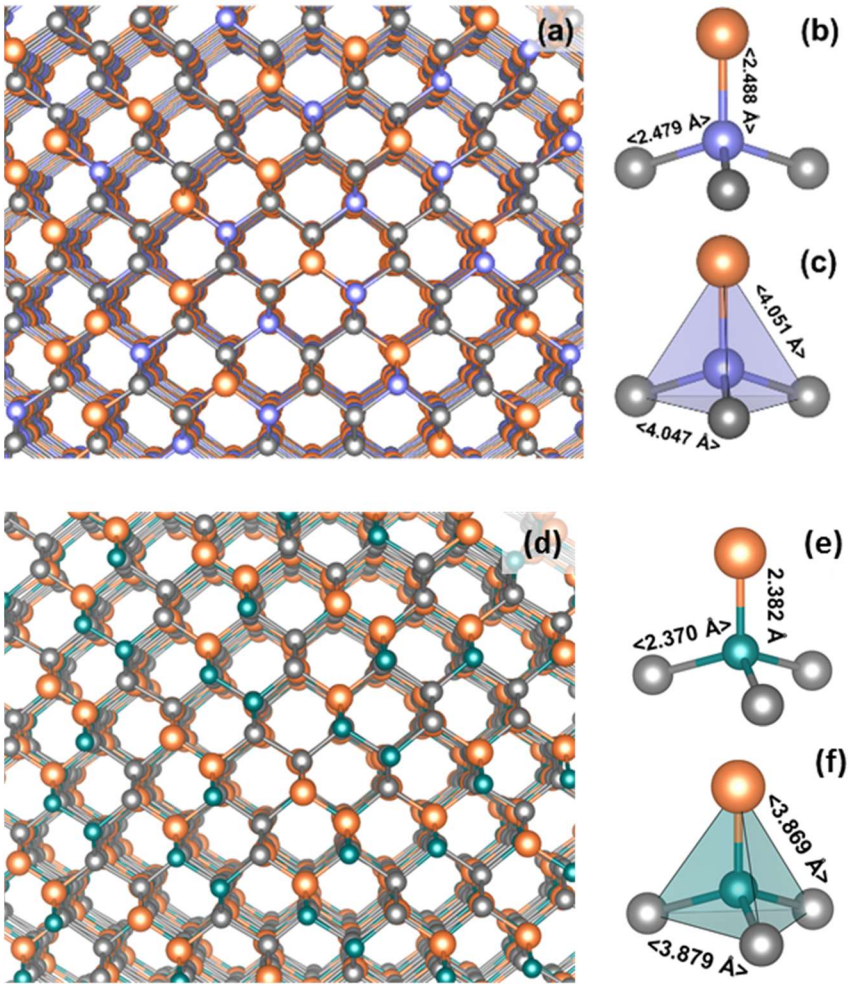

Figure 41: Structural models of $GaAsGe_3$ (a) and $GaPGe_3$ (d) in [110] projection showing the dimers or "dumbbells" of the diamond structure. (b and e) typical tetrahedral unit of the two compounds extracted from the calculated structure showing the average bond lengths. (c and f) Polyhedral representation of the building blocks showing the apical and basal edge lengths in each case.

ground state ordered phase. The figure illustrates the [110] equivalent direction featuring the "dumbbell" pattern of the average diamond lattice. For $GaAsGe_3$, Figure 41(a) shows no visible distortions from normal tetrahedral geometry due to the close similarity of Ga-As and Ge-Ge bond lengths. Correspondingly, a relatively regular bonding arrangement is also observed for $GaPGe_3$ in Figure 41(d) in spite of the smaller Ga-P bond length relative to Ge-Ge.

The uniformity of the $GaAsGe_3$ structure is further demonstrated in Figure 41(b) and 41(c) which show representations of the Ga-As-Ge_3 tetrahedral unit extracted from the ground-state structure of the material. The difference between the Ga-As (2.488 Å) and As-Ge (2.479 ± 0.001 Å) bond lengths shown in the models are small, as expected. This leads to the creation of a near regular tetrahedron exhibiting virtually identical apical and basal edges of 4.051 ± 0.018 Å and 4.047 ± 0.069 Å, respectively. Figure 41(e) and 41(f) show the tetrahedral units of the $GaPGe_3$ phase illustrating very similar Ga-P (2.382 Å) and Ge-P (2.370 ± 0.002Å) bond lengths, as expected. This also leads to the formation of a regular tetrahedron as evidenced by the close similarly of the apical (3.869 ± 0.026Å) and basal (3.879 ± 0.087 Å) edges in Figure 41(f). However, in this case a slight tilt of the tetrahedral units to accommodate the larger Ge-Ge bonds was observed. This is manifested by a minor displacement of the Ga atom positions down each crystal column, giving rise to a zigzag sequence (rather than a straight-line progression) as illustrated in Figure 41(f).

The ground state structure for both compounds is found to be monoclinic with C1c1 symmetry. The cell parameters for $GaAsGe_3$ are $a = b = 8.9898$ Å, $c = 5.7063$ Å, α

= β = 90°, and γ = 90.04° indicating near tetragonal geometry. The cubic equivalent of this monoclinic lattice is calculated to be a_0 = 5.6925 Å. Using the same theoretical framework, the lattice constants for the GaAs and Ge end members were also calculated to be a_0 = 5.6720 Å and a_0 = 5.6797 Å, respectively, so that the predicted Vegard average for $GaAsGe_3$ is a_0 =5.6766 Å. Similarly, the lattice constants of the $GaPGe_3$ monoclinic cell are calculated to be $a = b$ = 8.8169 Å, c = 5.608 Å, α = β = 90°, and γ = 90.08, which correspond to a cubic analogue of a_0 = 5.5869 Å. On the other hand, for GaP theory predicts a_0 = 5.5060 Å, so that the theoretical Vegard average for $GaPGe_3$ is a_0 = 5.6102 Å. In other words, theory predicts a positive (0.3%) deviation from Vegard's law near the $GaAsGe_3$ end, and a negative (-0.4%) deviation near the $GaPGe_3$ end. This is qualitatively in agreement with experiment, which shows a positive deviation (0.14%) near the $GaAsGe_3$ end and a vanishing deviation (0.03%) near the $GaPGe_3$ end. Quantitatively, however, the deviations do not agree. This may be partially due to the adoption of the C1c1 unit cell, which is just one of the many possible unit cell choices consistent with a lattice of III-V-IV_3 tetrahedra.

5.3.2 $Al(P_{1-x}Sb_x)Si_3$ Composition and Structural Analysis

High-resolution X-ray diffraction (HR-XRD) was used to probe the crystallinity of the resultant $Al(P_{1-x}Sb_x)Si_3$ films. The main panel of Figure 48 shows a (004) reflection of an $AlP_{0.89}Sb_{0.11}Si_3$ film overlaid with a pure $AlPSi_3$ film. The $AlP_{0.89}Sb_{0.11}Si_3$ peak is shifted significantly from that of $AlPSi_3$ due to the contribution of the large AlSb

lattice constant (6.1 Å). The single peak feature seen in the spectra is characteristic of a single-phase monocrystalline material. In this case, $AlP_{0.89}Sb_{0.11}Si_3$ was found to have a *c* lattice parameter of 5.5245 Å.

A (224) reciprocal space map (RSM) of the same material was collected, as can be seen in the inset of Figure 42. Again, a single peak feature can be seen for $AlP_{0.89}Sb_{0.11}Si_3$. The peak lies directly below the Si substrate along the pseudomorphic line meaning the epilayer is fully strained to Si. The film was calculated to have a relaxed lattice parameter of 5.4824 Å and a compressive strain of -0.92%. A complimentary -(224) RSM yielded the same peak position meaning the *a* and *b* lattice parameters are identical and the material is tetragonally distorted due to the strain. A (002) reflection

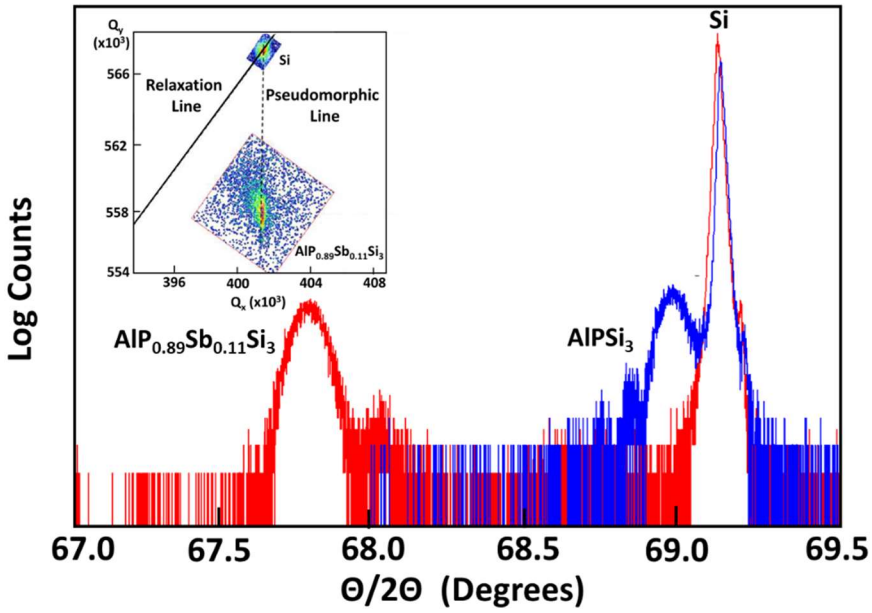

Figure 42: Main panel – (004) HR-XRD spectra on $AlP_{0.89}Sb_{0.11}Si_3$ on Si overlaid with $AlPSi_3$. A significant shift to lower angles is clear due to the presence of Al-Sb pairs in the film. Inset – a (224) RSM of the same $AlP_{0.89}Sb_{0.11}Si_3$ film, here the pseudomorphic nature of the film can be seen given its peak position directly below Si along the pseudomorphic line.

(not shown) yielded no diffraction, eliminating the possibility of a phase-segregated zincblende material.

Rutherford backscattering (RBS) characterization of the alloy, which is displayed in the main panel of Figure 43, shows distinct Al, P, and Sb peaks; an edge can be seen which corresponds to the Si contribution from the epilayer. Each peak is symmetric indicating a uniform composition throughout the film. The spectra was modeled using the program XRump to give the composition $AlP_{0.89}Sb_{0.11}Si_3$ and a thickness of 80 nm. The channeled spectra, shown as a blue dashed trace in Figure 43, has a significantly

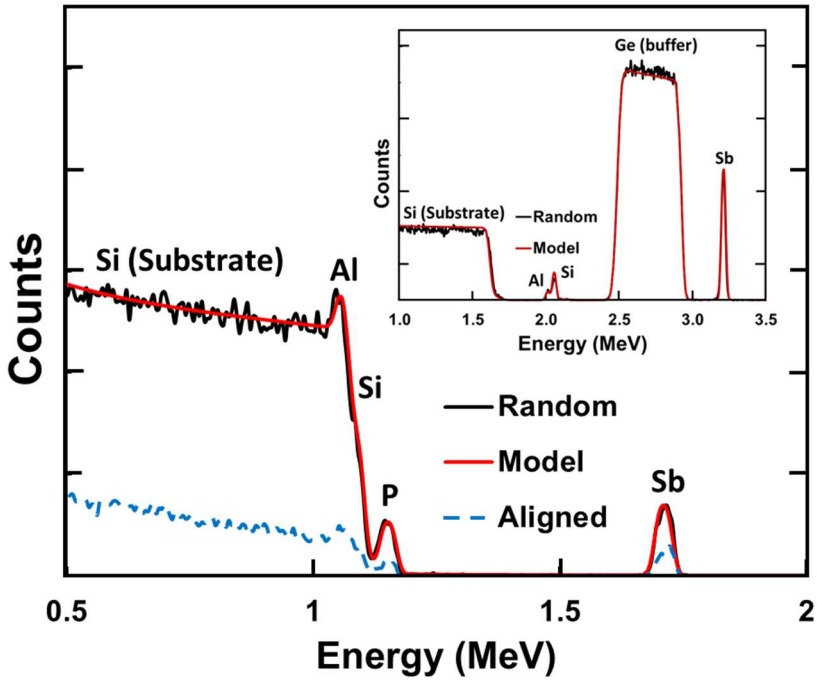

Figure 43: Main panel - 2.0 MeV RBS spectra of $AlP_{0.89}Sb_{0.11}Si_3$, the black trace is collected at a random angle, and the red trace is a computational model of the material. Distinct peaks can be seen for Al, P, and Sb along with the edge for the Si in the epilayer. The blue dashed trace is a channeled spectrum of the film. Inset - 3.7 MeV RBS spectra of $AlPSbSi_3$, again the black and red traces are random computational models respectively. Distinct peaks can be seen for Al, Si, and Sb in the epilayer along with a large peak from the Ge buffer.

decreased signal compared with the overlaid random spectra (shown in black). This decreased intensity is indicative of an epitaxially aligned film, which confirms the monocrystalline pseudomorphic nature of the material as observed through HR-XRD. The inset of Figure 43 shows the RBS spectrum obtained from an $AlSbSi_3$ film with a thickness of 80 nm, this alloy was grown on a Ge buffer that can also be seen in the spectra. Distinct peaks are visible for Al, Si, and Sb in the epilayer, and each peak is symmetric indicating that composition is uniform throughout the film. Thus far, no single-crystal alloys have been grown for materials $x > 0.15$, and thus no channeling or HR-XRD data was collected.

5.3.3 Microstructure Analysis

The structural properties of the samples were further characterized using high resolution cross sectional electron microscopy (XTEM), which confirmed the formation of smooth, uniform and crystalline epilayers with thicknesses in agreement with those determined by RBS and ellipsometry. Figure 44 shows XTEM images of a $Ga(As_{0.80}P_{0.20})Ge_3$ film grown pseudomorphically on a mismatched $Ge_{0.88}Si_{0.12}$ buffer layer. The data were collected using a JEOL ARM200F aberration-corrected microscope and include the low magnification Z-contrast view of the entire epilayer thickness (300 nm) shown in the top panel. The uniform contrast throughout the crystal is symptomatic of a homogeneous crystal devoid of GaP precipitates, corroborating the single-phase character established by XRD and RBS. The bottom panel is a high magnification image,

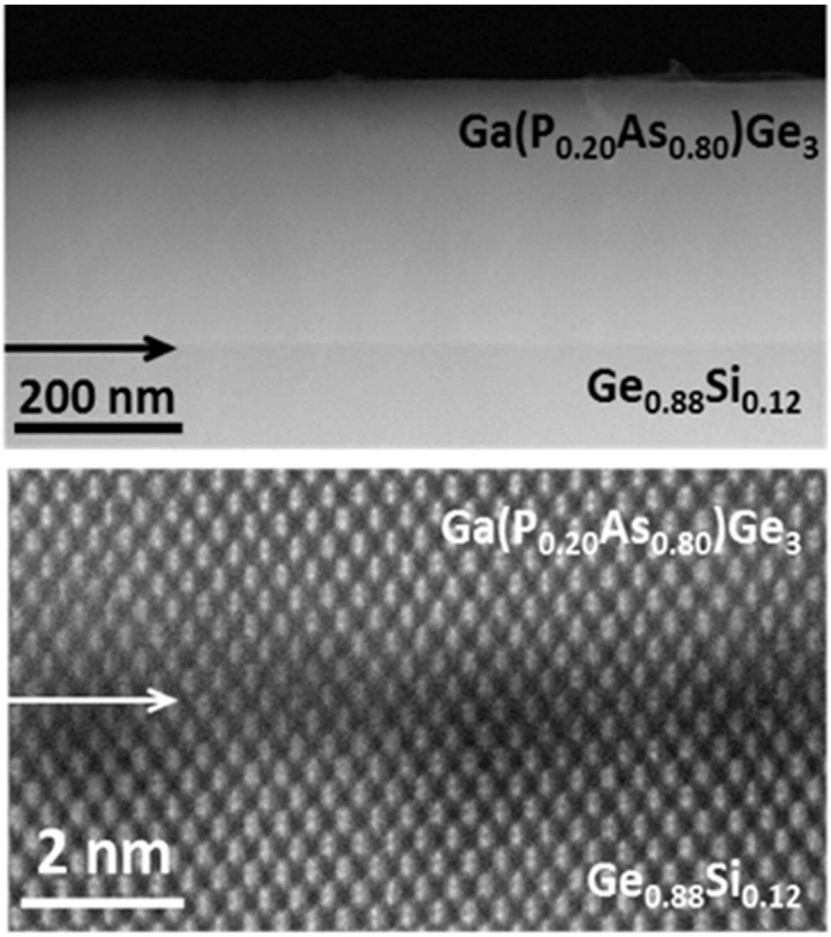

Figure 44: XTEM images of $Ga(As_{0.80}P_{0.20})Ge_3$ grown on a $Ge_{0.88}Si_{0.12}$ buffer. Top panel is a Z-contrast image showing the entire epilayer with thickness of 300 nm. Bottom panel is a high resolution image of the interface region showing a uniform and fully epitaxial heterojunction between the buffer and the epilayer marked by arrow.

featuring an atomic resolution view of the interface marked by an arrow. This is taken in [110] projection and contains elongated bright spots associated with pairs of atoms or "dumbbells". The complete alignment of the atomic rows seen along [111] and the absence of relaxation defects corroborate the XRD data that the crystal is pseudomorphic. Furthermore, the seamless bonding at the interface is consistent with the chemical compatibility between the III-V-IV epilayer and the Group IV buffer.

Figure 45 shows XTEM images of the same $Ga(As_{0.80}\ P_{0.20})Ge_3$ alloy grown in this case strain-free on a lattice matched $Ge_{0.93}Si_{0.07}$ buffer layer. The data in Figure 45 were collected on a FEI Titan 80-300 electron microscope operated at 300 kV. Panel 43(a) is a diffraction-contrast micrograph illustrating an enlarged view of the film, including the interface region marked by an arrow. Note that the surface is flat and the contrast is uniform, demonstrating the lack of phase separation or compositional variations, which typically appear in the form of vertical striations that dominate the background

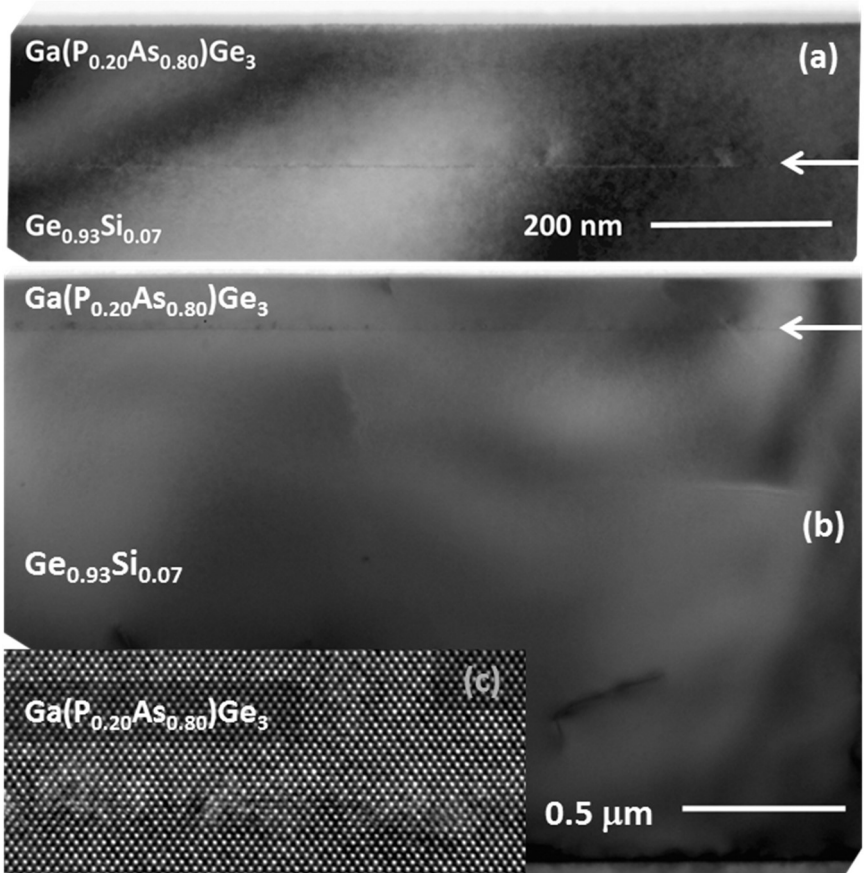

Figure 45: XTEM data of a $Ga(As_{0.80}\ P_{0.20})Ge_3$ alloy grown lattice matched on a $Ge_{0.93}Si_{0.07}$ buffer layer. Panel (a) is a partial enlarged view of the film illustrating an extremely uniform and featureless epilayer. Panel (b) is a full view of the film highlighting excellent crystallinity throughout. Panel (c) is a high-resolution image of the interface.

microstructure. Furthermore, the material is free of threading defects and stacking dislocations within the field view. Collectively the smooth and uniform texture provides strong evidence for the existence of a homogenous single-phase crystal.

Figure 45(b) shows the full film thickness providing a comprehensive view of the entire sample spanning several microns in the lateral direction. This makes it possible to observe the long-range order and gain a realistic assessment of the defect densities. Again, a uniform and featureless contrast is seen throughout, highlighting the paucity of defects and morphological flaws. Particularly striking is the structural perfection of the 1.6 μm-thick buffer layer, likely due to the low-temperature deposition of highly reactive precursors that readily combine on the Si wafer growth surface to yield $Ge_{1-x}Si_x$ films. The lattice mismatch of the films with Si(100) is accommodated with interface defects whose dislocation cores do not penetrate through the layer, as is evident in the figure. This process provides templates with bulk-like thicknesses, relaxed microstructures, and flat surfaces that promote epitaxy driven synthesis of single phase $Ga(As_{1-x}P_x)Ge_3$ alloys. Finally, panel 45(c) shows a high-resolution image of the interface illustrating a smooth transition between the buffer and the epilayer, as manifested by the observation of one-to-one alignment of the lattice planes along [111], with no sign of dislocations. The TEM results in general illustrate the formation of materials possessing not only phase homogeneity and compositional uniformity but also the desired morphological and structural perfection, making them possible candidates as either passive or active layers for device applications from a crystal quality perspective.

As indicated above, efforts to prepare the previously unknown $GaPGe_3$ (60% Ge) phase by reactions of $P(GeH_3)_3$ with $[D_2GaN(CH_3)_2]_2$ consistently yielded slightly Ge-rich samples with composition $y = 0.94$, which can equivalently be described as $GaPGe_{3.3}$. Detailed structural analysis of this sample was performed by XTEM and representative images are presented in Figure 46. The top panel reveals the presence of a crystalline layer exhibiting a uniform contrast except for several isolated regions that appear to show patches of thin columnar features aligned along the growth direction. These extend a short distance through the layer and may be related to misalignment in crystal orientation

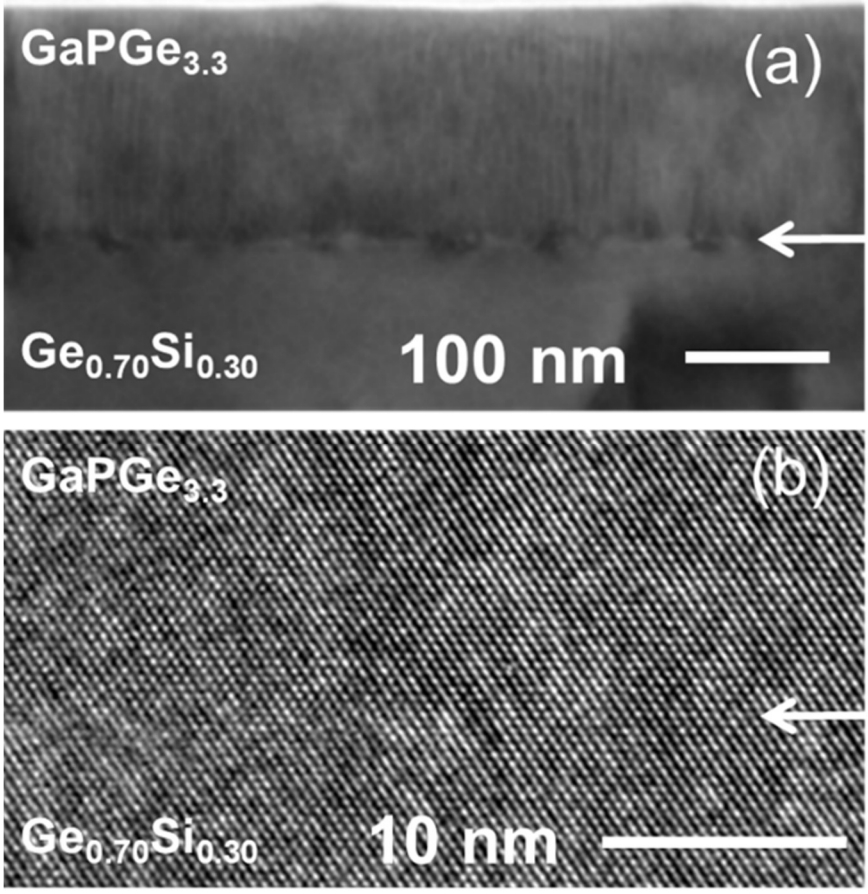

Figure 46: XTEM images of $GaPGe_{3.3}$ showing a full view of the epilayer in panel (a) and a high resolution of the interface region in panel (b). The white arrows mark the location of the interfaces.

or slight variations in composition at the nanoscale. This is not unexpected given the complexity of the deposition process that may in fact be susceptible to slight fluctuations in growth conditions under the low temperatures employed. Panel 46(b) is a high-resolution image of the interface showing defect-free epitaxy a testament to the lattice matching capability of the buffer layer.

XTEM was also used to examine the microstructure of the $Al(P_{1-x}Sb_x)Si_3$ alloys. Figure 47 – panel (a) shows the interface between $AlP_{0.88}Sb_{0.12}Si_3$ and the underlying Si(100) buffer. The interface is flat and devoid of defects within the field of view, and [111] lattice fringes are clearly visible propagating through interface indicating good epitaxial alignment between the layers. In panel (b) an atomic resolution micrograph of the same sample interface can be seen. There is clearly good commensuration between the two layers. The lack of defects at the interface is expected given the pseudomorphic nature of the $AlP_{0.88}Sb_{0.12}Si_3$ epilayer.

Clearly, oriented P-rich films are capable of being grown over a range of compositions, x = 0.01 – 0.15, directly onto Si(100) as monocrystalline layers. However, this is not the case of Sb-rich films grown under the same parameters. Figure 48 shows XTEM data collected under the same conditions described previously, but in this case the composition of the sample is $AlSbSi_3$. Panel (a) shows a low magnification micrograph of the full $AlSbSi_3$ layer, several crystal orientations can be seen with moiré patterns visible throughout the layer. The material is not oriented, which corroborates the lack of a peak in the HR-XRD spectra. A high magnification micrograph of the same sample can be

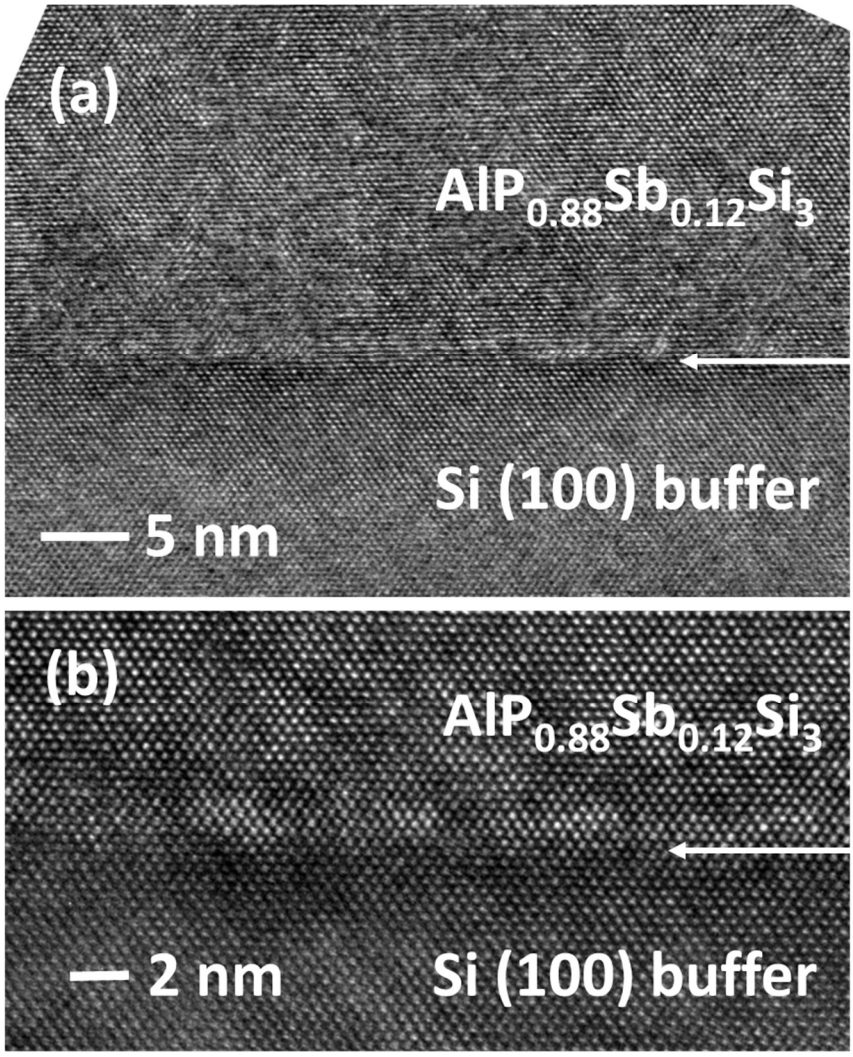

Figure 47: Panel (a) – Low magnification XTEM micrograph of $AlP_{0.88}Sb_{0.12}Si_3$ on Si, the interface is marked by a white arrow. A highly crystalline epilayer can be seen with no defects visible in the field of view. Panel (b) – Atomic resolution micrograph of the sample above. Here clear commensuration can be seen between the layers.

seen in Figure 48(b), the growth is clearly epitaxial, however, it is likely that defects introduced as the film relaxes result in the multiple orientations observed in Figure 48(a). In order to pursue $AlSbSi_3$ in detail, a substrate that more closely lattice matches the epilayer material needs to be used. Large lattice parameter III-V alloys such as GaSb are an option, but they are prohibitive due to their expense. A more judicious approach may

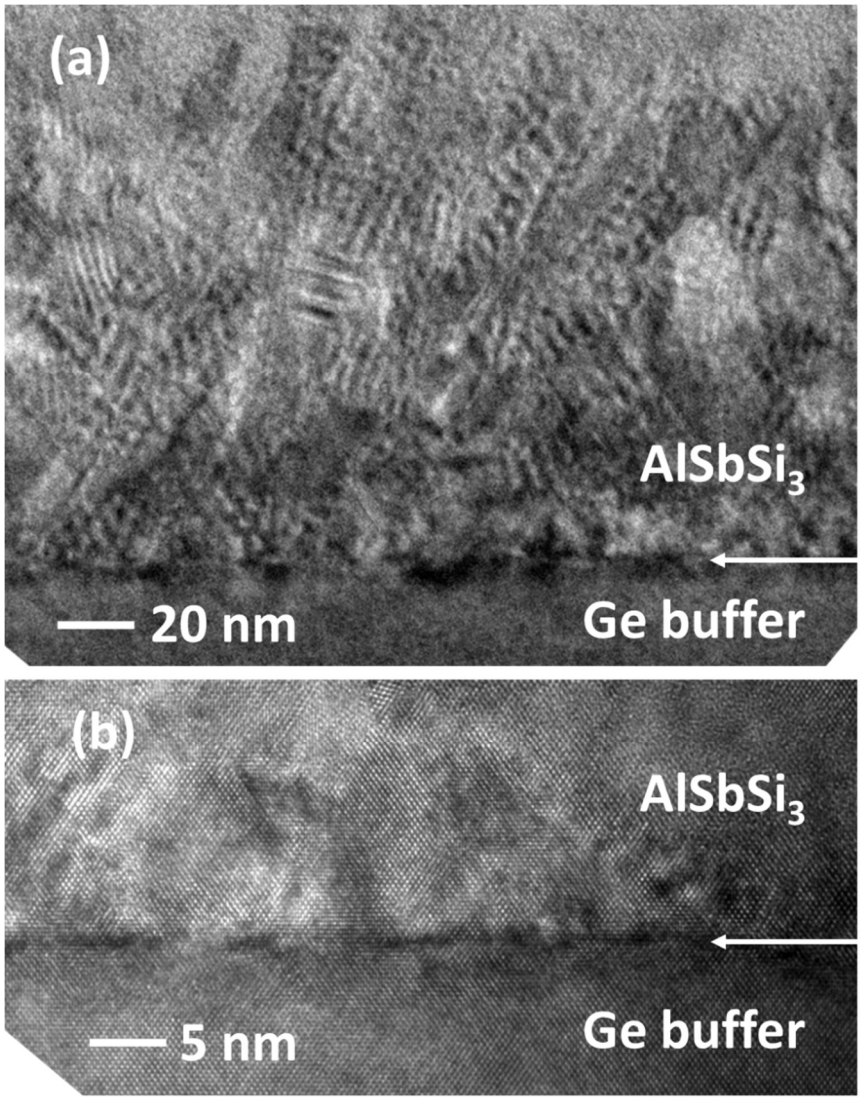

Figure 48: Panel (a) – Low-magnification XTEM micrograph of $AlSbSi_3$ on a Ge buffer, the interface is marked by a white arrow. Moiré patterns can be seen throughout the film indicating multiple lattice orientations. Panel (b) – High-resolution micrograph of the interface where epitaxial growth can be seen.

be to use relaxed $Ge_{1-y}Sn_y$ films as virtual substrates. The large lattice parameter of $Ge_{1-y}Sn_y$ would provide an inexpensive Group IV platform to accommodate $AlSbSi_3$ films; however, given the thermal instability of $Ge_{1-y}Sn_y$, an elegant approach to deposition would be required to integrate it with a material grown at 600 °C.

5.3.4 $Ga(As_{1-x}P_x)Ge_3$ Optical Properties

Raman scattering experiments were carried out at room temperature using 532 nm excitation to characterize the bonding properties. Typical spectra are shown in Figure 49. A main peak is seen near 285 cm^{-1} that corresponds to Ge-Ge vibrations[161] and a peak near 340 cm^{-1} that is assigned to Ga-P vibrations because it is close to the 356 cm^{-1} frequency at which the optical phonon density of states in zincblende GaP has a sharp peak.[162] In the As-containing sample, a clear shoulder is seen to the low-energy side of the main peak. This shoulder is assigned to Ga-As vibrations, which are very close in

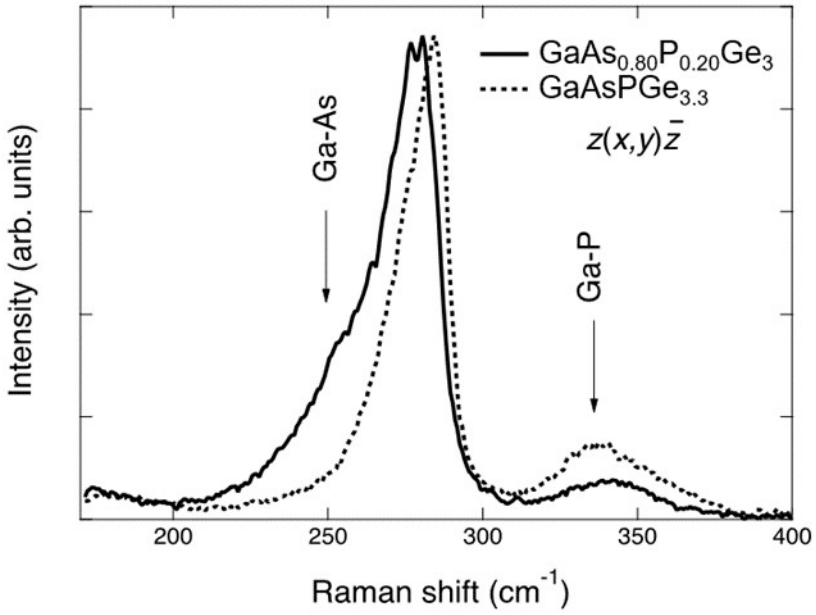

Figure 49: Room temperature Raman spectra of a $GaPGe_{3.3}$ and a $GaAs_{0.8}P_{0.2}Ge_3$ film using 532 nm illumination. The spectra are normalized so that the peak corresponding to Ge-Ge vibrations has the same maximum intensity. The scattering configuration is indicated using the Porto notation, with *x*, *y*, and *z* representing the cubic axes in the diamond structure. This configuration corresponds to allowed first-order Raman scattering in diamond and zincblende semiconductors.

frequency to Ge-Ge. Because of this proximity the vibrational modes are probably strongly mixed and do not have a pure Ge-Ge or Ga-As character.

Photoluminescence (PL) spectra were measured from $Ga(As_{1-x}P_x)Ge_3$ alloys using a 980 nm, 200 mW laser modulated at 190 Hz. A liquid nitrogen cooled InGaAs detector was employed to cover the relevant spectral range. The PL signal was only observed from As-rich samples with $x > 0.80$. Representative spectra of $Ga(P_{0.20}As_{0.80})Ge_3$ are shown in Figure 50, exhibiting two closely spaced peaks centered at 0.57 eV and 0.66 eV. Both peaks are strongly red-shifted relative to the direct transition energy expected from linear interpolation of the constituent end members Ge (E_0 = 0.80 eV), GaAs (E_0 = 1.4 eV), and GaP (E_0 = 2.3 eV). This trend is consistent with behavior observed for the $GaAsGe_3$ compound, whose PL spectrum also contains a similar two-peak profile with energies similar to $Ga(P_{0.20}As_{0.80})Ge_3$ indicating that the emission wavelength does not

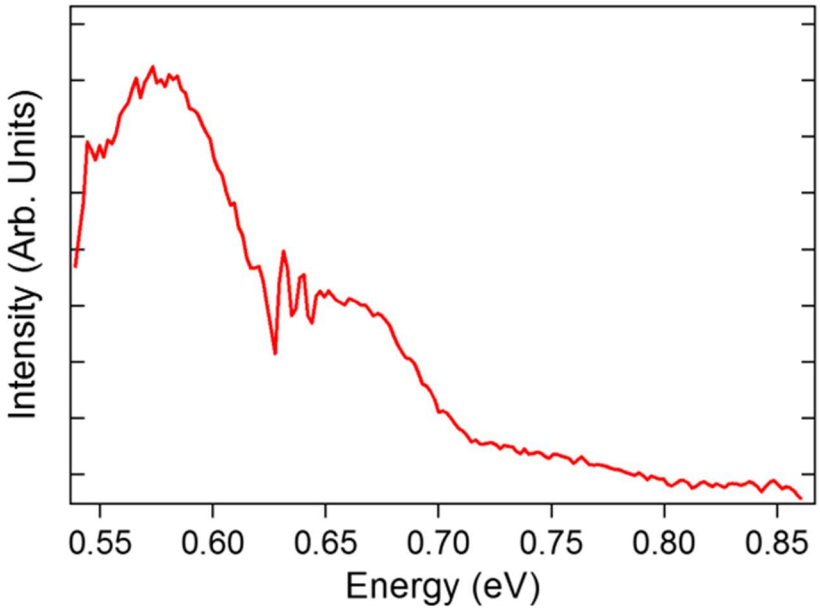

Figure 50: PL plots of $Ga(As_{0.8}P_{0.2})Ge_3$ showing a two peak profile similar to that of $GaAsGe_3$ compound.

change in any measurable manner by replacing As with P over a broad range up to x = 0.2.

It is noted that this trend is reminiscent of prior absorption measurements of $(GaAs)_x(Ge_2)_{1-x}$ alloys, which showed a nearly constant band gap energy of 0.5 eV as a function of Ge over a broad range of 30%-70%.[143] As in the case of $GaAsGe_3$, infrared (IR) spectroscopic ellipsometry also shows evidence for a direct optical transition (described below) at an energy close to the PL emission features in Figure 50. Also, note that the PL peaks in this figure are consistently narrower than those obtained for $GaAsGe_3$. Given the superior structural quality of the P-containing samples, this narrowing is consistent with an assignment to intrinsic features rather than defects. On the other hand, the disappearance of emission for $x > 0.2$ is intriguing. Studies of $(GaAs)_{1-x}Ge_{2x}$ alloys suggest that the large negative bowing of the band gap in this system is correlated with a strong valence band localization on the As atoms.[164] This may not be the case with P, and if so III-P-Ge compounds may not share the anomalously low band gap observed in compounds such as $(GaAs)_{1-x}Ge_{2x}$ or $(GaSb)_{1-x}Ge_{2x}$.[165] The nature of the lowest band gap of P-rich $Ga(As_{1-x}P_x)Ge_3$ alloys is very important from the point of view of potential applications and will be the subject of future research.

Higher-energy transitions were investigated using UV-visible ellipsometry. The measurements were carried out in a JA Woollam UV-VIS VASE system, in a photon energy range of 0.6 - 4.8 eV with a 10 meV step size. The sample structure was modeled as a Si substrate, a $Ge_{1-x}Si_x$ buffer layer, a $Ga(As_{1-x}P_x)Ge_3$ material layer, a thin (1-2 nm) GeO_2 layer, and a surface roughness layer. The optical constants for all layers were taken

from the literature except for the targeted $Ga(As_{1-x}P_x)Ge_3$, for which a parametric oscillator model was used. In a second step, all the thicknesses from the first fit were kept fixed and the ellipsometric data were fit again using the real and imaginary parts of the $Ga(As_{1-x}P_x)Ge_3$ dielectric function as adjustable parameters, and seeding the fit at one energy value with the dielectric function determined at the previous energy. This point-by-point fit largely eliminates any possible bias introduced by the parameterized model using in the first step. The absorption coefficients of the alloys were then computed from the real and imaginary parts of the dielectric function.

Figure 51 shows a comparison of the absorption coefficients of a representative $GaAs_{0.7}P_{0.3}Ge_3$ alloy with those of the $GaAsGe_3$ and $GaPGe_{3.3}$ end members, as well as Ge, GaP, GaAs and amorphous Si references. Note that as P replaces As, the absorption shifts to higher energies. The absorption coefficient for $GaAsGe_3$ is higher than that of $GaPGe_{3.3}$ over the full spectrum range, and the difference is more pronounced in the visible-IR region ($E < 3.1$ eV). The absorption coefficient of the $GaAs_{0.7}P_{0.3}Ge_3$ sample lies right in between the spectra of the two end compounds. The absorption coefficients of $Ga(As_{1-x}P_x)Ge_3$ samples are much higher than those of GaP and GaAs in almost all the energy range from 1 eV to 4.8 eV, and are also higher than amorphous Si in almost all the visible-IR region ($E < 3.1$ eV). These materials showed slightly lower absorption compared to the pure Ge reference, but one can notice that the absorption of $GaAsGe_3$ is higher than Ge in the range of 1.5 - 2 eV. The data show that alloying between GaP, Ga, and Ge leads to tunable absorption properties of $Ga(As_{1-x}P_x)Ge_3$ intermediate materials.

Furthermore, they exhibit extended coverage in the IR range, indicating possible applications in optoelectronics, including photovoltaics.

IR ellipsometry was used to characterize the low energy transitions in the band structure. The dielectric functions ε_1 and ε_2 were fitted using both model and point-by-point procedures, for a representative $GaAs_{0.8}P_{0.2}Ge_3$ sample. In both cases a clear E_0 transition could be seen at $E = 0.59$ eV, which agrees very well with the PL data in Figure 50 above.

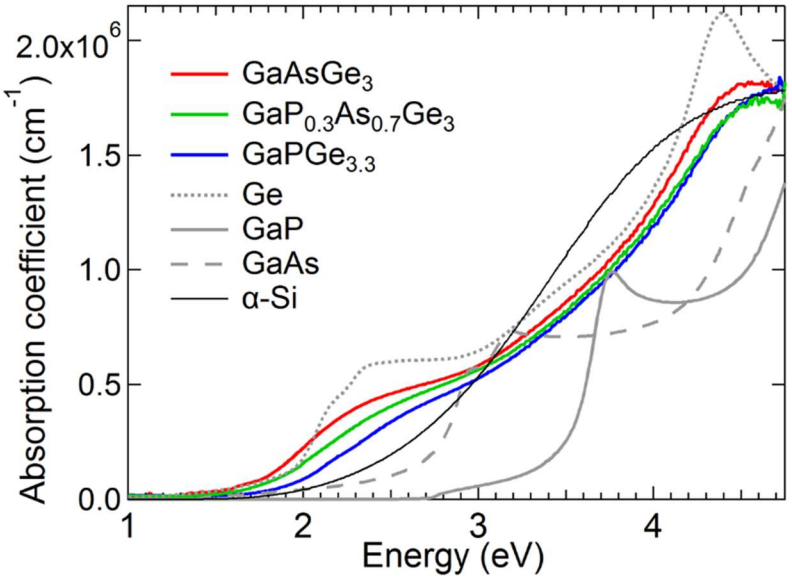

Figure 51: Plots of absorption coefficients from a $GaAs_{0.7}P_{0.3}Ge_3$ sample and reference GaP, GaAs, and Ge end members as well as amorphous Si. The latter is known to exhibit enhanced absorption relative to crystalline Si providing a useful figure of merit for comparing the photovoltaic potential of group IV based compounds from a light absorption perspective. The most striking outcome of the measurements is that the alloy absorption intensities are found to be intermediate to those of the end members, as expected, for the high-energy transitions in the band structure.

5.4 Summary

In summary, a new class of group III-V-IV hybrid alloys with $Ga(As_{1-x}P_x)Ge_3$ compositions (x = 0 - 1) was synthesized via reactions of $[D_2GaN(CH_3)_2]_2$ with $P(GeH_3)_3$ and $As(GeH_3)_3$ molecular sources. These materials are grown on Si wafers, using for the first time lattice-engineered $Ge_{1-x}Si_x$ buffer layers with continuously tunable lattice constants that match the dimensions of the alloy product, making them ideal platforms for subsequent integration of defect-free $Ga(As_{1-x}P_x)Ge_3$ epilayers. The growth mechanism proceeds *via* epitaxial assembly of $GaPGe_3$ and $GaAsGe_3$ building blocks, leading to single-phase monocrystalline layers with metastable diamond-like structures based on the Ge network. The structural and bonding properties are found to interpolate between Ge, GaAs, and GaP end members, in agreement with theoretical simulations. PL measurements suggest a large negative bowing of the band gap for As-rich samples as expected on account of strong valence band localization on the As atom. Ellipsometry measurements of the dielectric function revealed tunable absorption as a function of composition, and demonstrated extended coverage in the IR range indicating possible applications in optoelectronics. The above synthetic approach was further applied to the development of related $(GaP)_yGe_{5-2y}$ solid solutions grown on $Ge_{1-x}Si_x$ buffered Si(100) with varying Ge contents up to 90%. The latter contain highly dispersed Ga-P pairs within the parent Ge matrix, indicating that new functionalities are likely by altering the electronic structure while preserving the random diamond lattice of the resultant crystal.

In the case of $Al(P_{1-x}Sb_x)Si_3$, highly crystalline P-rich alloys have been successfully produced in the composition range x = 0.01- 0.15. However, while attempts to produce Sb-rich samples, such as pure $AlSbSi_3$, have achieved the desired composition, thus far attempts to grow oriented, monocrystalline films have failed likely due to the large lattice mismatch between the $AlSbSi_3$ layer and the Ge/Si substrates. Larger platforms are necessary to induce epitaxial growth and $Ge_{1-y}Sn_y$ may be an option for virtual substrates in further experiments.

Chapter 6

BEYOND GERMANIUM: SYNTHESIS OF III-V MATERIALS VIA REACTIONS BETWEEN $Al(BH_4)_3$ AND PH_3 AND SbD_3 GROUP V HYDRIDES

Portions of this chapter describe experiments performed by Dr. Patrick E. Sims, data from those experiments is used here with his written permission.

Synopsis

In the final chapter of this thesis, III-V materials with compositions BP and $Al_{1-x}B_xSb$ were produced in order to further explore reactions between $Al(BH_4)_3$ and Group V hydrides. $Al(BH_4)_3$ was used as a source of both Al and B in combination with PH_3 and SbD_3 as Group V sources. In the case of reactions between $Al(BH_4)_3$ and PH_3, B-rich $B_{1-x}Al_xP$ and pure BP alloys were formed allowing a CVD route toward BP thin films on Si(100). While in reactions between $Al(BH_4)_3$ and SbD_3, Al-rich $Al_{1-x}B_xSb$ films ($x \sim 0.05$) were produced. A CVD process capable of integrating BP and BSb thin films directly with Si-based technologies would be extremely beneficial for heat dissipation in power electronics. Progress toward the synthesis of BP and BSb alloys is described below.

6.1 Introduction

Given the success of $Al(BH_4)_3$ as a source of Al and B in III-V-IV alloys it was subsequently used in combination with Group V hydrides in order to further explore its behavior in forming III-V pairs. PH_3 and SbD_3 were chosen as Group V sources in order mimic the III-V portion of the $Al(P_{1-x}Sb_x)Si_3$ alloys described in Chapter 5. Surprisingly, in reactions involving SbD_3, the $Al(BH_4)_3$ acted almost exclusively as a source of Al giving Al-rich $Al_{1-x}B_xSb$ films. However, in the case of PH_3, the $Al(BH_4)_3$ acted only as a source of B resulting in pure BP films. This is indicative of the relative stability between BP and BSb, the latter being thermodynamically unstable due to the large atomic size difference between the constituent atoms. Nevertheless, $Al(BH_4)_3$ and PH_3 have been shown to be potential gaseous precursors for CVD growth of BP.

Boron phosphide, with a cubic zincblende structure, exhibits a wide range of useful properties. These include chemical inertness toward strong acids, bases, or oxidizers, high hardness comparable to that of SiC, and excellent thermal conductivity.[166] Furthermore, BP is a semiconductor with a bandgap of ~2.0 eV in the optical region of the electromagnetic spectrum.[167-169] Finally, B has a large neutron capture cross-section, making the material a promising candidate for the fabrication of solid-state neutron detectors operating at room temperature.[167] Other applications that can benefit from this unique combination of properties include protective IR coatings and thermoelectric devices.[170,171] However, it has not seen widespread use due to the challenges faced in synthesizing the material.[166]

The first modern synthesis of BP, achieved by heating the constituent elements within a sealed chamber to 1100 ºC, was reported by Popper and Ingels.[172] While several researchers have reported the synthesis of BP via reaction of the elements since that time, the method is not straightforward due to the large differences between the chemical and physical properties of B and P sources.[166,173,174] Therefore, alternate methods have been explored for the synthesis of BP. The reaction of boron and phosphorus halides has been reported,[175] as have more unusual synthesis methods such as growth of BP from molten metal phosphides.[176] In addition to bulk scale approaches, CVD techniques have gained popularity for depositing BP films for electronic device applications. The precursors typically used in this case are B_2H_6 and PH_3,[168,171,177] but B and P halide compounds[169] and metal-organic analogues have also been employed.[178] The deposition temperatures are typically in the 800 – 1070 ºC range. Several successful devices have been fabricated using CVD BP materials. For example, Kumashiro and Okada demonstrated working Schottky barrier diodes made from films deposited using B_2H_6 and PH_3,[177] and Lund *et al.* used CVD samples to fabricate BP radiation detectors.[167]

Crystalline compounds containing B-P bonds are relatively uncommon. A binary analogue to BP is the boron rich $B_{12}P_2$ phase whose structure comprises of icosahedral B_{12} units linked together through B-P bonds. This material is more stable than BP at higher temperatures above 800 °C and has been shown to possess self-healing properties making it a potential candidate for radiation–resistant applications.[179] Other known examples of compounds with B-P bonds are ternary halides with compositions PB_4F_9 and $P_2B_4Cl_4$ and compounds of the form A_3BP_2 where A is an alkali metal atom.[164] Recently,

formation of B-P bonds was demonstrated in a new III-V-IV alloy with diamond like structure, $Al_{1-x}B_xPSi_3$.[28] This material was deposited epitaxially on Si(100) substrates via CVD using the novel gas phase precursors $P(SiH_3)_3$ and $Al(BH_4)_3$. The success of this synthetic method raises the possibility of using a similar CVD method for the synthesis of BP. A new synthetic route would be a significant advance in the field.

In this chapter $Al(BH_4)_3$ is used as a precursor with PH_3 to synthesize films of BP on Si(100) substrates at much lower temperatures, 580 – 650 ºC, than has been used in previous CVD methods. The low temperatures used in this process may be particularly advantageous in the fabrication of IR optical coatings using BP. Crystalline materials were obtained via this method, and were subjected to thorough characterization to elucidate structure and composition.

6.2 Low-Pressure CVD Methods to Produce BP and $Al_{1-x}B_xSb$ Materials

The approach to BP synthesis is based on gas-phase reactions of $Al(BH_4)_3$ and PH_3 as the sources of B and P atoms, respectively. The $Al(BH_4)_3$ compound is a volatile liquid with 50 Torr vapor pressure at room temperature making it an versatile candidate for CVD applications. This material is synthesized using literature methods and stored at low temperature for extended periods of time without decomposition. The PH_3 co-reactant is also synthesized using known recipes in small quantities as needed for this application. Aliquots of each precursor are diluted with H_2 and placed into separate containers. These are then attached to the flow manifold of an inductively heated CVD

reactor. The latter comprises a water-cooled deposition constructed using fused quartz. This is attached to a stainless steel UHV chamber using high vacuum components. The system is evacuated to 10^{-9} Torr using a cryopump backed by a series of turbo pumps ensuring high purity thermal processing. The substrate holder is a graphite susceptor inductively heated by a radio frequency (RF) generator. The surface is coated with an amorphous silicon film using SiH_4 to prevent degassing of residual impurities. In some cases a molybdenum block was employed as a heating element. This proved to be particularly useful for low-*p* depositions under ultra-pure conditions. Si(100) wafers were used to investigate proof of concept feasibility of the deposition process. It is worth noting that there are no commercially available substrates that allow for perfect lattice match of BP or BSb compounds. Furthermore, it is unlikely that these materials will grow as single crystals on severely mismatched substrates, as is the case, for example for Ge on Si.

In a typical experiment, the substrates are loaded onto the heating stage of the reactor and inserted into the deposition tube under UHV conditions using a differentially pumped load lock mechanism. The samples are first heated inside to 800 °C for 30 minutes under vacuum to degas the surface. The temperature is then adjusted between 580-650 °C and a background pressure of 50 Torr is then established inside the reactors using a dynamic flow of 5% H_2 in argon carrier gas. The $Al(BH_4)_3$ and PH_3 gaseous reactants are dispensed separately and allowed to flow into the reactor along with the diluent gas stream using mass flow controllers. The latter facilitate steady flow of the co-reactants over the substrate surface initiating crystal growth. A typical run takes 30

minutes yielding layers with reflective surfaces and large thicknesses up to 600 nm depending on the temperature.

Experiments growing BSb films utilize $Al(BH_4)_3$ as the source of B and SbD_3, analogous to the commercial PH_3, as the source of Sb. SbD_3 is selected over SbH_3 because it is thermally robust at room temperature. The replacement of H by D provides sufficient kinetic stability to synthesize and store the compound over the period of at least a month and beyond. SbD_3 has been synthesized in practical yields via reactions of commercially available $SbCl_3$ and $LiGaD_4$ or $LiAlD_4$ reagents. Proof of concept deposition reactions of SbD_3 and $Al(BH_4)_3$ produced mirror like films grown directly onto Si(100) utilizing the CVD tool described above for BP. Prior to growth all substrates were degreased in methanol, dipped in a 5% HF solution for 2 minutes to remove the native oxide, and dried under a flow of N_2. The clean wafers were loaded into the chamber and outgassed at 500 °C until the reactor reached a base pressure of $1.0x10^{-8}$ Torr. The chamber was pressurized to 5 Torr using a stream of 5% H_2 in argon. Stock mixtures of 1:10 SbD_3:H_2 and 1:20 $Al(BH_4)_3$:H_2 were prepared and passed through calibrated mass flow controllers in a 1:1 stoichiometric ratio. Depositions were performed at temperatures ranging from 330-400 °C over 15 minute periods resulting in 100 - 150 nm thick films depending on the growth temperature used. These conditions consistently yielded samples with compositions $Al_{1-x}B_xSb$ ($x \sim 0.05$) as determined by RBS and SIMS.

6.3 Composition and Structural Analysis of BP and $Al_{1-x}B_xSb$ Materials

As indicated above, a series of exploratory reactions were initially conducted directly on Si wafers with intact native oxide to gauge the reactivity profile of the chemical sources under varying *T*/*p* conditions. The resulting samples exhibit smooth, mirror-like morphologies as grown. It was found that at $p \sim 50$ Torr and substrate $T \sim 600$ ^{o}C the reactions consistently produce pure BP layers with thicknesses exceeding 600 nm. The bulk elemental content is this case was established by RBS. The 2.0 MeV spectra (not shown) showed a strong P signal and a weak B step overlaid on the broad Si background. The boron signal was significantly enhanced using a resonance reaction at 3.9 MeV as illustrated in the inset of Figure 52 that shows a strong and well-defined boron peak. Fitting of the data using the program XRump gave a nominal composition of $BP_{1.1}$ well within the range of the stoichiometric zincblende phase. The absence of excess B in samples produced under the 50 Torr and 600 ^{o}C conditions indicates that the reaction mechanism between $Al(BH_4)_3$ and PH_3 does not favor the formation of boron rich B_6P impurities. Furthermore, no measurable amount of Al was detected in these samples by RBS precluding formation of AlP and related phases. This was corroborated by SIMS plots as illustrated in Figure 52, which shows the elemental profiles for a 500 nm thick sample grown on Si. The data revealed near background levels of aluminum as evidenced by the vanishing counts through the entire layer thickness. Using the well-established $AlPSi_3$ phase as a reference standard it was found that the amount of Al is at or near the detection limit relative to P. In this regard, one should note that the intensity

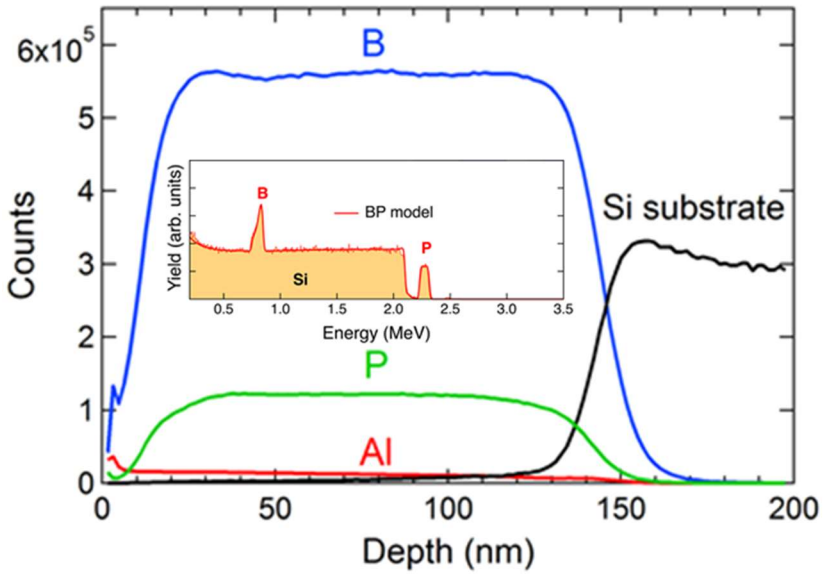

Figure 52: Main Panel – SIMS spectra of a BP film, flat traces for both the B and P contributions in the epilayer are clearly seen with no contribution from Al. Inset - Boron resonance RBS spectra of a BP film grown on Si(100), distinct signals from the B and P contributions in the epilayer are again clearly visible.

of the Al signal intensity in the SIMS spectra is typically found to be vastly enhanced relative to P further corroborating the dearth of Al in the BP samples. In contrast to Al, the B and P constituents are prominently displayed in the SIMS spectra indicating that the material is a pure combination of the two elements.

The composition was further determined by electron energy loss spectroscopy (EELS). Thin, electron beam transparent specimens were made and analyzed using a JEOL ARM200F aberration corrected transmission electron microscope fitted with an Enfinium EELS spectrometer. Figure 53 shows EELS spectra featuring the K-edges of B and P. Background subtraction followed by peak integration yielded a BP stoichiometry. Corresponding elemental maps were then generated from nanoscale areas throughout the

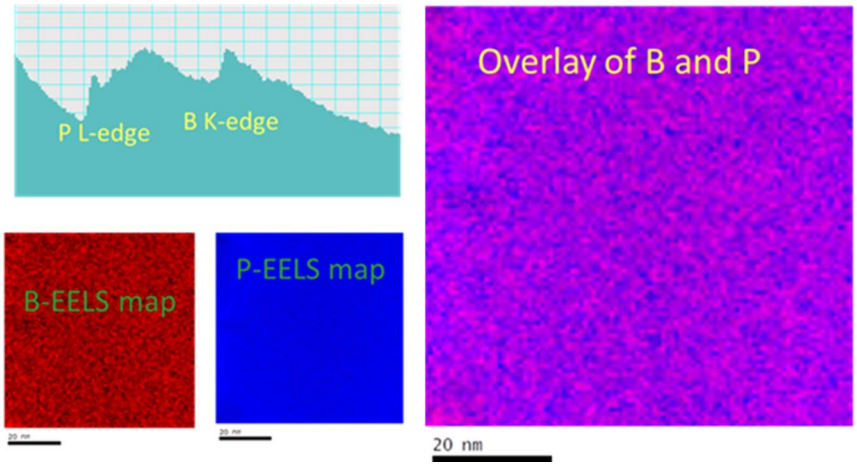

Figure 53: EELS spectra of a BP sample showing a uniform atomic distribution of B and P atoms devoid of Al. Maps showing both B and P contributions as well as an overlay of B and P can be seen.

crystal to further investigate the elemental purity of the samples. Figure 53 shows individual B and P maps as well as their overlay illustrating a uniform distribution within the field of view indicating phase pure BP material devoid B-rich impurities. Moreover, no Al was seen in the EELS spectra corroborating the above SIMS and RBS findings.

The absence of Al in the samples suggests that the Al atom in $Al(BH_4)_3$ is eliminated as a volatile byproduct. This can be explained by the proposed reaction mechanism described below by Reaction (1).

$$Al(BH_4)_3 + PH_3 \rightarrow 3BP + \text{“}AlH_3\text{”} + 9/2H_2 \quad (1)$$

This shows the formation of AlH_3 molecular intermediates that seemingly do not participate in the reaction process. The AlH_3 compound is known to exist as a polymeric solid in the condensed state containing six fold coordinated Al centers that are interconnected with bridging H atoms. It is possible that under the reactions conditions

volatile AlH_3 monomers or short-lived oligomers are first generated and then removed from the reaction medium under the dynamic conditions of the deposition process. Another possibility is that Al is removed in the form of partially substituted $AlH_x(BH_4)_{3-x}$ derivatives that are produced by the unimolecular decomposition of the parent $Al(BH_4)_3$ species. This scenario is supported by the known dissociation of $Al(BH_4)_3$ at 70 ^oC to produce stable dimers of $HAl(BH_4)_2$ and B_2H_6 according to Reaction (2) below. In this case, the highly reactive BH_3 readily combines with PH_3 to produce BP.

$$Al(BH_4)_3 \rightarrow HAl(BH_4)_2 + BH_3 \quad (2)$$

In both Reactions (1) and (2), the proposed byproducts are expected to be thermally sensitive and readily decompose under the growth conditions to produce Al or AlB_2 type impurity solids. In practice, it is observed that the process appears to be exclusively driven by the formation of strong B-P bonds ultimately leading to the formation of pure boron phosphide. The aluminum phosphide analogue is not observed in spite of the high activity of PH_3 in the deposition due to the large 10-fold excess employed in the experiments. This is likely due to the much lower stability of Al-P bonding relative to B-P.

Initial investigations of the sample microstructure were performed by XTEM. Micrographs of the entire layer revealed columnar growth on the SiO_2 wafer surface. The data shows a typical view featuring crystalline domains that originate at the interface and extend through the layer to the top surface. Selected area diffraction showed

polycrystalline ring patterns containing diffraction spots that can be assigned to preferentially oriented cubic material (see inset of Figure 54). High-resolution images revealed large crystallites with cubic structure throughout the layer with no sign of epitaxy at the interface as illustrated in Figure 54. The observation of extensive zincblende-BP crystallization by TEM at the low growth temperature (~600 ºC) employed here was corroborated by FT-IR transmission measurements. This is illustrated by the sharp IR band at ~818 cm^{-1} in the inset of Figure 54 corresponding to zincblende B-P vibrations. The Raman spectra also showed a sharp peak at 820 cm^{-1}, further

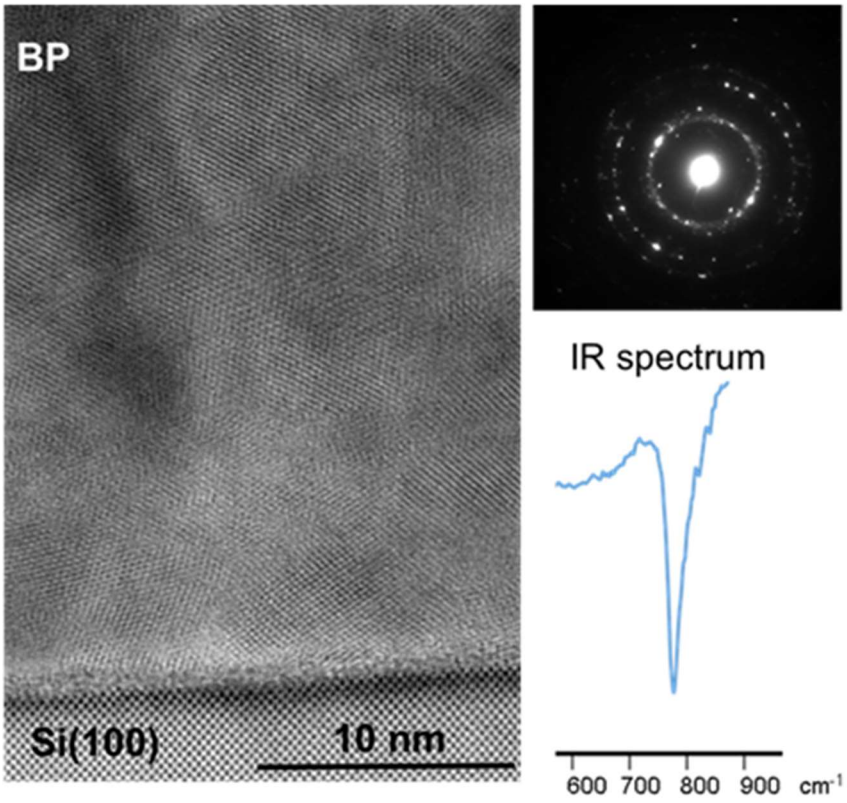

Figure 54: XTEM micrographs of a BP sample grown directly onto Si(100). Multiple crystallites can be seen within the field of view, and electron diffraction shown in the top left reveals ring patterns with some orientation. The bottom left panel shows a transmission FT-IR spectrum of a BP film with a sharp peak corresponding to a B-P vibration.

corroborating the presence of BP crystals. It is apparent from the above structural and spectroscopic data that the controlled depositions afforded by the high reactivity of $Al(BH_4)_3$ tend to promote tetrahedral bonding as required for the fabrication of the cubic structures, rather than formation of multiple B-B bonding corresponding to non-stoichiometric B-rich phases.

Films comprising of $Al_{1-x}B_xSb$ were analyzed using similar methods as described above for BP. Figure 55 shows a typical 2.0 MeV RBS plot of an $Al_{1-x}B_xSb$ film deposited directly onto Si(100). A computational model was produced using XRump and the composition was found to be $Al_{0.95}B_{0.05}Sb$. Both Al and Sb peaks are clearly visible, however, no B peak is visible even at B resonance energies (~3.9 MeV) indicating very

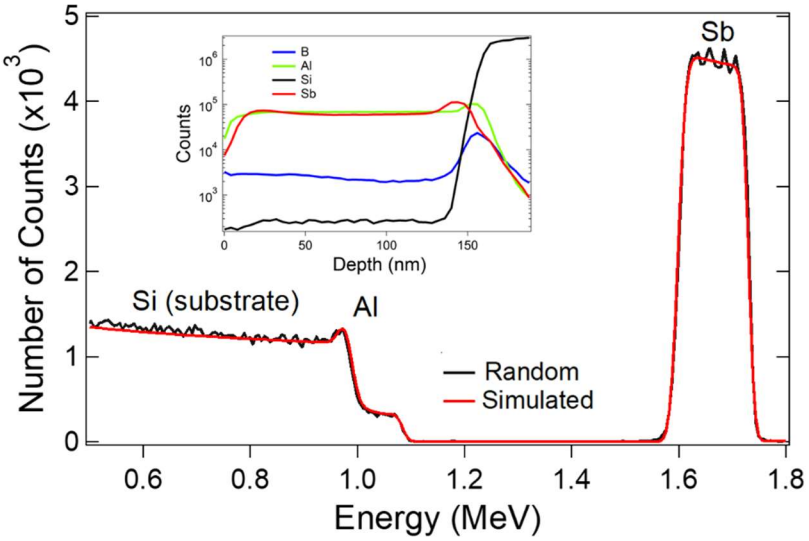

Figure 55: Main Panel - 2.0 MeV RBS spectra of an $Al_{0.95}B_{0.05}Sb$ film on Si, the black trace is a spectra collected at a random angle, the red trace is a computational model of the material. Distinct peaks can be seen for Al, and Sb. Note the B concentration is too low to be seen above the signal from the Si substrate. Inset – SIMS profile of the same $Al_{0.95}B_{0.05}Sb$ film, the traces for B, Al, and Sb (blue, green, and red respectively) are flat throughout the layer indicating uniform composition.

low incorporation of B into the film which cannot be seen due to the intense signal from the Si substrate. No channeling experiments were successful in this material system indicating a misaligned film. Additional compositional analysis was performed using secondary-ion mass spectrometry (SIMS) which confirmed the incorporation of 5% B relative to Sb. Representative SIMS data can be viewed in the inset of Figure 55. A clear flat signal can be seen for B (blue trace) as well as contributions from Al (green trace), and Sb (red trace). Flat profiles can been see for all three elements indicating that their composition remains constant throughout the layer.

Structural analysis was performed via XTEM using an FEI Titan 80-300 electron microscope. Figure 56(a) shows a high resolution micrograph of a $Al_{0.95}B_{0.05}Sb$ film grown directly onto a Si(100) substrate. A clear transition can be seen at the interface marked by an arrow where highly defected $Al_{0.95}B_{0.05}Sb$ can be seen. After the first few nanometers of growth the crystallinity of the sample improves although several stacking faults can be seen propagating along the [111] direction. Electron diffraction measurements can be seen in panel (b) unlike in the BP system no ring patterns were observed and distinct diffraction points can be seen for both the $Al_{0.95}B_{0.05}Sb$ epilayer as well as the Si substrate. No peaks were observed in HR-XRD scans of these films, which is unusual given the crystallinity seen in the XTEM images. It may be that the epilayer is severely misaligned to the underlying Si(100) substrate, making alignment to the (004) reflection from the epilayer nearly impossible under high-resolution conditions. Panel (c) shows a transmission FT-IR spectrum of the film, a sharp peak can be seen at 318 cm^{-1}

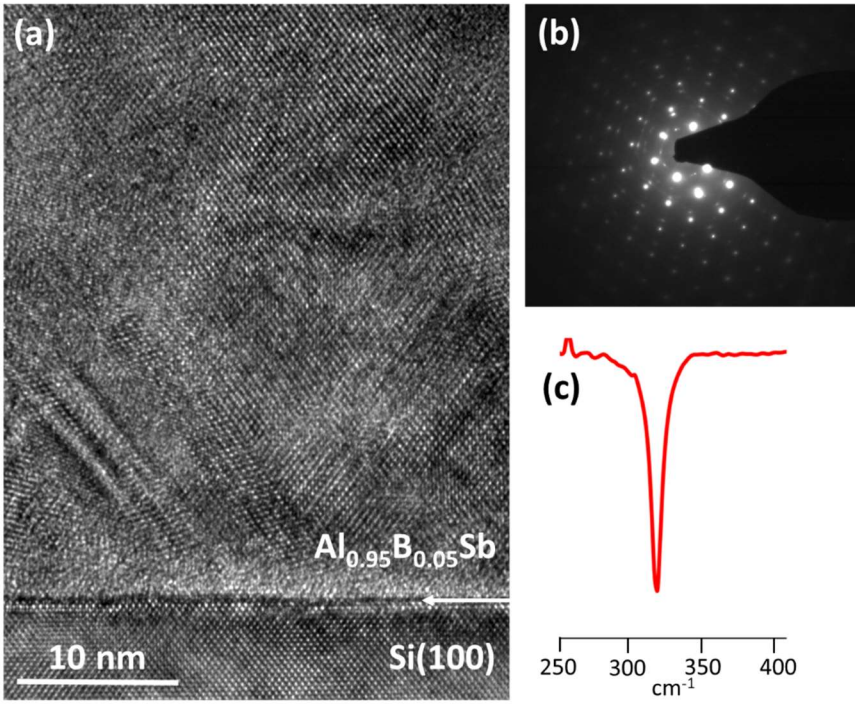

Figure 56: Panel (a) - XTEM micrographs of an $Al_{0.95}B_{0.05}Sb$ sample grown directly onto Si(100). Multiple stacking faults can be seen within the field of view. Electron diffraction (panel (b)) reveals a mostly single crystal material with distinct patterns for the epilayer and substrate. Panel (c) shows a transmission FT-IR spectrum of a $Al_{0.95}B_{0.05}Sb$ film, a sharp peak can be seen at 318 cm^{-1} corresponding to an Al-Sb vibration.

corresponding to zincblende Al-Sb vibrations. The sharpness of the peak indicates the film is of good crystalline quality.

Interestingly, reactions between $Al(BH_4)_3$ and PH_3 routinely resulted in the formation of pure BP films, meaning that the PH_3 precursor preferentially reacted with the BH_3 decomposition product shown in Reaction (2) above. However, in the case of SbD_3 only small amounts of B-Sb bonding was observed, and the SbD_3 preferentially reacted with Al to form Al-Sb bonds. This is in spite of the higher concentration of B available for bonding. This is not surprising as B-Sb is likely to be far less stable than Al-

Sb due to the large atomic size difference between the constituent atoms, and thus Al-Sb bonds are formed much more readily and Al-rich $Al_{1-x}B_xSb$ alloys are formed.

Ultimately crystalline $Al_{0.95}B_{0.05}Sb$ films have been routinely produced, but the large lattice mismatch between the epilayer and the underlying Si(100) substrates has yielded severely misaligned films that are difficult if not impossible to analyze through HR-XRD. Much larger lattice constant substrates, such as ZnTe, could be used in order to allow better commensuration for epitaxial growth.

6.4 Summary

Use of $Al(BH_4)_3$ in combination with PH_3 was successful in producing pure BP films directly onto Si(100) substrates. XTEM analysis revealed the films had grown polycrystalline with large cubic crystallites. B-P bonding was apparent through transmission FT-IR meaning the method described here is capable of producing crystalline BP films directly onto Si(100) using common CVD techniques. Using similar methods, reactions between $Al(BH_4)_3$ and SbD_3 produced Al-rich $Al_{1-x}B_xSb$ films. These films were found to be highly defected and misaligned relative to the Si(100) substrates, however the films grew epitaxially and were monocrystalline. The high defectivity is likely due to the extreme lattice mismatch between the epilayer and the substrate, and substrates that are more suitable must be used in order to produce high quality films.

REFERENCES

1 Haller E.E. *Mater. Sci. Semicond. Process*. **2006**, *9*, 408.

2 Bardeen, J.; Brattain, W.H. *Phys. Rev*. **1948**, *74*, 230.

3 Kilby, J. *ChemPhysChem* 2001, *2*, 482.

4 Braunstein, R. *Phys. Rev.* **1955**, *99,* 1892.

5 Gupta, S.; Magyari-Köpe, B.; Nishi, Y.; Saraswat, K.C. *J. Appl. Phys*. **2013**, *113*, 073707.

6 Gallagher, J. D.; Senaratne, C. L.; Kouvetakis, J.; Menéndez, J. *Appl. Phys. Lett.* **2014**, *105*, 142102.

7 Moontragoon, P.; Ikonic, Z.; Harrison, P. *Semicond. Sci. Tech.* **2007***, 22*, 742.

8 Shah, S.; Greene, J.E.; Abels, L.L.; Yao, Q.; Raccah, P.M. *J. Cryst. Growth* **1987**, *83*, 3.

9 He, G.; Atwater, H.A. *Nucl. Instrum. Meth. Phys. Res. B.* **1995**, *106*, 126.

10 Taraci, J.; Tolle, J.; McCartney, M.R.; Menendez, J.; Santana, M.; Smith, D.J.; Kouvetakis, J. *Appl. Phys. Lett*. **2001**, *78*, 3607.

11 Taraci, J.; Zollner, S.; McCartney, M. R.; Menendez, J.; Smith, D.J.; Tolle, J.; Bauer, M.; Duda, E.; Edwards, N. V.; Kouvetakis, J. *Mater. Res. Soc. Symp. P.* **2002**, *602*, 1141.

12 Wirths, S.; Geiger, R.; von den Driesch, N.; Mussler, G.; Stoica, T.; Mantl, S.; Ikonic, Z.; Luysberg, M.; Chiussi, S.; Hartmann, J.M.; Sigg, H.; Faist, J.; Buca, D.; Grutzmacher, D. *Nat. Photonics* **2015**, *9*, 88.

13 Jiang, L.; Xu, C.; Gallagher, J.D.; Favaro, R.; Aoki, T.; Menéndez, J.; Kouvetakis, J. *Chem. Mater.* **2014**, *26*, 2522.

14 Margetis, J.; Mosleh, A.; Al-Kabi, S.; Ghetmiri, S.A.; Due, W.; Dou, W.; Benamara, M.; Li, B.; Mortazavi, M.; Naseem, H.A.; Yu, S.Q.; Tolle, J. *J. Cryst. Growth* **2017**, *463*, 128.

15 Xu, C.; Gallagher, J.D.; Sims, P.; Smith, D.J.; Menéndez, J; Kouvetakis, J. *Semicond. Sci. Tech.* **2015**, *30*, 1.

16 Xu, C.; Senaratne, C.L.; Sims, P.; Kouvetakis, J.; Menéndez, J. *ACS Appl. Mater. Inter.* **2016**, *8*, 23810.

17 D'Costa, V.R.; Tolle, J.; Xie, J.; Kouvetakis, J.; Menéndez, J. *Phys. Rev. B* **2009**, *80*, 125209.

18 Fang, Y.Y.; Tolle, J.; Chizmeshya, A.V.G.; Kouvetakis, J.; D'Costa, V.R.; Menendez, J. *Appl. Phys. Lett.* **2009**, *95*, 081113.

19 Radamson, H.H.; Joelsson, K.B.; Ni, W.X.; Birch, J.; Sundgren, J.E.; Hultman, L.; Hansson, G.V. *J. Cryst. Growth* **1996**, *167*, 495.

20 Sims, P.E.; Xu, C; Poweleit, C.D.; Menéndez, J.; Kouvetakis, J. *Chem. Mater.* **2017***, 29*, 3202.

21 Smith, D.J.; Aoki, T.; Furdyna, J.K.; Liu, X.; McCartney, M.R.; Zhang, Y.H. *J. Phys. Conf. Ser.* **2013**, *471*, 012005.

22 Norman, A.G.; Olson, J.M.; Geisz, J.F.; Moutinho, H.R.; Mason, A.; Al-Jassim, M.M.; Vernon, S.M. *Appl. Phys. Lett.* **1999**, *74*, 1382.

23 Giorgi, G.; Van Schilfgaarde, M.; Korkin, A.; Yamashita, K. *Nanoscale Res. Lett.* **2010**, *5*, 469.

24 Watkins, T.; Chizmeshya, A.V.G.; Jiang, L.; Smith, D.J.; Beeler, R.T.; Grzybowski, G.; Poweleit, C.D.; Menéndez, J.; Kouvetakis, J. *J. Am. Chem. Soc.* **2011**, *133*, 16212.

25 Watkins, T.; Jiang, L.; Xu, C.; Chizmeshya, A.V.G.; Smith, D.J.; Menéndez, J.; Kouvetakis, J. *Appl. Phys. Lett.* **2012**, *100*, 022101.

26 Kouvetakis, J.; Chizmeshya, A.V.G; Watkins, T.; Grzybowski, G.; Jiang, L.; Beeler, R.T.; Menéndez, J. *Chem. Mater.* **2012**, *24*, 3219.

27 Sims, P.E.; Chizmeshya, A.V.G.; Jiang, L.; Beeler, R.T.; Poweleit, C.D.; Gallagher, J.; Smith, D.J.; Menéndez, J.; Kouvetakis, J. *J. Am. Chem. Soc.* **2013***, 135,* 12388.

28 Sims, P.; Aoki, T.; Favaro, R.; Wallace, P.; White, A.; Xu, C.; Menéndez, J.; Kouvetakis, J. *Chem. Mater.* **2015**, *27*, 3030.

29 Jain, A.; McGaughey, A.J.H. *J. Appl. Phys*. **2014**, *116*, 073503.

30 Shibata, T.; Nakata, J.; Nanishi, Y.; Fujimoto, M. *Jpn. J. Appl. Phys*. **1994**, *33*, 1767.

31 Bauer, M.; Taraci, J.; Tolle, J.; Chizmeshya, A.V.G.; Zollner, S.; Smith, D.J.; Menéndez, J.; Hu, C.; Kouvetakis, *J. Appl. Phys. Lett*. **2002**, *81*, 2992.

32 Fleurial, J.P. J. *Electrochem. Soc*. **1990**, *137*, 2928.

33 Freitas, F.L.; Furthmüller, J.; Bechstedt, F.; Marques, M.; Teles, L.K. *Appl. Phys. Lett.* **2016**, *108*, 092101.

34 Tseng, H.H.; Wu, K.Y.; Li, H.; Mashanov, V.; Cheng, H.H.; Sun, G.; Soref, R.A. *Appl. Phys. Lett*. **2013**, *102*, 182106.

35 Du, W.; Zhou, Y.; Ghetmiri, S.A.; Mosleh, A.; Conley, B. R.; Nazzal, A.; Soref, R.A.; Sun, G.; Tolle, J.; Margetis, J.; Naseem, H.A.; Yu, S.Q. *Appl. Phys. Lett*. **2014**, *104*, 241110.

36 Wirths, S.; Buca, D.; Mantl, S. *Prog. Cryst. Growth Ch*. **2016**, *62*, 1.

37 Gallagher, J.D.; Senaratne, C.L.; Sims, P.; Aoki, T.; Menéndez, J.; Kouvetakis, J. *Appl. Phys. Lett*. **2015**, *106*, 091103.

38 Sun, G.; Soref, R.A.; Cheng, H.H. *J. Appl. Phys*. **2010**, *108*, 033107.

39 Sweeney, S.J.; Adams, A.R.; Silver, M.; O'Reilly, E.P.; Watling, J.R.; Walker, A.B.; Thijs, P.J.A. *Phys. Status Solidi* **1999**, *211*, 525.

40 Ventura, C.I.; Fuhr, J.D.; Barrio, R.A. *Phys. Rev. B* **2009**, *79*, 155202.

41 Gencarelli, F.; Vincent, B.; Souriau, L.; Richard, O.; Vandervorst, W.; Loo, R.; Caymax, M.; Heyns, M. *Thin Solid Films* **2012**, *520*, 3211.

42 Woelk E. and Loo, R. *Solid State Technol*. **2014**, *58*, 37.

43 Grzybowski, G.; Beeler, R.T.; Jiang, L.; Smith, D.J.; Kouvetakis, J.; Menéndez, J. *Appl. Phys. Lett*. **2012**, *101*, 072105.

44 Spohn, R.F. and Richenberg, C.B. *ECS Trans*. **2012**, *50*, 921.

45 Rivard, E. *Chem. Soc. Rev*. **2016**, *45*, 989.

46 von den Driesch, N.; Stange, D.; Wirths, S.; Mussler, G.; Holländer, B.; Ikonic, Z.; Hartmann, J.M.; Stoica, T.; Mantl, S.; Grützmacher, D.; Buca, D. *Chem. Mater*. **2015**, *27*, 4693.

47 Bentham, J.E.; Cradock, S.; Ebsworth, E.A.V. *Inorg. Nucl. Chem. Lett*. **1971** *7*, 1077.

48 Feltrin, A. and Freundlich, A. *Renew. Energ*. **2008**, *33*, 180.

49 Senaratne, C.L.; Gallagher, J.D.; Jiang, L.; Aoki, T.; Menéndez, J.; Kouvetakis, J. *J. Appl. Phys*. **2014**, *116*, 133509.

50 Oehme, M.; Werner, J.; Gollhofer, M.; Schmid, M.; Kaschel, M.; Kasper, E.; Schulze, J. *IEEE Photonic. Tech. L*. **2011**, *23*, 1751.

51 Oehme, M.; Kasper, E.; Schulze, J. *ECS J. Solid State Sci. Technol*. **2016**, *2*, R76.

52 Oehme, M.; Kostecki, K.; Arguirov, T.; Mussler, G.; Ye, K.; Gollhofer, M.;

53 Schmid, M.; Kaschel, M.; Korner, R.A.; Kittler, M.; Buca, D.; Kasper, E.; Schulze, J. *IEEE Photonic. Tech. L.* **2014**, *26*, 187.

54 Kasper, E. and Oehme, M. *Jpn. J. Appl. Phys. Part 1* **2015**, *54*, 04DG11.

55 Xu, C.; Gallagher, J.D.; Sims, P.; Smith, D.J.; Menéndez, J.; Kouvetakis, J. *Semicond. Sci. Technol*. **2015**, *30*, 045007.

56 Gallagher, J.D.; Senaratne, C.L.; Xu, C.; Sims, P.; Aoki, T.; Smith, D.J.; Menéndez, J.; Kouvetakis, J. *J. Appl. Phys*. **2015**, *117*, 245704.

57 Beeler, R.; Roucka, R.; Chizmeshya, A.V.G.; Kouvetakis, J.; Menéndez, J. *Phys. Rev. B* **2011**, *84*, 035204.

58 Schulte-Braucks, C.; Stange, D.; von den Driesch, N.; Blaeser, S.; Ikonic, Z.; Hartmann, J.M.; Mantl, S.; Buca, D. *Appl. Phys. Lett*. **2015**, *107*, 042101.

59 Schulte-Braucks, C.; Stange, D.; von den Driesch, N.; Blaeser, S.; Ikonic, Z.; Hartmann, J.M.; Mantl, S.; Buca, D. *Appl. Phys. Lett*. **2015**, *107*, 042101.

60 Samavedam, S.B.; Currie, M.T.; Langdo, T.A.; Fitzgerald, E.A. *Appl. Phys. Lett*. **1998**, *73*, 2125.

61 D'Costa, V.R.: Fang, Y.Y.; Tolle,J.; Kouvetakis, J.; Menéndez, J. *Thin Solid Films* **2010***, 518*, 2531.

62 D'Costa, V.R.; Fang, Y.Y.; Tolle, J.; Kouvetakis, J.; Menéndez, J. *Phys. Rev. Lett.* **2009***, 102*, 107403.

63 Van de Walle, C.G. *Phys. Rev. B* **1989**, *39*, 1871.

64 Menéndez, J. and Kouvetakis, J. *Appl. Phys. Lett*. **2004**, *85*, 1175.

65 Jaros, M. *Phys. Rev. B* **1988**, *37*, 7112.

66 Li, Y.H.; Walsh, A.; Chen, S.; Yin, W.J.; Yang, J.H.; Li, J.; Da Silva, J.L.F.; Gong, X.G.; Wei, S.H. *Appl. Phys. Lett.* **2009,** *94*, 212109.

67 Teherani, J.T.; Chern, W.; Antoniadis, D.A.; Hoyt, J.L.; Ruiz, L.; Poweleit, C.D.; Menéndez, J. *Phys. Rev. B* **2012**, *85*, 205308.

68 Thewalt, M.L.W.; Harrison, D.A.; Reinhart, C.F.; Wolk, J.A. *Phys. Rev. Lett*. **1997**, *79*, 269.

69 Li, Y.H.; Gong, X.G.; Wei, S.H. *Phys. Rev. B* **2006**, *73*, 245206.

70 Yamaha, T.; Shibayama, S.; Asano, T.; Kato, K.; Sakashita, M.; Takeuchi, W.; Nakatsuka, O.; Zaima, S. *Appl. Phys. Lett*. **2016**, *108*, 061909.

71 Xu, C.; Beeler, R.T.; Jiang, L.; Grzybowski, G.; Chizmeshya, A.V.G.; Menéndez, J.; Kouvetakis, J. *Semicond. Sci. Technol.* **2013**, *28*, 105001.

72 Jiang, L.; Gallagher, J.D.; Senaratne, C.L.; Aoki, T.; Mathews, J.; Kouvetakis, J.; Menéndez, J. *Semicond. Sci. Technol.* **2014***, 29*, 115028.

73 Xu, C.; Gallagher, J.D.; Senaratne, C.L.; Menéndez, J.; Kouvetakis, J. *Phys. Rev. B* **2016**, *93*, 125206.

74 Moontragoon, P.; Soref, R.; Ikonic, Z. *J. Appl. Phys*. **2012**, *112*, 073106.

75 Sant, S. and Schenk, A. *Appl. Phys. Lett*. **2014**, *105*, 162101.

76 Wenday, T.; Fischer, I.A.; Montanari, M.; Zoellner, M.H.; Klesse, W.; Capellini, G.; von den Driesch, N.; Oehme, M.; Buca, D.; Busch, K.; Schulze, J. *Appl. Phys. Lett.* **2016**, *108*, 242104.

77 Kotlyar, R.; Avci, U.E.; Cea, S.; Rios, R.; Linton, T.D.; Kuhn, K.J.; Young, I.A.; *Appl. Phys. Lett.* **2013**, *102*, 113106.

78 Schulze, J.; Blech, A.; Datta, A.; Fischer, I.; Hähnel, D.; Naasz, S.; Rolseth, E.; Tropper, E.M. *Solid. State. Electron.* **2015**, *110*, 59.

79 Wang, H.; Liu, Y.; Liu, M.; Zhang, Q.; Zhang, C.; Ma, X.; Zhang, J.; Hao, Y.; Han, G. *Superlattices Microstruct.* **2015**, *83*, 401.

80 Wirths, S.; Tiedemann, T.; Ikonic, Z.; Harrison, P.; Holländer, B.; Stoica, T.; Mussler, G.; Myronov, M.; Hartmann, J.M.; Grützmacher, D.; Buca, D.; Mantl, S. *Appl. Phys. Lett.* **2013**, *102*, 10.

81 Gupta, S.; Vincent, B.; Yang, B.; Lin, D.; Gencarelli, F.; Lin, J.Y.J.; Chen, R.; Richard, O.; Bender, H.; Magyari-Kope, B.; Caymax, M.; Dekoster, J.; Nishi, Y.; Saraswat, K. *International Electron Devices Meeting* (IEEE) **2012**, pp 16.2.1

82 Gupta, S.; Chen, R.; Vincent, B.; Lin, D.; Magyari-köpe, B. *ECS Trans.* **2012**, *50*, 937.

83 Sau, J.D. and Cohen, M.L. *Phys. Rev. B* **2007**, *75*, 045208.

84 Liu, L.; Liang, R.; Wang, J.; Xu, J. *J. Appl. Phys.* **2015**, *117*, 184501.

85 Vincent, B.; Shimura, Y.; Takeuchi, S.; Nishimura, T.; Eneman, G.; Firrincieli, A.; Demeulemeester, J.; Vantomme, A.; Clarysse, T.; Nakatsuka, O.; Zaima, S.; Dekoster, J.; Caymax, M.; Loo, R. *Microelectron. Eng.* **2011**, *88*, 342.

86 Roucka, R.; Mathews, J.; Beeler, R.T.; Tolle, J.; Kouvetakis, J.; Menéndez, J. *Appl. Phys. Lett.* **2011***, 98*, 061109.

87 Mathews, J.; Roucka, R.; Xie, J.Q.; Yu, S.Q.; Menéndez, J.; Kouvetakis, J. *Appl. Phys. Lett.* **2009***, 95*, 133506.

88 Senaratne, C.L.; Wallace, P.M.; Gallagher, J.D.; Sims, P.E.; Kouvetakis, J.; Menéndez, J. *J. Appl. Phys.* **2016**, *120*, 025701.

89 Wirths, S.; Ikonic, Z.; Tiedemann, A.T.; Holländer, B.; Stoica, T.; Mussler, G.; Breuer, U.; Hartmann, J.M.; Benedetti, A.; Chiussi, S.; Grützmacher, D.; Mantl, S.; Buca, D. *Appl. Phys. Lett.* **2013**, *103*, 192110.

90 Loo, R.; Vincent, B.; Gencarelli, F.; Merckling, C.; Kumar, A.; Eneman, G.; Witters, L.; Vandervorst, W.; Caymax, M.; Heyns, M.; Thean, A. *ECS J. Solid State SC.* **2013***, 2*, N35.

91 Ike, S.; Moriyama, Y.; Kurosawa, M.; Taoka, N.; Nakatsuka, O.; Imai, Y.; Kimura, S.; Tezuka, T.; Zaima, S. *Thin Solid Films* **2013**, *557*, 1.

92 Oehme, M.; Kostecki, K.; Schmid, M.; Oliveira, F.; Kasper, E.; Schulze, J.*Thin Solid Films* **2014**, *557*, 169.

93 Zaima, S.; Nakatsuka, O.; Taoka, N.; Kurosawa, M.; Takeuchi, W.; Sakashita, M. *Sci. Technol. Adv. Mater.* **2015**, *16*, 43502.

94 Chen, R.; Huang, Y.C.; Gupta, S.; Lin, A.C.; Sanchez, E.; Kim, Y.; Saraswat, K.C.; Kamins, T.I.; Harris, J.S. *J. Cryst. Growth* **2013**, *365*, 29.

95 Bhargava, N.; Coppinger, M.; Prakash, G.J.; Wielunski, L.; Kolodzey, J. *Appl. Phys. Lett.* **2013**, *103*, 041908.

96 Wang, W.; Zhou, Q.; Dong, Y.; Tok, E.S.; Yeo, Y.C. *Appl. Phys. Lett.* **2015**, *106*, 232106.

97 Gurdal, O.; Desjardins, P.; Carlsson, J.R.; Taylor, N.; Radamson, H.H.; Sundgren, J.E.; Greene, J.E. *J. Appl. Phys.* **1998**, *83*, 162.

98 Nikolenko, A.S.; Strelchuk, V.V.; Safriuk, N.V.; Kryvyi, S.B.; Kladko, V.; Oberemok, O.S.; Borkovska, L.V.; Sadofyev, Y.G. *Thin Solid Films* **2015**, 613, 68.

99 D'Costa, V.R.; Wang, W.; Zhou, Q.; Soon, T.E.; Yeo, Y.C. *Appl. Phys. Lett.* **2014**, *104*, 022111.

100 Dybala, F.; Elazna, K.Z.; Maczko, H.; Gladysiewicz, M.; Misiewicz, J.; Kudrawiec, R.; Lin, H.; Chen, R.; Shang, C.; Huo, Y.; Kamins, T.I.; Harris, J.S. *J. Appl. Phys.* **2016**, *119*, 215703.

101 Tseng, H.H.; Li, H.; Mashanov, V.; Yang, Y.J.; Cheng, H.H.; Chang, G.E.; Soref, R.A.; Sun, G. *Appl. Phys. Lett.* **2013**, *103*, 231907.

102 Schwartz, B.; Oehme, M.; Kostecki, K.; Widmann, D.; Gollhofer, M.; Koerner, R.; Bechler, S.; Fischer, I.A.; Wendav, T.; Kasper, E.; Schulze, J.; Kittler, M. *Opt. Lett.* **2015**, *40*, 3209

103 Xie, J.; Beeler, R.T.; Grzybowski, G.; Chizmeshya, A.V.G.; Menéndez, J.; Kouvetakis, J. *Appl. Phys. Lett*. **2009**, *95*, 181909.

104 Matthews, J.W. and Blakeslee, A.E. *J. Cryst. Growth* **1974***, 27*, 118.

105 Clough, R.; Tietjen, J.; *Trans. Metall. Soc.* AIME **1969**, *245*, 583.

106 Wang, L.; Su, S.; Wang, W.; Yang, Y.; Tong, Y.; Liu, B.; Guo, P.; Gong, X.; Zhang, G.; Xue, C.; Cheng, B.; Han, G.; Yeo, Y.C. *IEEE Electron Device Lett.* **2012**, *33* 1529.

107 Han, G.; Su, S.; Wang, L.; Wang, W.; Gong, X.; Yang, Y.; Ivana, ; Guo, P.; Guo, C.; Zhang, G.; Pan, J.; Zhang, Z.; Xue, C.; Cheng, B.; Yeo, Y.C. *2012 Symposium on VLSI Technology (VLSIT)* (IEEE) **2012**, 97.

108 Zhang, X.; Zhang, D.; Zheng, J.; Liu, Z.; He, C.; Xue, C.; Zhang, G.; Li, C.; Cheng, B.; Wang, Q. S*olid. State. Electron.* **2015**, *114*, 178.

109 Jeon, J.; Asano, T.; Shimura, Y.; Takeuchi, W.; Kurosawa, M.; Sakashita, M.; Nakatsuka, O.; Zaima, S. *Jpn. J. Appl. Phys.* **2016**, *55*, 04EB13.

110 Gallagher, J.D.; Senaratne, C.L.; Wallace, P. M.; Menéndez, J.; Kouvetakis, J. *Appl. Phys. Lett.* **2015**, *107*, 123507.

111 Desjardins, P.; Spila, T.; Gürdal, O.; Taylor, N.; Greene, J. *Phys. Rev. B* **1999**, *60*, 15993.

112 Gencarelli, F.; Vincent, B.; Demeulemeester, J.; Vantomme, A.; Moussa, A.; Franquet, A.; Kumar, A.; Bender, H.; Meersschaut, J.; Vandervorst, W.; Loo, R.; Caymax, M.; Temst, K.; Heyns, M. *ECS J. Solid State Sci. Technol.* **2013**, *2*, 134.

113 Hull, R.; Bean, J.C.; Buescher, C.A.*J. Appl. Phys.* **1989**, *66*, 5837.

114 Houghton, D.C. *J. Appl. Phys.* **1991**, *70*, 2136.

115 Yonenaga, I.; Werner, M.; Bartsch, M.; Messerschmidt, U.; Werner, E.R. *Phys. Status Solidi* **1999**, *171*, 35.

116 Menéndez, J. *J. Appl. Phys.* **2009**, *105*, 063519.

117 People, R. and Bean, J.C. *Appl. Phys. Lett.* **1985**, *47*, 322.

118 Wang, W.; Li, L.; Zhou, Q.; Pan, J.; Zhang, Z.; Tok, E.S.; Yeo, Y. *Appl. Surf. Sci.* **2014**, *321*, 240.

119 Houghton, D.C.; Gibbings, C.J.; Tuppen, C.G.; Lyons, M.H.; Halliwell, M.A.G. *Thin Solid Films* **1989**, *183*, 171.

120 Houghton, D.C.; Gibbings, C.J.; Tuppen, C.G.; Lyons, M.H.; Halliwell, M.A.G. *Appl. Phys. Lett.* **1990**, *56*, 460.

121 Dunstan, D.J. *J. Mater. Sci. Mater. Electron.* **1997**, *8*, 337.

122 Hu, S.M. *J. Appl. Phys.* **1991**, *69*, 7901.

123 Spitzer, W. G.; Trumbore, F. A.; Logan, R. A. *J. Appl. Phys.* **1961**, *32*, 1822.

124 Impellizzeri, G.; Napolitani, E.; Boninelli, S.; Fisicaro, G.; Cuscunà, M.; Milazzo, R.; La Magna, A.; Fortunato, G.; Priolo, F.; Privitera, V. *J. Appl. Phys.* **2013**, *113*, 113505.

125 Chui, C. O.; Gopalakrishnan, K.; Griffin, P. B.; Plummer, J. D.; Saraswat, K. C. *Appl. Phys. Lett*., **2003**, *83*, 3275.

126 Camacho-Aguilera, R. E.; Cai, Y.; Bessette, J. T.; Kimerling, L. C.; Michel, J. *Opt. Mater. Express* **2012**, *2*, 1462.

127 Bogumilowicz, Y. and Hartmann, J.M. *Thin Solid Films* **2014**, *557*, 4.

128 Moriyama, Y.; Kamimuta, Y.; Kamata, Y.; Ikeda, K.; Sakai, A; Tezuka, T. *Appl. Phys. Express* **2014**, *7*, 106501.

129 Jakomin, R.; Beaudoin, G.; Gogneau, N.; Lamare, B.; Largeau, L.; Mauguin, O.; Sagnes, I. *Thin Solid Films* **2011**, *519*, 4186.

130 Xu, C.; Gallagher, J. D.; Wallace, P. M.; Senaratne, C. L.; Sims, P.; Menéndez, J.; Kouvetakis, J. *Semicond. Sci. Technol.* **2015**, *30*, 105028.

131 Satta, A.; Simoen, E.; Clarysse, T.; Janssens, T.; Benedetti, A.; De Jaeger, B.; Meuris, M.; Vandervorst, W. *Appl. Phys. Lett.* **2005**, *87*, 172109.

132 Mirabella, S.; Impellizzeri, G.; Piro, A. M.; Bruno, E.; Grimaldi, M. G. *Appl. Phys. Lett.* **2008**, *92*, 251909.

133 Trumbore, F.A. *Bell Syst. Tech. J.* **1960**, *39*, 205.

134 Bidwell, L.R. *J. Less. Common. Met*. **1970**, *20*, 19.

135 Wu, Y.; Luo, S.; Wang, W.; Masudy-Panah, S.; Lei, D.; Liang, G; Gong, X.; Yeo, Y.-C. *J. Appl. Phys.* **2017**, *122*, 224503.

136 Hellings, G.; Wuendisch, C.; Eneman, G.; Simoen, E.; Clarysse, T.; Meuris, M.; Vandervorst, W.; Posselt, M.; De Meyer, K. *Electrochem. Solid-State Lett.* **2009**, *12*, H417.

137 Herrmannsdörfer, T.; Heera, V.; Ignatchik, O.; Uhlarz, M.; Mücklich, A.; Posselt, M.; Reuther, H.; Schmidt, B.; Heinig, K.-H.; Skorupa, W.; Voelskow, M.; Wündisch, C.; Skrotzki, R.; Helm, M.; Wosnitza, J. *Phys. Rev. Lett.,* **2009**, *102*, 217003.

138 Kawanaka, M.; Iguchi, N.; Fujieda, S.; Furukawa, A.; Baba, T. *J. Appl. Phys.* **1993**, *74*, 3886.

139 Oehme, M.; Werner, J.; Kasper, E. *J. Cryst. Growth* **2008**, *310*, 4531.

140 Shimura, Y.; Takeuchi, S.; Nakatsuka, O.; Vincent, B.; Gencarelli, F.; Clarysse, T.; Vandervorst, W.; Caymax, M.; Loo, R.; Jensen, A.; Petersen, D.H.; Zaima, S. *Thin Solid Films* **2012**, *520*, 3206.

141 Wang, W.; Vajandar, S.; Lim, S. L.; Dong, Y.; D'Costa, V. R.; Osipowicz, T.; Tok, E. S.; Yeo, Y.-C. *J. Appl. Phys.* **2016**, *119*, 155704.

142 Dapkus, P.D.; M.Manasevit, H.; Hess, K.L.; Low, T.S.; Stillman, G.E. *J. Crystal Growth*, **1981**, *55*, 10.

143 Sims, P. E.; Wallace, P. M.; Xu, C.; Poweleit, C. D.; Claflin, B.; Kouvetakis, J.; Menéndez, J. *Appl. Phys. Lett.* **2017**, *111*, 122101.

144 Grzybowski, G.; Jiang, L.; Beeler, R. T.; Watkins, T.; Chizmeshya, A. V. G.; Xu, C.; Menéndez, J.; Kouvetakis, J. *Chem. Mater.* **2012**, *24*, 1619.

145 Cuttriss, D. B. *Bell Syst. Tech. J.* **1961**, *40*, 509.

146 Gallagher, J.D.; Xu, C.; Jiang, L.; Kouvetakis, J.; Menéndez, J. *Appl. Phys. Lett.* **2013**, *103*, 202104.

147 Wagner, J.; Viña, L. *Phys. Rev. B* **1984**, *30*, 7030.

148 Mathews, J.; Roucka, R.; Weng, C.; Beeler, R.; Tolle, J.; Menéndéz, J.; Kouvetakis, J. *ECS Trans*. **2010**, *33*, 765.

149 Dimroth, F. and Kurtz, S. *MRS Bulletin* **2007**, *32*, 230.

150 Noreika, A. J. and Francombe, M. H. *J. Appl. Phys.* **1974**, *45*, 3690. Cadien, K. C.;

151 Eltoukhy, A. H.; Greene, J. E. *Appl. Phys. Lett.* **1981**, *38*, 773.

152 Banerjee, I.; Chung, D. W.; Kroemer, H. *Appl. Phys. Lett.* **1985**, *46*, 494.

153 Grzybowski, G.; Watkins, T.; Beeler, R. T.; Jiang, L.; Smith, D. J.; Chizmeshya, A. V. G.; Kouvetakis, J.; Menéndez, J. *Chem. Mater.* **2012**, *24*, 2347.

154 Barnett, S. A.; Ray, M. A.; Lastras, A.; Kramer, B.; Greene, J. E.; Raccah, P. M.; Abels, L. L. *Electron. Lett.* **1982**, *18*, 891.

155 Baxter, P.L.; Downs, A.J.; Rankin, D.W.H; Robertson, H.E. *J. Chem. Soc Dalton Trans*. **1985**, 807.

156 Tang, C.V.; Jones, A.J.; Greene, T.M.; Kettle, L.; Rankin, D.W.H.; Robertson, H. E.; Turner, A.R. *Dalton Trans*. **2006**, 1204.

157 McSkimin, H. J. *J. Appl. Phys*. **1953**, *24*, 988.

158 McSkimin, H. J.; Jayaraman, A.; Andreatch, P. *J. Appl. Phys.* **1967**, *38*, 2362.

159 Boyle, W. F. and Sladek, R. J. *Phys. Rev. B* **1975**, *11*, 2933.

160 Giannozzi, P.; Baroni, S.; Bonini, N; Calandra, M.; Car, R.; Cavazzoni, C.; Ceresoli, D.; Chiarotti, G. L.; Cococcioni, M.; Dabo, I.; Dal Corso, A.; Fabris, S.; Fratesi, G.; de Gironcoli, S.; Gebauer, R.; Gerstmann, U.; Gougoussis, C.; Kokalj, A.; Lazzeri, M.; Martin-Samos, L.; Marzari, N.; Mauri, F.; Mazzarello, R.; Paolini, S.; Pasquarello, A.; Paulatto, L.; Sbraccia, C.; Scandolo, S.; Sclauzero, G.; Seitsonen, A. P.; Smogunov, A.; Umari, P.; Wentzcovitch, R. M. *J. Phys.: Condens. Matter* **2009**, *21*, 395502.

161 Perdew, J. P.; Burke, K.; Ernzerhof, M. *Phys. Rev. Lett.* **1996**, *77*, 3865.

162 Boote, B. W.; Men, L.; Andaraarachchi, H. P.; Bhattacharjee, U.; Petrich, J. W.; Vela, J.; Smith, E. A. Germanium–Tin/Cadmium Sulfide Core/Shell Nanocrystals with Enhanced Near-Infrared Photoluminescence. Chem. Mater. 2017, 29(14), 6012.

163 Eckl, C.; Pavone, P.; Fritsch, J.; Schröder, U. in *The Physics of Semiconductors*; Scheffler, M. and Zimmerman, R. Ed.; Singapore, 1996; Vol. 1; p. 229.

164 Kawai, H.; Giorgi, G.; Yamashita, K. *Phys. Stat. Sol. B* **2012**, *249*, 29.

165 Davis, L.; Holloway, H. *Phys. Rev. B* **1987**, *35*, 2767.

166 Woo, K.; Lee, K.; Kovnir, K. *Mater. Res. Express* **2016**, *3*, 074003.

167 Lund, J.; Olschner, F.; Ahmed, F.; Shah, K. *MRS Proceedings* **1989**, *162*, 601.

168 Abbott, J.K.; Brasfield, J.D.; Rack, P.D.; Duscher, G.J.; Feigerle, C.S. *MRS Proceedings* **2012**, *1432*, 12.

169 Mizutani, T.; Ohsawa, J.; Nishinaga, T.; Uchiyama, S. *Jpm. J. Appl. Phys.* **1976**, *15*, 1305.

170 Gibson, D.R.; Waddell, E.M.; Wilson, S.A.; Lewis, K.L. *Opt. Eng.* **1994**, *33*, 957.

171 Brasfield, J.D. Chemical Vapor Deposition of Heteroepitaxial Boron Phosphide Thin Films. Ph.D. Dissertation, University of Tennessee, 2013.

172 Popper, P. and Ingles, T. *Nature* **1957**, *179*, 1075.

173 Ananthanarayanan, K.; Mohanty, C.; Gielisse, P. *J. Cryst. Growth* **1973**, *20*, 63.

174 Williams, F.V.; Ruehrwein, R.A. *J. Amer. Chem. Soc.* **1960**, *82*, 1330.

175 Vickery, R. *Nature* **1959**, *184*, 268.

176 Chu, T.; Jackson, J.; Smeltzer, R. *J. Electrochem. Soc.* **1973**, *120*, 802.

177 Kumashiro, Y.; Okada, Y. *Appl. Phys. Lett.* **1985**, *47*, 64.

178 Manasevit, H.; Hewitt, W.; Nelson, A.; Mason, A. *J. Electrochem. Soc.* **1989**, *136*, 3070.

179 Huber, S.; Gullikson, E.; Frye, C.; Edgar, J.; van de Kruijs, R.; Bijkerk, F.; Prendergast, D. *Chem. Mater.* **2016**, *28*, 8415.

APPENDIX A

PERMISSIONS FOR REPRINTED MATERIALS

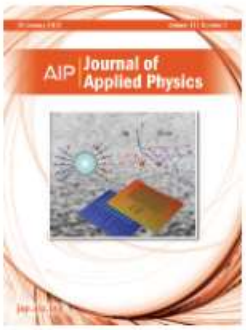

Title:	Direct gap Ge1-ySny alloys: Fabrication and design of mid-IR photodiodes
Author:	C. L. Senaratne, P. M. Wallace, J. D. Gallagher, et al
Publication:	Journal of Applied Physics
Volume/Issue	120/2
Publisher:	AIP Publishing
Date:	Jul 14, 2016
Page Count:	9

Order Completed

Thank you for your order.

This Agreement between Arizona State University -- Patrick Wallace ("You") and AIP Publishing ("AIP Publishing") consists of your license details and the terms and conditions provided by AIP Publishing and Copyright Clearance Center.

Your confirmation email will contain your order number for future reference.

printable details

License Number	4373800737765
License date	Jun 21, 2018
Licensed Content Publisher	AIP Publishing
Licensed Content Publication	Journal of Applied Physics
Licensed Content Title	Direct gap Ge1-ySny alloys: Fabrication and design of mid-IR photodiodes
Licensed Content Author	C. L. Senaratne, P. M. Wallace, J. D. Gallagher, et al
Licensed Content Date	Jul 14, 2016
Licensed Content Volume	120
Licensed Content Issue	2
Requestor type	Author (original article)
Format	Print and electronic
Portion	Excerpt (> 800 words)
Requestor Location	Arizona State University Arizona State University TEMPE, AZ 85287 United States Attn: Arizona State University
Billing Type	Invoice
Billing address	Arizona State University Arizona State University TEMPE, AZ 85287 United States Attn: Arizona State University
Total	0.00 USD

ORDER MORE | CLOSE WINDOW

Title: Semiconductor Science and Technology
Article ID: 0268-1242
Publication: Publication1
Publisher: CCC Republication
Date: Jan 1, 1986

Order Completed

Thank you for your order.

This Agreement between Patrick M Wallace ("You") and IOP Publishing ("IOP Publishing") consists of your order details and the terms and conditions provided by IOP Publishing and Copyright Clearance Center.

License number	Reference confirmation email for license number
License date	Jul, 31 2018
Licensed content publisher	IOP Publishing
Licensed content title	Semiconductor Science and Technology
Licensed content date	Jan 1, 1986
Type of use	Thesis/Dissertation
Requestor type	Academic institution
Format	Print, Electronic
Portion	chapter/article
The requesting person/organization	Patrick Wallace Arizona State University
Title or numeric reference of the portion(s)	Chapter 3
Title of the article or chapter the portion is from	Molecular epitaxy of pseudomorphic Ge1−y Sn y (y = 0.06–0.17) structures and devices on Si/Ge at ultra-low temperatures via reactions of Ge4H10 and SnD4
Editor of portion(s)	Patrick Wallace
Author of portion(s)	Patrick Wallace
Volume of serial or monograph	N/A
Page range of portion	
Publication date of portion	August 2018
Rights for	Main product
Duration of use	Life of current edition
Creation of copies for the disabled	no
With minor editing privileges	no
For distribution to	United States
In the following language(s)	Original language of publication
With incidental promotional use	no
Lifetime unit quantity of new product	Up to 499
Title	Germanium as a mid-IR material: Extending the optical range of Ge through Group IV and III-V-IV alloy systems
Instructor name	n/a
Institution name	n/a
Expected presentation date	Aug 2018
Requestor Location	Arizona State University Arizona State University TEMPE, AZ 85287 United States Attn: Arizona State University
Billing Type	Invoice
Billing address	Arizona State University Arizona State University TEMPE, AZ 85287 United States Attn: Arizona State University
Total (may include CCC user fee)	0.00 USD
Total	0.00 USD

CLOSE WINDOW